A&A 656, A46 (2021)
https://doi.org/10.1051/0004-6361/202141567

Astronomy & Astrophysics

ALCHEMI, an ALMA Comprehensive High-resolution Extragalactic Molecular Inventory

Survey presentation and first results from the ACA array

S. Martín[1,2], J. G. Mangum[3], N. Harada[4,5,6], F. Costagliola[7], K. Sakamoto[5], S. Muller[7], R. Aladro[8], K. Tanaka[9], Y. Yoshimura[10], K. Nakanishi[4,6], R. Herrero-Illana[1,11], S. Mühle[12], S. Aalto[7], E. Behrens[13], L. Colzi[14,15], K. L. Emig[3,⋆], G. A. Fuller[16,17], S. García-Burillo[18], T. R. Greve[19,20], C. Henkel[8,21,22], J. Holdship[23,20], P. Humire[8], L. Hunt[15], T. Izumi[4,6], K. Kohno[10,24], S. König[7], D. S. Meier[25,26], T. Nakajima[27], Y. Nishimura[10,4], M. Padovani[15], V. M. Rivilla[14,15], S. Takano[28], P. P. van der Werf[23], S. Viti[23,20], and Y. T. Yan[8]

(Affiliations can be found after the references)

Received 16 June 2021 / Accepted 14 September 2021

ABSTRACT

Context. The interstellar medium is the locus of physical processes affecting the evolution of galaxies which drive or are the result of star formation activity, supermassive black hole growth, and feedback. The resulting physical conditions determine the observable chemical abundances that can be explored through molecular emission observations at millimeter and submillimeter wavelengths.
Aims. Our goal is to unveiling the molecular richness of the central region of the prototypical nearby starburst galaxy NGC 253 at an unprecedented combination of sensitivity, spatial resolution, and frequency coverage.
Methods. We used the Atacama Large Millimeter/submillimeter Array (ALMA), covering a nearly contiguous 289 GHz frequency range between 84.2 and 373.2 GHz, to image the continuum and spectral line emission at 1.6″(~28 pc) resolution down to a sensitivity of 30−50 mK. This article describes the ALMA Comprehensive High-resolution Extragalactic Molecular Inventory (ALCHEMI) large program. We focus on the analysis of the spectra extracted from the 15″ (~255 pc) resolution ALMA Compact Array data.
Results. We modeled the molecular emission assuming local thermodynamic equilibrium with 78 species being detected. Additionally, multiple hydrogen and helium recombination lines are identified. Spectral lines contribute 5 to 36% of the total emission in frequency bins of 50 GHz. We report the first extragalactic detections of C_2H_5OH, HOCN, HC_3HO, and several rare isotopologues. Isotopic ratios of carbon, oxygen, sulfur, nitrogen, and silicon were measured with multiple species.
Conclusion. Infrared pumped vibrationaly excited HCN, HNC, and HC_3N emission, originating in massive star formation locations, is clearly detected at low resolution, while we do not detect it for HCO^+. We suggest high temperature conditions in these regions driving a seemingly "carbon-rich" chemistry which may also explain the observed high abundance of organic species close to those in Galactic hot cores. The L_{vib}/L_{IR} ratio was used as a proxy to estimate a 3% contribution from the proto super star cluster to the global infrared emission. Measured isotopic ratios with high dipole moment species agree with those within the central kiloparsec of the Galaxy, while those derived from $^{13}C^{18}O$ are a factor of five larger, confirming the existence of multiple interstellar medium components within NGC 253 with different degrees of nucleosynthesis enrichment. The ALCHEMI data set provides a unique template for studies of star-forming galaxies in the early Universe.

Key words. line: identification – galaxies: ISM – galaxies: individual: NGC 253 – galaxies: starburst – ISM: molecules – submillimeter: ISM

1. Introduction

The interstellar medium (ISM) is the location and source of fuel for key phenomena that influence the evolution of galaxies. While star formation is one of the most important of such phenomena, the ISM is sensitive to a large number of processes, such as radiative transfer effects, heating and cooling, and/or active chemistry (see Omont 2007, for a review). Moreover, the physical properties of the ISM and the effects of such processes imprint their signatures in the many atomic and molecular spectral lines they emit. This fact makes the observation of molecular emission an essential tool in the study of the ISM, where different tracers probe different physical processes within the gaseous component in galaxies (i.e., Meier & Turner 2005, 2012; Takano et al. 2014; Meier et al. 2015; Martín et al. 2015; Harada et al. 2019). Thus it is essential to observe as many molecular tracers as is observationally feasible to understand the ongoing processes in these regions.

Additionally, it is crucial to evaluate as many different types of environments as possible to capture and understand how the mechanisms at work affect the ISM. Although our own Galaxy is the ideal nearby laboratory, our position within the disk sometimes hinders our ability to have a clear view of the overall ISM properties. Furthermore, our Galaxy lacks the extreme environments created by star bursting regions, high or low metallicity gas environments, growth of supermassive blackholes, or intense feedback by massive outflows. The observation of nearby galaxies allows us to probe different environments and study their physical and chemical properties. For this work we probed the ISM under a star bursting environment.

Almost five decades have passed since the first extragalactic detection of carbon monoxide (CO) toward the nearby starburst

⋆ Jansky Fellow of the National Radio Astronomy Observatory.

galaxies NGC 253 and M 82 (Rickard et al. 1975), the two brightest extragalactic IRAS sources beyond the Magellanic Clouds (Soifer et al. 1989), and shortly after the first detection of CO in the Galaxy (Wilson et al. 1970). These CO emission detections had only been preceded by the extragalactic detections of OH (Weliachew 1971) and H_2CO (Gardner & Whiteoak 1974) in absorption, and were quickly followed by detections of higher dipole moment species such as HCN (Rickard et al. 1977). Such milestones in extragalactic molecular observations were only possible thanks to improvements in receiver technology. These observations have gone on to shape our current knowledge of galaxy evolution and the complexity of processes in the ISM within those galaxies in a fundamental way.

The advent of instruments operating at millimeter wavelengths with a larger collecting area, lower noise receivers, broadband spectrometers, and being placed at drier locations resulted in observing speed improvements of more than three orders of magnitude. Such a technological leap allowed, for example, the detection of the fainter CO isotopologues (Harrison et al. 1999) and tentative detections of its double isotopologue $^{13}C^{18}O$ (Martín et al. 2010) in extragalactic environments, now routinely achievable with the Atacama Large Millimeter/Submillimeter array (ALMA; Martín et al. 2019b). Studies using both spectral detection and imaging of dense molecular gas tracers (see Mauersberger & Henkel 1989, and the subsequent series of papers) could be considered the genesis of today's field of extragalactic molecular astrophysics and astrochemistry.

However, it was not until the pioneering systematic large multitransition and multimolecule work from Wang et al. (2004), followed shortly after by the first unbiased extragalactic spectral line surveys (Martín et al. 2006, 2011; Muller et al. 2011; Aladro et al. 2011a), that the field of extragalactic astrochemistry developed its full power, with dozens of species detected (see Sect. 4.4) and made full use of the bandwidth increase in receiver and spectrometer technology. To the best of our knowledge, Table 1 summarizes every published wide-band (>10 GHz) extragalactic spectral line survey conducted with millimeter and submillimeter ground-based observatories.

The Sculptor galaxy, NGC 253, is a nearby ($D \sim 3.5 \pm 0.2$ Mpc, Rekola et al. 2005; Mouhcine et al. 2005) almost edge-on barred spiral galaxy (Puche et al. 1991; Pence 1981; de Vaucouleurs et al. 1991). Its central molecular zone (CMZ), about 300 × 100 pc in size (Sakamoto et al. 2011), containing $\sim 10^8$ $M_\odot$ of molecular gas (Canzian et al. 1988; Mauersberger et al. 1996; Harrison et al. 1999; Sakamoto et al. 2011). Such a large amount of gas in the NGC 253 CMZ is built up as a result of gas inflow toward the inner Lindblad resonance (ILR) region at $r \sim 500$ pc. This inflow appears to be driven by a stellar bar, which has a deprojected length of 2.5 kpc and clearly stands out in near-infrared observations (Scoville et al. 1985; Forbes & Depoy 1992; Paglione et al. 2004; Iodice et al. 2014), rather than by interaction with the nearby galaxy NGC 247, based on the regularity of the H I velocity field and density distribution outside its central region (Combes et al. 1977; Puche et al. 1991). This molecular material is responsible for feeding the burst of star formation of 2 $M_\odot\,\mathrm{yr}^{-1}$ in the central kiloparsec (Leroy et al. 2015; Bendo et al. 2015) which accounts for approximately half of the global star formation of 3.6–4.2 $M_\odot\,\mathrm{yr}^{-1}$, based on the infrared luminosity of $L_{\rm IR} = 2.1 \times 10^{10}\,L_\odot$ (Sanders et al. 2003; Strickland et al. 2004).

Radio observations reveal at least 64 individual compact continuum sources within the NGC 253 CMZ, 23 of which have spectral indices measured by Ulvestad & Antonucci (1997). Of these 23 spectral index measurements, 17 have errors less

Table 1. Extragalactic spectral scans at mm and submm wavelengths.

Source (#)	Frequency coverage (GHz)	Telescope	Ref.
NGC 4945	82–354 [a]	SEST 15m	1
NGC 253	86–116	IRAM 30m	2
	86–116 [b]	ALMA	3
	85–116	Nobeyama 45m	4, 5
	129–175	IRAM 30m	6
N113 (LMC)	85–357 [a]	SEST 15m	7
M 82	86–116	IRAM 30m	2
	130–175	IRAM 30m	8
	241–260	IRAM 30m	8
	190–307 [c]	CSO 10.4m	9
NGC 1068	86–116	IRAM 30m	10
	85–116	Nobeyama 45m	4, 5
	161–169 [b]	IRAM 30m	11
	176–184 [b]	IRAM 30m	11
	190–307 [c]	CSO 10.4m	12
PKS 1830-211 [d]	57–94	ATCA	13
	59–94	Yebes 40m	14
Arp 220	86–116	IRAM 30m	2
	202–242	SMA	15
M 51	86–116	IRAM 30m	2
	83–116	IRAM 30m	16
	130–148	IRAM 30m	16
M 83	86–116	IRAM 30m	2
NGC 4418	84–113	ALMA	17
	214–294 [b]	ALMA	17
IC 342	84–116	Nobeyama 45m	4, 5
IC 10	84–116	Nobeyama 45m	18
NGC 3256	85–113	ALMA	19
	214–273	ALMA	19
NGC 3627	85–116	IRAM 30m	20
	140–148	IRAM 30m	20
	85–115.5	Nobeyama 45m	20
Survey (10)	74–111 [c]	FCRAO 14m	21
Survey (23)	84–92	IRAM 30m	22
	108–116	IRAM 30m	22
Survey (4)	85–268 [b]	IRAM 30m	23
Survey (7, LMC)	85–116	MOPRA 22m	24

Notes. The source column indicates the name of the survey target or the number of surveyed sources in multisource works (labeled Survey). Sources are chronologically ordered according to the year of its first survey publication. Large Magellanic Cloud (LMC) sources are indicated. [a]Multiple targeted tunings within the indicated frequency coverage. [b]Not fully sampled. Multiple tunings within the indicated frequency coverage with broadband receivers. [c]Using low spectral resolution high redshift ultra wide band receivers. [d]Molecular absorber system. The frequency refers to rest frequency, which at the redshift of the source corresponds to observed frequecy range of 30–50 and 31.5–50 GHz for the two references, respectively.

References. (1) Wang et al. (2004); (2) Aladro et al. (2015); (3) Meier et al. (2015); (4) Nakajima et al. (2018); (5) Takano et al. (2019); (6) Martín et al. (2006); (7) Wang et al. (2009); (8) Aladro et al. (2011a); (9) Naylor et al. (2010); (10) Aladro et al. (2013); (11) Qiu et al. (2020); (12) Kamenetzky et al. (2011); (13) Muller et al. (2011); (14) Tercero et al. (2020); (15) Martín et al. (2011); (16) Watanabe et al. (2014); (17) Costagliola et al. (2015) (18) Nishimura et al. (2016a); (19) Harada et al. (2018) (20) Watanabe et al. (2019); (21) Snell et al. (2011); (22) Costagliola et al. (2011); (23) Li et al. (2019); (24) Nishimura et al. (2016b)

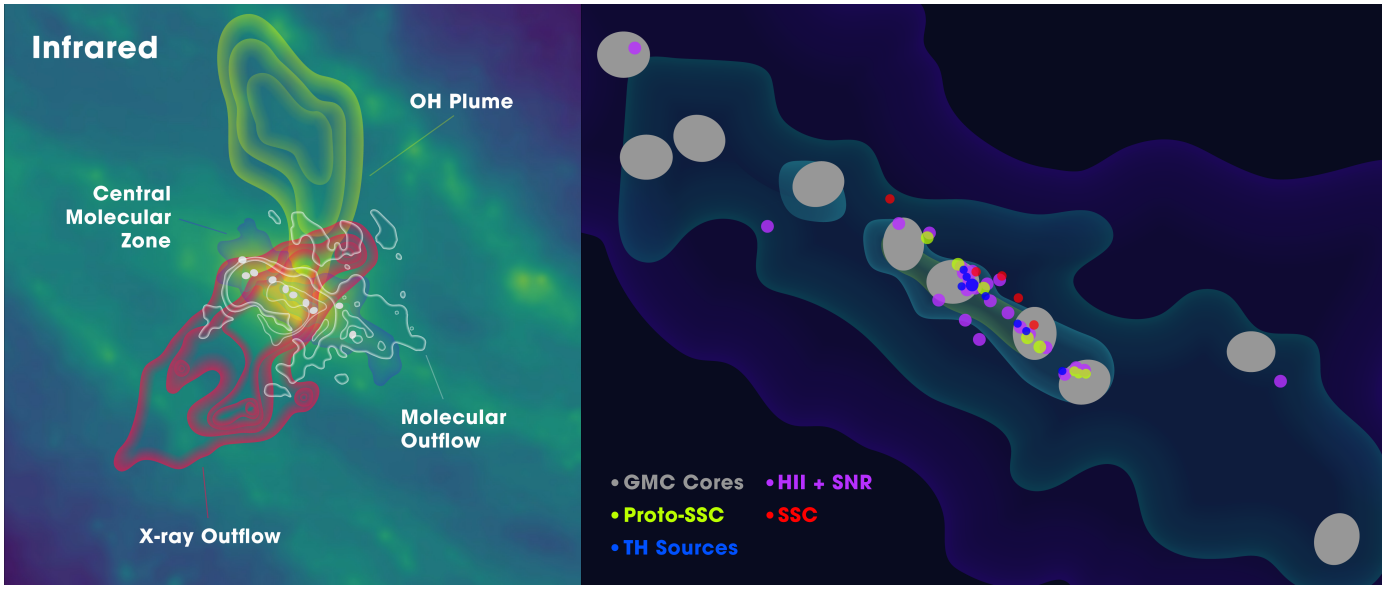

Fig. 1. Schematic summary of the activity within central molecular zone of NGC 253. See Sect. 1 for a comprehensive summary of the activity in its central region as probed by multiwavelength observations. In both figures, the CO traced CMZ, and the dense gas traced GMCs (Leroy et al. 2015) are included as a spatial scale reference. *Left*: IRAC 8μm from *Spitzer* Local Volume Legacy survey (Dale et al. 2009) in the background; *Chandra* X-ray traced outflow (Strickland et al. 2000); 18 cm OH plume (Turner 1985); molecular outflow observed in CO emission (Bolatto et al. 2013). *Right*: 2 cm TH sources (Turner & Ho 1985) and HII regions and supernovae remnants (Ulvestad & Antonucci 1997); proto-super stellar clusters traced by vibrationally excited HC_3N emission (Rico-Villas et al. 2020); star cluster identified from near-IR HST imaging (Watson et al. 1996).

than 0.4. About half the sources in this subset have spectral indices below −0.4, indicating synchrotron emission likely associated with supernovae remnants. The remaining sources have spectral indices spanning 0.0–0.2, which is indicative of free-free emission stemming from HII regions. Ulvestad & Antonucci (1997) note that the majority of flat-spectrum sources lie along the galaxy disk midline, whereas the steeper-spectrum sources lie farther away from the central axis. The brightest of these radio sources (TH2, Turner & Ho 1985) is associated with the nucleus of the galaxy, within 1″ of the galaxy's kinematic center (Müller-Sánchez et al. 2010). The five giant molecular cloud complexes identified from 1″ resolution dust and CO observations (Sakamoto et al. 2011) are resolved into 14 dust clouds at 0.11″ resolution (1.9 pc, Leroy et al. 2018). Only one of these dust clumps is associated with a near-infrared identified super star clusters (SSCs; Watson et al. 1996). These molecular clouds are responsible for the star formation activity within the central region of NGC 253 and appear to be at different stages of evolution, with proto-SSCs identified through vibrational molecular emission (Rico-Villas et al. 2020) and molecular outflows (Levy et al. 2021). Adaptive optics observations resolve 37 IR knots on top of the diffuse emission, eight of which have radio counterparts (Fernández-Ontiveros et al. 2009). Among the many X-ray observations toward NGC 253 (e.g., Bauer et al. 2008, and references therein), Lehmer et al. (2013) reported the detection of three ultra-luminous X-ray sources, one of which is located 1″ from the dynamical center, but with no signs of active galactic nucleus (AGN) activity. A starburst-driven outflow is traced by X-ray and Hα emission all the way to 9 kpc from the disk (Dahlem et al. 1998; Strickland et al. 2000). The outflow entrains molecular gas away from its base, limiting the star formation activity in NGC 253 by negative feedback (Bolatto et al. 2013; Walter et al. 2017; Krieger et al. 2019). The sketch presented in Fig. 1 aims at visually summarizing this complex region.

As one of the brightest extragalactic infrared sources (Soifer et al. 1989) and the most prominent molecular emitter beyond the Magellanic Clouds, the prototypical local starburst galaxy NGC 253 has been the target of multiple molecular spectral line studies (see Table 1). Due to its proximity, high resolution studies can resolve the giant molecular cloud (GMC) scales of a few tens of parsecs (Sakamoto et al. 2011; Ando et al. 2017; Leroy et al. 2018). In particular, NGC 253 has been the target of a number of ALMA observations which analyzed the properties of individual molecular clouds and complexes within its CMZ (Sakamoto et al. 2011; Meier et al. 2015; Leroy et al. 2015, 2018; Ando et al. 2017; Mangum et al. 2019; Martín et al. 2019b; Rico-Villas et al. 2020; Krieger et al. 2020).

The ALMA Comprehensive High-resolution Extragalactic Molecular Inventory (ALCHEMI) is an ALMA large program whose aim is to obtain the most complete spatially resolved unbiased molecular inventory toward a starburst environment. For this purpose we carried out a broadband spectral scan toward the NGC 253 CMZ with a homogeneous spatial resolution. Unbiased wide-band spectral line surveys provide immediate advantages over narrow-band spectroscopy since the detection of multiple transitions per molecular species allows us to observationally constrain the excitation conditions (e.g., Aladro et al. 2011b; Pérez-Beaupuits et al. 2018; Scourfield et al. 2020). They also allow for the evaluation of line blending between molecular lines by simultaneously fitting many transitions of a given species rather than fitting individual spectral features.

The main objectives of ALCHEMI are to: (1) Define a uniform molecular template for an extragalactic starburst environment, where systematic uncertainties are minimized; (2) accurately constrain the physical conditions of individual star-bursting molecular cloud complexes; (3) study the ISM enrichment by stellar nucleosynthesis through measurement of isotopic ratios; (4) enable a direct comparison of the physical and chemical ISM properties between the Milky Way and an active star-forming environment; (5) explore the chemistry of complex organic molecules (COMs) in the CMZ of NGC 253; (6) evaluate

gas processing in galactic outflows. This study provides a template for the molecular emission in a starburst galaxy that can be compared to future spatially-resolved millimeter and submillimeter studies of more distant galaxies on GMC size scales.

This paper, the first in a series of articles which will describe the scientific results from ALCHEMI, provides a global presentation of the ALCHEMI survey that includes data obtained with both the main (12 m) and Morita (ACA 7 m) arrays. However, here we focus, as a first step, on the analysis and discussion of the low resolution (15″ ∼ 255 pc) 7m array data. This study aims at describing the global molecular properties of the entire unresolved CMZ of NGC 253. As such, and similar to existing single-dish line surveys but with improved frequency coverage and sensitivity (5.6× broader and >2−10 deeper than Martín et al. 2006), the low resolution data analyzed here provide a template of a starburst environment for spatially-unresolved targets at larger distances. Already at this low resolution we explore the physical conditions of the gas and the enrichment of the ISM, and peer into the genesis of complex organic molecules in NGC 253.

2. Observations

The CMZ in NGC 253 was imaged with ALMA in frequency Bands 3, 4, 6, and 7 as part of the Cycle 5 large program 2017.1.00161.L. The survey was subsequently extended to Band 5 during ALMA Cycle 6 (project code 2018.1.00162.S). A total of 101.5 h of integration time on source were acquired, 38.8 hours of which were obtained with the 12 m array.

The nominal phase center of the observations is $\alpha = 00^{\rm h}47^{\rm m}33.26^{\rm s}$, $\delta = -25°17'17\farcs7$ (ICRS). Observations were configured to cover a common rectangular area of 50″ × 20″ (850 × 340 pc) with a position angle of 65° (east of north), and a target resolution of 1″ (17 pc, see Sect. 3.2). This targeted region required a single pointing in Band 3, where the 12 m antenna primary beams range between 57″ and 68″, and Nyquist-sampled mosaic patterns of 5 to 19 pointings (from the lower frequency end of Band 4 to the upper frequency end of Band 7, respectively) with the 12 m array. The average integration time per mosaic pointing to achieve the target sensitivity (Sect. 2.2) varied from ∼2.6 h in Band 3, ∼12 min in Band 4, ∼9 min in Band 5, ∼4 min in Band 6, and ∼2.5 min in Band 7. Additional single pointing observations in a 12 m more compact configuration or 7 m array were performed to achieve a common maximum recoverable scale of 15″ across the whole survey (see Sect. 2.3).

2.1. Frequency setup

The full data set results in a rest-frequency coverage between 84.2 and 373.2 GHz, with 47 individual tunings, each composed of four 1.875 GHz spectral windows from two receiver sidebands. Table A.1 compiles the frequency coverage of the final data products per tuning and separated by receiver sideband after homogeneous processing (Sect. 3.2).

The broad frequency range of 289 GHz was continuously covered except for a few narrow regions: First, the ∼9 GHz gap between bands 3 and 4 (from 116 to 125 GHz avoiding the deep 118.75 GHz telluric oxygen line) is not observable with the ALMA receivers. Between the other receiver bands, the frequency gaps are significantly narrower: only 325 MHz around 163 GHz (bands 4–5), 250 MHz around 211.1 GHz (bands 5–6), and 225 MHz around 275.25 GHz (bands 6–7). The spectral window centered close to the 183 GHz telluric water line was observed, but the data quality was not good enough for calibration. Finally, the ∼9 GHz frequency range from 319.3 to 328.3 GHz, surrounding the 325 GHz telluric water line, was intentionally not covered, given the expected poor atmospheric transmission, to reduce the number of tunings necessary to cover the large frequency width of ALMA Band 7.

A variable frequency overlap of 50 to 500 MHz was used between two adjacent spectral windows within a given sideband, and a frequency overlap of 100–200 MHz between contiguous tunings was adopted, allowing us to check the relative amplitude calibration across the survey (Sect. 3.1).

The native spectral resolution was 0.977 MHz, equivalent to 3.4 to 0.8 km s^{-1} (with Hanning smoothing) for Bands 3 to 7, respectively. Only a few setups in Band 7 (B7g to B7p) had some spectral windows set to a resolution of 1.128 MHz. Final products were produced at a coarser uniform velocity resolution during imaging (Sect. 3.2).

2.2. Sensitivity

The targeted brightness temperature sensitivity of the survey was 50, 50, 40, 30, and 30 mK in 10 km s^{-1} channels across ALMA Bands 3, 4, 5, 6, and 7, respectively. This was a compromise to achieve a deep uniform sensitivity across all bands while keeping an achievable ALMA time request. These brightness temperature sensitivities can be converted to point source flux density sensitivities using Eq. (3.31) in the ALMA Cycle 8 technical Handbook[1]:

$$S_\nu({\rm Jy}) = 0.0736 \left(\frac{\nu}{300\,{\rm GHz}}\right)^2 \left(\frac{\theta_{\rm max}}{1''}\right)\left(\frac{\theta_{\rm min}}{1''}\right) T_R(K). \quad (1)$$

For the originally-specified circular beam size of 1″ the approximate point source flux density sensitivities are ∼0.35, 0.9, 1.2, 1.6, and 2.3 mJy at the ALMA frequency band centers.

The flux density root mean square (RMS) values of each individual continuum subtracted spectral window were estimated from line free spectral channels. Channels showing bright line emission were masked by hand, while those showing fainter emission were eliminated by using the biweight algorithm in the CASA task *imstat* (McMullin et al. 2007). The top panel in Fig. 2 displays the measured flux density RMS of each spectral window as a function of frequency. Combined (12 m compact plus extended configurations in Band 3 or 12-m plus 7-m array data for higher frequency bands, see Sect. 2.3) sensitivities (blue) as well as the 12-m compact configuration (green) and 7-m array (red) sensitivities are shown. Figure 2 shows that for most of the survey, the achieved flux density complies with the project's original sensitivity goals. Apart from the spectral windows directly affected by the 183 GHz telluric water line (USB of B5b, B5c, and B5d, and LSB of B5e) and the oxygen and water lines at 368 GHz and 380 GH, respectively (USB of B7m and B7n), the flux density RMS noise ranges from 0.18 to 5.0 mJy beam^{-1}, with average flux density sensitivity of 1.4 mJy beam^{-1} and median of 1.0 mJy beam^{-1}. This noise is measured in the final 8−9 km s^{-1} channels (Sect. 3.2).

The bottom panel in Fig. 2 displays the 1.6″ beam (Sect. 3.2) equivalent brightness temperature noise per spectral window. The targeted brightness temperature sensitivity with a beam of 1″ is corrected by a factor of 2.56 to account for the achieved common beam of 1.6″ (Sect. 3.2). The average sensitivity is 14.8 mK with a median of 10.2 mK.

[1] https://almascience.nrao.edu/documents-and-tools/cycle8/alma-technical-handbook/view

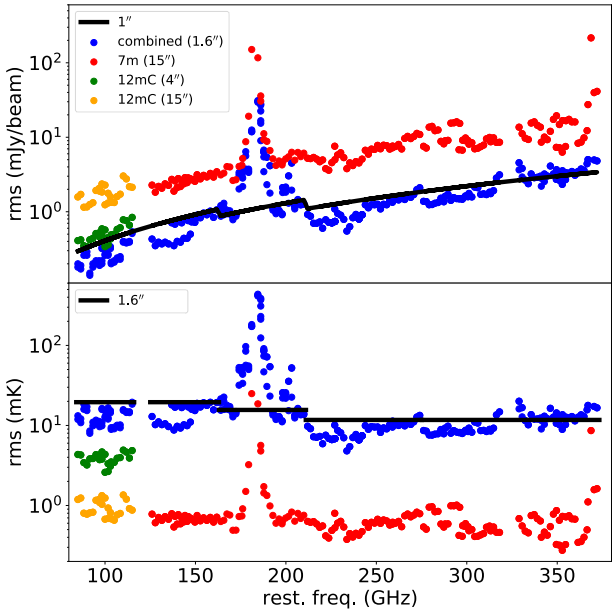

Fig. 2. Measured RMS flux density (*top*) and equivalent brightness temperature (*bottom*) noise level of each individual data cube (spectral windows) imaged for the combined arrays (blue), compact 12 m array band 3 observations (green) and 7 m array band 4 to 7 (red). Black lines correspond to the target sensitivities requested for 1″ (*top*) and 1.″6 (*bottom*) resolution imaging. Brightness temperature noise levels have been calculated for a beam of 1.6″, 4″, and 15″ for combined, 12 m compact, and 7 m array, respectively. For completeness, compact 12 m array band 3 sensitivities are also displayed (orange) for data cubes imaged at 7 m array 15″ resolution. Target brightness temperature sensitivities are scaled down to that of the common beam of 1.6″ resolution used during imaging. See Sects. 2.2 and 3.2 for details.

2.3. Maximum recoverable scales

Due to the lack of short spacings in interferometric observations, structures larger than the maximum recoverable scale (MRS) are filtered out. Following Eq. (7.6) in the ALMA Cycle 8 technical handbook[1] the MRS is defined as $\theta_{\rm MRS} \sim 0.6\lambda/B_{\rm min}$, where λ is the wavelength and $B_{\rm min}$ the shortest projected baseline.

Based on the extent of the CO $J = 1-0$ emission (Meier et al. 2015), ALCHEMI targeted an MRS of 15″ across its entire frequency coverage. This corresponds to spatial scales of up to ∼250 pc, which should recover most of the emission from the GMCs in the NGC 253 CMZ. These spatial scales also correspond to one fourth of the region enclosed within the ILR (Sect. 1) and are similar to the length of the 120−320 pc filaments tracing the molecular outflow (Bolatto et al. 2013). In Band 3, our required MRS could be achieved with the extra-compact 12-m array configuration, but additional observations with the ACA 7-m array were required for Bands 4 through 7. Figure 3 displays the MRS for each of the individual 12-m and 7-m array observations. The targeted MRS was achieved across the entire ALCHEMI spectral coverage, ensuring that $\lesssim$15″ scales are recovered throughout the survey. We note however that at the lower frequencies, scales larger than 15″ could also contribute to the observed emission. In that sense, the survey is not strictly homogeneous, although this could be corrected, if deemed important for a given science case, by cropping the visibilities within a given *uv* radius. Based on the results presented in Sect. 4, we expect only minor contributions from structures larger than our expected MRS of 15″, with the exception of CO transitions.

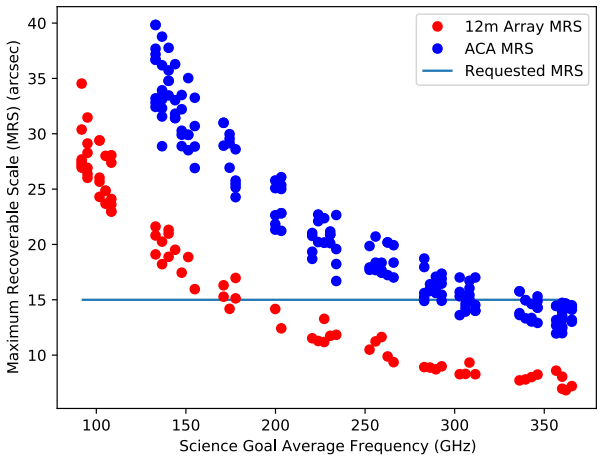

Fig. 3. Maximum recoverable scale per channel estimated for each individual 12-m (red) and 7-m (blue) array observations (Sect. 2.3). Each point corresponds to an individual execution centered at the average frequency of all four spectral windows (thus the gaps that appear in some frequencies). The targeted 15″ maximum recovered scale is represented by an horizontal black line.

3. Data calibration, equalization, and imaging

Calibration and data quality assessment were performed by ALMA staff. For all but a couple of scheduling blocks the ALMA calibration pipeline was used. A summary of the calibrators used within each scheduling block is provided in Table A.2.

3.1. Flux calibration accuracy

According to the ALMA Cycle 5 Proposer's Guide[2], delivered absolute flux calibration should be better than 5% for Bands 3, 4 and 5, and 10% for Bands 6 and 7. The flux calibration method adopted by ALMA (described in Guzmán et al. 2019) uses regularly-monitored fluxes from a catalog of secondary flux calibrators to set the flux calibration scale for all science measurements. One or more secondary flux calibration sources are measured with each science scheduling block. The absolute flux scale for the secondary calibrators are determined through almost simultaneous measurements of primary flux calibrators (solar system objects, including Uranus, Neptune, Callisto, Ganymede, and Mars) with a monitor cadence of 10−14 days. The accuracy of this flux calibration scheme has not been fully assessed, and recent studies suggest that the ALMA flux calibration uncertainty can be significantly worse than that stated in the ALMA user guidelines (Francis et al. 2020; de Kleer et al. 2021).

Taking advantage of the multiple contiguous frequency tunings of the ALCHEMI data set across the five covered frequency bands, we are able to further estimate the relative flux calibration accuracy of the individual frequency tunings. Prior to this analysis, data were cleaned and preliminary imaging was performed to a common beam as described in Sect. 3.2. Two independent methods were used to check the relative flux alignment. We derived amplitude scaling factors between tunings (Table A.1), based on overlapping channels (Sect. 3.1.1). The relative continuum level was then used to double check the accuracy of our spectral flux alignment (Sect. 3.1.2).

[2] https://almascience.nrao.edu/documents-and-tools/cycle5/alma-proposers-guide/view

For a target source with strong continuum and a significant amount of spectral line emission within each independent frequency tuning, absolute flux calibration precision is required. Accurate absolute flux calibration minimizes amplitude misalignment in the final concatenated spectrum as well as assures a high level of accuracy when comparing spectral line fluxes derived from different frequency tunings. As shown by Harada et al. (2018), for spectra with a low density of spectral lines per sampled frequency bandwidth, one can derive and subtract the continuum emission first within individual tunings. This continuum information can then be used to perform an amplitude rescaling, followed by concatenation of the continuum-subtracted spectra from each frequency tuning to achieve accurate relative flux scaling and minimal gaps at the frequency tuning boundaries. Subtraction of a smooth continuum from a spectrum with a high density of spectral lines, on the other hand, cannot extract the necessary continuum emission information in order to use this flux rescaling technique. We describe a method to improve the flux calibration accuracy of our ALCHEMI spectra when there is a high density of spectral lines in Sect. 3.1.1.

In Appendix B we show the unscaled spectra where only the standard ALMA pipeline calibration has been applied to the data. As evidenced by Figs. B.1 through B.7 and in the scaling factors in Table A.1 some of the misalignment between adjacent receiver tunings are beyond nominal calibration uncertainties. In Appendix C we provide an analysis of the relative and absolute flux calibration uncertainties for all ALCHEMI image cubes.

The two methods used below assume that flux calibration has no systematic bias, or said otherwise, cannot account for systematic biases in the fluxes accross the spectral scan. In fact, our analysis suggest that for absolute flux calibration an overall uncertainty of 15% is justified and appropriate. However, the derivation and application of the amplitude scaling factors has allowed us to improve the relative flux calibration accuracy beyond that which a single ALMA scheduling block might normally attain. The relative flux calibration scaling factors listed in Table A.1 were applied to the originally calibrated visibilities prior to final imaging. In the analysis presented in this paper (Sect. 4), only the statistical uncertainty in the fits due the noise in the spectra are considered and not the absolute flux calibration uncertainty mentioned above, which is enough for our purposes.

3.1.1. Overlapping channels alignment

As the ALCHEMI spectra toward NGC 253 in many cases possess a high degree of spectral crowding, we refined our flux calibration by using the target signal itself as reference. This technique, originally developed for other ALMA spectral scans, is referred to as "flux self-calibration" (Sakamoto et al. 2021). Below we recapitulate the technique details fully described there.

The amplitude re-scaling in this technique is based on a comparison of the initial spectra at their overlaps, which as described in Sect. 2.1 has been built-into our scheduling block tuning setup for this purpose. For the choice of the reference signal it does not matter whether the emission at that position is dominated by continuum or spectral line emission as long as it is reasonably spatially compact and presents no time variability over the observation period. This is due to the fact that a pair of frequency tunings is always compared at their overlapped frequencies, using the same emission from each frequency. Furthermore, the ALCHEMI spectra have been produced with the same spatial resolution across each spectral scan, so that the two observations being compared should possess approximately the same range of baseline *uv* lengths at their respective overlapped frequencies. This flux self-calibration through overlapping tunings can therefore be used on targets with numerous broad lines with a limited number of line-free channels. A single scaling factor is derived for each tuning, shared by all the spectral windows in that tuning. It is important to note that the flux scales for individual spectral windows within a given sideband align to $\lesssim$1%.

As indicated in Sect. 2.1 our frequency setup included a 100−200 MHz overlap among contiguous frequency tunings. In order to derive the flux rescaling factors for each frequency tuning and array configuration, we assigned to each frequency tuning a scaling factor a_i, where i is the scheduling block ID (Col. 1 in Table A.1). For each set of adjacent tunings we then solved (with the least squares method when necessary) a set of equations given by:

$$r_{ij} = \frac{a_i}{a_j}, \tag{2}$$

where r_{ij} is the measured amplitude ratio between the independent frequency tunings i and j. The spectra extracted from the TH2 position (α_{J2000} = $00^{\rm h}47^{\rm m}33.182^{\rm s}$, δ_{J2000} = $-25°17'17.148''$; Lenc & Tingay 2006) within the preliminary imaged data cubes was used as the reference measurement in Eq. (2). We used the constraint mean(a_i) = 1 to set the overall scale of the solutions, resulting in the flux self-calibration rescaling factors listed in Table A.1. These flux rescaling factors were applied to the calibrated visibilities before final imaging using the CASA task *gencal* as follows:

$$A_{uv}^{\rm final} = \frac{A_{uv}^{0}}{a_i}, \tag{3}$$

where A_{uv}^{0} and $A_{uv}^{\rm final}$ are initial ALMA delivered and final *uv* amplitudes. As evidenced by the scaled spectra shown in Figs. B.1 through B.7 the rescaled spectral image cubes are in most cases well-aligned in amplitude.

3.1.2. Continuum level alignment

We can use the continuity of the spectral energy distribution of the continuum emission to verify the relative amplitude scaling of the different tunings. One advantage of this method is that it can make a bridge across bands and gaps in the frequency coverage (Sect. 2.1) which is an intrinsic uncertainty when using overlapping channels (Sect. 3.1.1). The continuum emission is measured on the STATCONT continuum cubes (Sect. 3.3), after the first amplitude scaling derived from the overlapping channels alignment process (Sect. 3.1.1). While the amplitude scaling was applied per tuning, here we measure the continuum emission for each individual spectral window. The position TH2, close to the continuum emission peak, is also used as in Sect. 3.1.1. At this step, we do not want to introduce a complicated fit of the overall SED, so we simply use a third order polynomial to estimate the standard deviation of the continuum levels with respect to a smooth and continuous function. This strategy allows us to test the robustness of the channel-overlapping scaling by checking "residual" scaling factors (i.e., if the channel-overlapping scaling was perfect across all data, then those new factors would be all equal to one).

We have run this method on both the 7m-array and 12m+7m array cubes separately. After removing a few spectral windows close to the 183-GHz telluric water line (in Band 5), which appear as clear outliers, we find that the standard deviation of the new scaling factors is 2.5% across all bands, for both 12m+7m

and 7m array data. We can thus take this value as the maximum additional error after the channel-overlapping scaling, since the STATCONT cubes may introduce some uncertainty due to line crowding and imperfect continuum estimation. Alternatively, this result suggests that the continuum determination is relatively robust and uniform over spectral windows. We note that the dispersion increases slightly toward the highest frequency edge for the 7m-array data, as the RMS of the new scaling factors for Band 7 alone goes to 3.5%.

3.2. Imaging

Before imaging, several homogenization corrections were applied to all ALCHEMI data sets in order to produce a uniform science archive. In addition to the normalization of the amplitude scale in each tuning using the procedure described in Sect. 3.1.1, all measurement sets were binned to a common velocity scale. A common velocity scaling was produced by binning to frequency resolutions of 3, 5, 6, 8, and 10 MHz for Bands 3, 4, 5, 6, and 7, respectively, which is equivalent to an approximately common velocity resolution of ∼8−9 km s^{-1} in the LSRK velocity reference frame. Once homogeneity in amplitude scaling and velocity resolution was attained, the CASA task *tclean* was used to produce image cubes of each tuning spectral windows. The specific *tclean* parameters used for imaging were catered to the needs of individual spectral windows as follows.

The cell and image sizes used for imaging each array and frequency band were as follows: 7m Array observations used cell = 0.4 arcsec and *imsize* = [320, 320] pixels for all frequency bands; 12m Array and the combined 7m+12m data sets used *cell* = 0.15 arcsec for all frequency bands and *imsize* =[800,800], [800,720], [720,648], [640,512], and [640,512] for Bands 3 through 7, respectively. Automasking was used for clean region selection

Based on *tclean* dry-runs of the ALCHEMI measurements containing known strong spectral features (i.e. CO 2 − 1), a list of line-free spectral channel RMS values for those spectral windows was developed to use as input for the *tclean* parameter *threshold*. This was necessary to allow for the proper cleaning of spectral windows where strong spectral lines amplify imaging artifacts, causing the single channel noise values near strong spectral lines to be anomalously high. For spectral windows which contained strong spectral lines, the predetermined spectral channel RMS values were used to set the *tclean* threshold, leaving the *nsigma* parameter unset. For spectral windows which did not contain strong spectral lines, the *tclean* parameter *nsigma=2* was set, and the *threshold* parameter was left unset. Spectral channel flagging was performed on those spectral windows which contained clear absorption due to telluric oxygen and water (see Sect. 2.1).

The *hogbom* deconvolver function was used for all spectral windows. The *mosaic* gridder was used for spectral windows comprised of multiple pointings, while the *cube* gridder was used for Band 3 and all ACA spectral windows as these measurements required only a single pointing (Sect. 2). Robust (Briggs) weighting was used with a robust parameter of 0.5 for most spectral windows. In order to produce images with resultant spatial resolution of 1.6″, a few tunings required alternate robust parameters for each of the four spectral windows, and in three cases *uv* range settings: B3b used robust = [0.4, 0.5, 0.5, 0.5]; B3c used robust = [0.25, 0.5, 0.5, 0.5]; B3f used robuts = [0.0, 0.0, 0.5, 0.5]; B5d used robust = [0.0, −2.0, 0.5, 0.5] and uvrange > 20 $k\lambda$; B5e used robust = [−2.0, −2.0, −2.0, −2.0] and uvrange > 25 $k\lambda$; B5f used robust = [−2.0, −2.0, −2.0, −2.0] and uvrange > 50 $k\lambda$.

The originally requested angular resolution was 1″ (17 pc). However, the synthesized beams of each individual spectral window significantly varied between frequency setups and between individual spectral windows in the upper and lower sidebands due to the effective antenna configuration used for each observation. This fact did not allow the imaging of the entire survey at the targeted spatial resolution. In order to produce a homogeneous data set, with data cubes sharing a uniform spatial (and spectral) resolution over all frequencies, a common final spatial resolution of 1.6″ (28 pc) was selected, corresponding to that of the data cube with the coarsest resolution in the survey. Post-imaging convolution using the CASA task *imsmooth* was therefore performed to produce final image cubes with a fixed Gaussian circular beam of 1.6″.

Additional data cubes were generated for the compact 12-m array observations at Band 3 and the 7-m array observations for Bands 4 through 7. Data were imaged with a common restoring beam of 4″ and 15″, respectively, for these two compact array configurations.

3.3. Continuum subtraction

It was determined that it would be inefficient to subtract the continuum in the *uv* plane from the individual 188 data cubes constituting the ALCHEMI measurement set. The large velocity gradient across the field of view and the significant cumulative line contribution even in the low resolution data (Sect. 4.2) makes it difficult to accurately identify line free windows to perform the continuum subtraction in the *uv* plane for all data cubes. Therefore, for consistency across the entire survey, continuum emission was statistically derived from each individual spectral window using STATCONT (Sánchez-Monge et al. 2018) to derive and subtract the continuum on a per pixel basis from each image cube. Sigma-clipping continuum determination was used with the default parameter (α = 1.8, see Sánchez-Monge et al. 2018, for details).

Continuum subtraction was performed on both the initial input data cubes used to feed the flux level alignment and also on the final amplitude-scaled data (Sect. 3.1). The per-pixel continuum estimation was thoroughly tested and provides good overall results. Since the algorithm was mostly tuned to confusion limited Galactic sources with relatively narrow spectral line emission, we observe that the continuum appears slightly overestimated in the regions of spectra with higher noise levels. For example, the continuum level appears to be overestimated near the 183 GHz telluric water line and at the upper end of Band 7 (>335 GHz). More importantly, continuum subtraction is seen not to be optimal for spectral lines close to the noise level. In such cases, continuum subtraction in the *uv* plane or subtraction of a spectral baseline in the image plane using a narrow window around the lines of interest may be needed for accurate imaging.

3.4. Self-calibration

It is foreseen that the ALCHEMI data set will eventually be improved with self-calibration of both the ACA and 12m Array measurements. However, the data in this article and the data that will initially be publicly released from this ALMA large program will not include self-calibration. The ALCHEMI research collaboration intends on providing a subsequent version of the ALCHEMI image cube archive which includes the application of

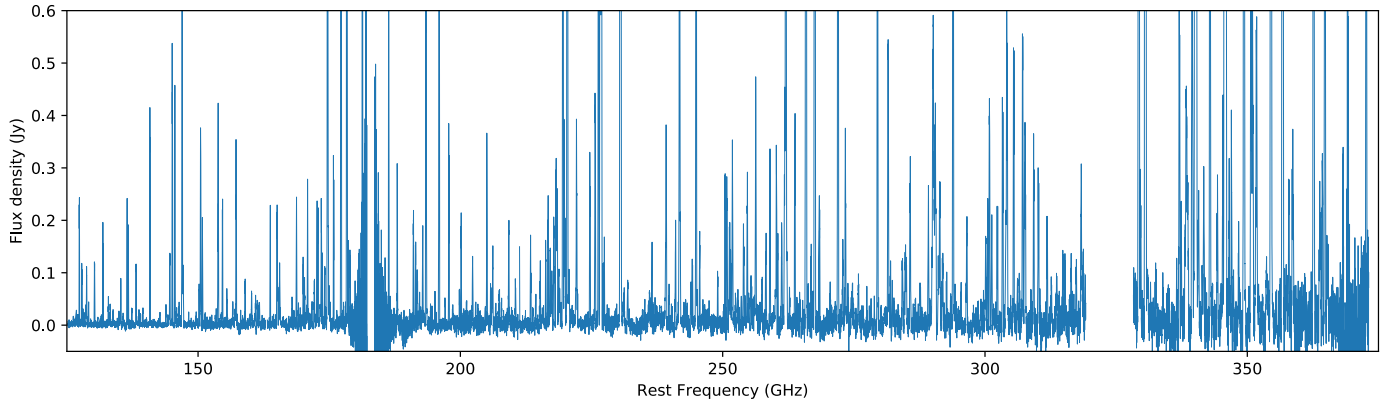

Fig. 4. Full spectral coverage obtained with the ALMA Compact Array (ACA 7m) alone, extracted from the position of brightest molecular emission (see Sect. 4.3.1). Figure F.1 presents a zoomed version of this plot in five frequency windows 50 GHz wide where the comparison with the modeled emission (Sect. 4.3.2) and the molecular line identification of each individual feature is included. Figures F.2–F.11 present a further zoomed version in 5 GHz windows.

self-calibration. It is important to note that self-calibration may have an impact on the absolute flux calibration of the ALCHEMI measurements. As a result, we emphasize that the amplitude scaling factors derived in Sect. 3.1 will need to be recalculated after self-calibration of the ALCHEMI data.

4. ACA data: Analysis and first results

While Sect. 2 describes the observational details of the full ALCHEMI survey, here we focus on the ACA 7-m (Morita) array alone. The ACA data allow us to probe the global properties of the molecular emission of the CMZ in NGC 253. This provides a template for subsequent analysis of the high resolution data to compare molecular abundances on individual GMC size scales to those on the larger size scales probed by the ACA.

The frequency coverage of the ACA data in this analysis is limited to the 256.7 GHz surveyed with this array; ALMA Bands 4 to 7 between 125.2 and 373.2 GHz. Figure 4 presents an overview of the survey. As indicated in Sect. 3.2, a homogeneous reconstructing beam of 15″ was used across the entire frequency range. This resolution is roughly equivalent to that of the 2 mm (i.e., ALMA Band 4) spectral survey in Martín et al. (2006) carried out with the IRAM 30-m single-dish telescope. However, in contrast to single-pointing surveys with single-dish telescopes for which the resolution changes as a function of frequency, our ACA interferometric observations allow for uniform spatial resolution across the entire frequency coverage.

The point-source flux density sensitivity of the ACA data alone (Fig. 2, top) is lower than that of the combined data presented in Sect. 2. If we exclude the noisy data sets at the highest frequencies (i.e., USB of B7m and B7n), sensitivities range between 1.8 and 19.4 mJy beam^{-1} across the survey, with an average RMS of 7.8 mJy beam^{-1} and a median of 7.5 mJy beam^{-1}. For the 15″ synthesized beam, using Eq. (1), those values correspond to equivalent point-source brightness temperatures between 0.27 and 1.0 mK, and an average of 0.6 mK.

4.1. Continuum emission

Having continuous frequency coverage over ∼260 GHz ranging from 2 mm to 850 μm (resulting in $\Delta\nu/\nu \simeq 1$ at the central frequency of the survey) allows us to study the spatially averaged continuum spectral energy distribution (SED). This frequency range is particularly interesting because we can probe the Rayleigh-Jeans (RJ) tail of the dust emission as well as the free-free continuum emission from ionized gas and, to a lesser degree, synchrotron emission from nonthermal sources in the CMZ of NGC 253.

Continuum emission is barely resolved at our 15″ resolution as derived from the two sample STATCONT continuum product images at 198 and 350 GHz. The 2D Gaussian fit to both continuum images yields a similar 18″ × 14″ ($FWHM$; PA = 55°) emission extent which hints at some elongation along the major axis of the CMZ. In Fig. 5, we show the continuum emission as derived from STATCONT (Sect. 3.3) for each spectral window at the pixel position analyzed in this article (Sect. 4.3.1). Although this is not strictly an SED ($\nu\ F_\nu$ vs. $\log(\nu)$) we will refer as such in the following. Due to the slightly extended emission compared to our spatial resolution, if the continuum is measured integrating over an aperture larger than the beam instead of using the continuum value at the emission peak, a similar SED shape is obtained but with 15−20% larger flux densities. The SED was calculated from amplitude-aligned data cubes on overlapping channels (Sect. 3.1.1). Thus, the SED is spectrally smooth except for the regions in which the spectra are noise dominated such that STATCONT did not accurately fit the continuum (Sect. 3.3). Such is the case with the apparent drop in continuum intensity due to the higher noise in the measurements around the telluric 183 GHz H_2O transition in Fig. 5.

The observed curvature of the continuum SED in Fig. 5 fits well to a graybody with dust temperature $T_\mathrm{d} = 42 \pm 1$ K, mass $M_\mathrm{d} = 8.0 \pm 0.2 \times 10^5\ M_\odot$, emissivity $\beta = 1.9$ (i.e., $S \propto \nu^{3.9}$), and a mass opacity coefficient of dust, $\kappa_\nu = \kappa_0(\nu/\nu_0)^\beta$, where $\kappa_0 = 0.1\,\mathrm{cm^2\,g^{-1}}$ and $\nu_0 = 250$ GHz (e.g., Cao et al. 2019), plus a free-free component to account for the lower frequency emission with SFR = 2.5 $M_\odot\,\mathrm{yr^{-1}}$ and $T_e = 10^4$ K ($S \propto \nu^{-0.1}$, using Eq. (3) in De Zotti et al. 2019).

The dust temperature was fit to the data in Fig. 5 using Herschel observations (with no aperture correction applied) at high frequencies, finding good agreement with the cold component fit of 37 K by Pérez-Beaupuits et al. (2018). Similarly the derived mass agrees well with the Pérez-Beaupuits et al. (2018) value of $1 \times 10^6\ M_\odot$ if we correct our estimate to account for the extra 20% flux from extended emission in our data (see above). The higher temperature components derived by Pérez-Beaupuits et al. (2018) are negligible at our observed

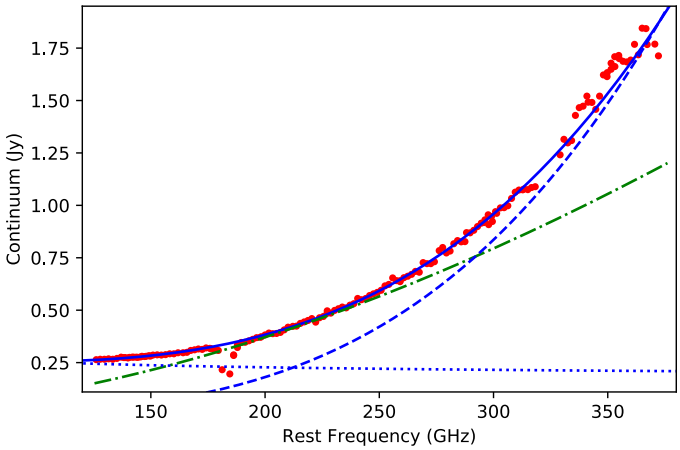

Fig. 5. Continuum flux density at the peak of emission as derived from each spectral window across the surveyed frequency range (red dots). We note that extended emission in our data might account for up to ∼20% higher fluxes (Sect. 4.1). A fit to the data is shown by a continuous blue line, which is the combination of the free-free emission (dotted blue almost horizontal line) and the graybody emission (dashed blue line). See text for further details on parameters used. As a reference to illustrate the deviation from pure black body emission, that for a $T_{\rm d}$ = 50 K and 0.5″ source size is shown as a green dot-dashed line.

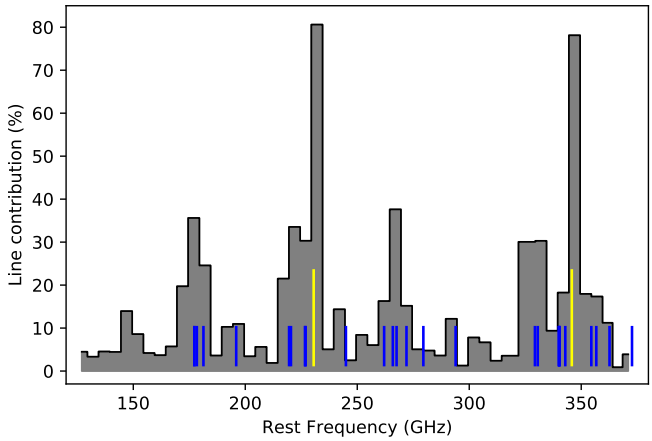

Fig. 6. Spectral line contribution to the continuum flux in 5 GHz bins. The position of spectral features brighter than 1 Jy are shown as blue segments at their corresponding frequency, with the two CO $J = 2 - 1$ and $3 - 2$ transitions displayed in yellow.

frequencies. Dust emissivity (β = 1.9) based on this data agrees well with that derived by Rodríguez-Rico et al. (2006).

Synchrotron emission was also included in the fit shown in Fig. 5 based on Eq. (1) in De Zotti et al. (2019) which considers a steepening of the emission above 20 GHz. Since we assumed a SFR=2.5 $M_\odot\,{\rm yr}^{-1}$ the synchrotron emission at our observed frequencies is negligible compared to that due to free-free emission. However, our assumed SFR is slightly higher than that derived from radio recombination lines (∼1.7 $M_\odot\,{\rm yr}^{-1}$: Kepley et al. 2011; Bendo et al. 2015) or the SFR of ∼1.7 $M_\odot\,{\rm yr}^{-1}$ derived from a fit to the free-free emission by Rodríguez-Rico et al. (2006). The power law emission resulting from the combination of synchrotron and free-free emission can only be disentangled with observations at lower frequencies not covered by the ACA data in this article.

4.2. Line contribution to broadband continuum emission

Observations with broad, coarse spectral resolution mm and submm continuum detectors such as bolometers may suffer from contamination by spectral line emission. The 40-GHz-wide spectral scan at 1.3 mm toward the ULIRG Arp 220, reported a line contribution to the total observed flux of ∼28% (Martín et al. 2011). The wide spectral coverage ALCHEMI data set allows us to investigate the typical line contamination for a starburst galaxy like NGC 253. In order to obtain the spectral line contribution to the total emission per frequency band, we calculated the average flux density over the continuum subtracted spectrum and divided it by the observed average flux density (continuum plus line emission) over the same band. Results are shown in 5 GHz bins in Fig. 6 and averaged over 50 GHz bands in Table 2.

Similar to the results for Arp 220, we observe a significant contribution from spectral lines to the continuum-integrated flux density in NGC 253. Most of the contamination is due to the brightest lines in the band, as shown by color segments in Fig. 6, but there is also a significant contribution from the forest of weaker lines. The line contribution, both in narrow 5 GHz and broad 50 GHz bins, ranges from a few percent up to a third of the measured flux density, and up to 80% in narrow ranges containing CO transitions. We note that the CO contribution over the 50 GHz band considered in Table 2 would account for 8% in both Bands 6 and 7, similar to what was reported toward Arp 220 (Martín et al. 2011), while the remaining contribution of up to ∼35% corresponds to emission from other species.

Table 2. Line contribution to the observed flux density.

Frequency range (GHz)	$S_{\rm Total}$ [a] [mJy]	$S_{\rm Molec}$ [mJy]	Line contribution [%]	Line density [b] [GHz^{-1}]
125−175	308	23	7.6	7.7
175−225	437	70	16.1	7.4
225−275	921	322	35.0	8.4
275−325	987	53	5.3	5.8
325−375	2488	909	36.6	6.5

Notes. The numbers in this table are exclusively based on ACA data, thus not including Band 3. See Sect. 4.2 for details. [a]Total flux density corresponds to the contribution from both continuum and line emission. [b]Only spectral lines >2 mJy included in this calculation.

Both this work and that on Arp 220 can now serve as a reference for evaluating the line contribution to broadband continuum observations (i.e., with too coarse spectral resolution to resolve the lines) and considering corrections to broad continuum observations over ALMA Bands 3 to 7 (rest frame), and correspondingly to the spectral index derived from those measurements. Such corrections may be particularly relevant for high-redshift galaxies showing a nuclear starburst contribution.

4.3. Molecular emission analysis

4.3.1. Selected sample position

In order to analyze the global molecular emission of the CMZ in NGC 253, we targeted the peak of the molecular emission in the 15″ resolution data. To select this position, the pixel of peak emission was measured for each of the moment 0 maps from 16 of the brightest transitions in the survey shown in Fig. 7. The spectra analyzed in this article were extracted from the pixel at

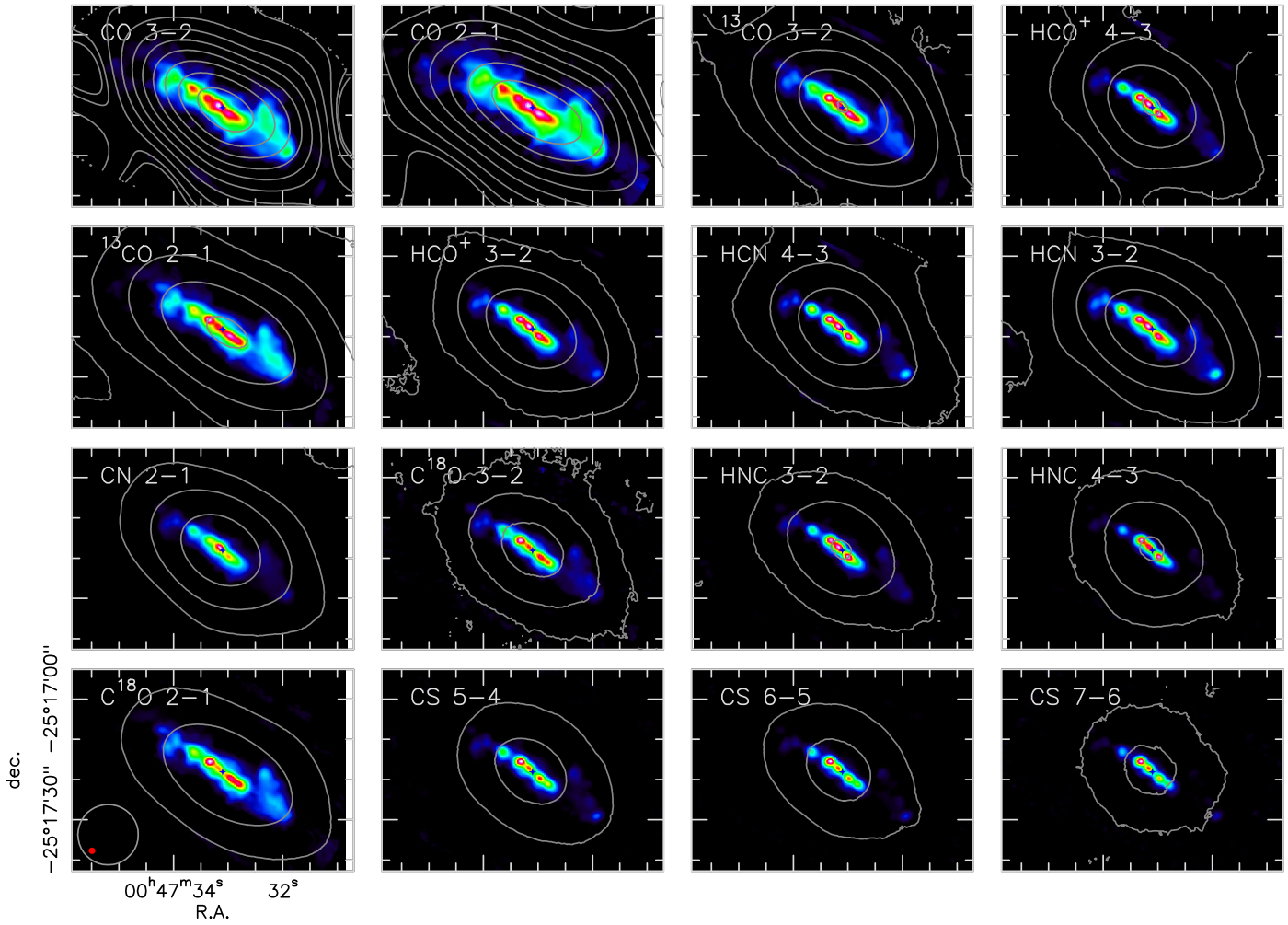

Fig. 7. Sample of integrated flux density moment 0 maps from 16 of the brightest molecular transitions in the covered frequency band. Each panel is labeled with the corresponding molecular species and transition. We point out that CO 1 − 0 is not included since Band 3 is not covered by the ACA data. In color the combined 12 m+7 m maps are shown where the color coding is adjusted for visibility of each individual species. Gray contours show the 7 m integrated intensity images where the n-th contour level corresponds to 20 n^3 Jy km s^{-1} beam^{-1} for all species. Species are ordered in decreasing order of integrated flux density *from left to right* and *from top to bottom*. The panel in the *lower left* shows the reference coordinates and the beam size of the combined 12 m+7 m (1.″6, filled red circle) and 7 m data (15″, gray line), which are shared by all tunings. The blue cross at the center of every map shows the selected position (Sect. 4.3.1) from which we extracted the spectra for modeling (Sect. 4.3.2) and for presentation in Fig. 4.

position α_{J2000} = 00^{h}47^{m}33.^{s}10, δ_{J2000} = −25°17′18.″1, corresponding to the average of all measured peak emission pixels and shown as a blue cross in Fig. 7. This position is just ∼1.5″ away from the giant molecular cloud analog Region 5 from Leroy et al. (2015) and ∼1.4″ from TH2 (Turner & Ho 1985).

We note that despite the different spatial distribution among species observed at the high resolution data, the brightest pixel in these ACA images agrees well among all images. Peak positions deviate from the average of all peak positions within an RMS of 0.8″ (∼2 pixels), and/or within 0.65″ (∼1.5 pixels) if we exclude the two CO transitions, whose emission structure is significantly affected by opacity and overall extended emission.

4.3.2. Line identification and LTE modeling

In this section we describe the overall criteria for molecular line identification and modeling. Further specific details on the fitting of individual species are provided in Appendix D. We emphasize that we did not analyze individual spectral features, but modeled the emission of all spectral lines within the surveyed band at once for each species. Therefore, line identification is done per molecule and not per transition, which is more robust and makes use of the broad frequency coverage in this work. Line flux densities reported in this paper are those from fits to the molecule transitions and accounts for line blending. We do not report the measured flux of each individual spectral feature.

Molecular emission has been identified and modeled under local thermodynamic equilibrium (LTE) conditions using MADCUBA[3] (Martín et al. 2019a) where physical parameters of column density, excitation temperature, radial velocity, line width, and source size are used to fit a modeled synthetic spectrum to the observations. Spectroscopic parameters required for LTE modeling in MADCUBA, and therefore all the frequencies reported in this paper, are extracted from the CDMS (Müller et al. 2001, 2005; Endres et al. 2016) and JPL (Pickett et al. 1998) catalogs.

[3] MADCUBA VERSION 6.0 (07/05/2018). https://www.cab.inta-csic.es/madcuba/index.html

One of the visual advantages from fitting through synthetic spectra is that non-LTE emission or just spectral lines not properly fit under the LTE assumption are evidenced by line intensities significantly deviating from the LTE fit, which is often overlooked in the log-log representation in rotational diagrams. As explained in Appendix D, the LTE approximation appears to work well to describe the vast majority of observed spectral features modeled in this analysis, and the most obvious deviations from the fit are also identified.

The spectra extracted at the selected position (Sect. 4.3.1) show a double peak profile which is the result of the convolution of the molecular distribution substructure observed at higher resolution (see Fig. 7). In principle, fitting a two component model would allow us to kinematically disentangle the molecular gas from both sides of the nucleus. However, the use of a multiple Gaussian fit to the overall spectrum adds little significance to the results (which will be better studied with the high resolution ALCHEMI image cubes), while increasing significantly the complexity of the modeling, even more so given that not all species show double peak profiles. For these reasons the modeling described here will consider a single Gaussian emission profile which suits the purpose of this article's focus on the global averaged properties of the molecular emission in the CMZ of NGC 253.

Among the fitted parameters, fitting the source size requires an accurate "a priori" excitation temperature for a molecule with enough optically thick transitions covering a wide range of energy levels and not too affected by spectral blending (Martín et al. 2019a). Since the broad line emission in our spectrum does not allow for an accurate constraint of the source size, we assumed a circular Gaussian equivalent source size of 5″, based on available higher resolution observations (Meier et al. 2015; Martín et al. 2019b). This parameter is not too relevant for the global relative properties analyzed in this article, as we consider a linear dependence of the derived column density with the source solid angle. It could, however, be significant for lower values of the source size, when opacity starts playing a major role as discussed in Sect. 5.4. Only in the case of the main $^{12}C^{16}O$ isotopologue did we find it necessary to assume a larger source size of 10″ to be able to reproduce the observed flux densities. A difference in the larger molecular emission extent is obvious from the contours in Fig. 7 for the CO transitions, and to a lesser extent the ^{13}CO images.

All other physical parameters mentioned above (column density, temperature, velocity, and width) were kept as free parameters when possible. For each molecule, all available transitions within the covered frequency band were used for the fit, except those heavily blended or not detected above the noise level ($<3\sigma$). In some cases, for species with many transitions, only a subset of the brightest unblended transitions were used to avoid the fit being dominated by faint transitions too close to the noise level or residual emission from other species. When line blending or signal-to-noise did not allow fitting the line velocity and width, parameters were fixed to $v_{\rm LSR}$ = 230 km s^{-1} and $\Delta\ v_{1/2}$ = 150 km s^{-1}, which are the average fitted parameters to the brighter transitions. Similarly, when detected transitions did not allow the excitation temperature to be determined, the excitation temperature was set to $T_{\rm ex}$ = 15 K, which is the median of the measured temperatures in all species allowing such a fit (ranging between 5 and 60 K). Additionally, whenever any of these parameters (with the exception of the column density) were derived from a given species, these values were used to obtain more appropriate parameters to be fixed in the fit to their rarer isotopologues or isomers. This allows for a better relative abundance comparison between related species, while no biases resulting from this assumption are obvious in our derived values.

The final model includes 146 species with a total of 42121 transitions. However, only 78 species are considered firmly or tentatively detected, accounting for 1790 transitions with flux densities above 2 mJy in the model. We note that 2 mJy corresponds to 1σ at the lowest frequencies and $\sim(1/3)\sigma$ for the majority of the survey. However, the sum of faint transitions (even below the noise level) is relevant since in some cases they add up to detectable features or may significantly contaminate other transitions. The detected molecule count includes isotopologues and vibrational states. In addition multiple hydrogen and helium recombination lines from Hnα, Hnβ, and Henα were also detected throughout the survey but are not discussed in this article.

The criterium for detection of a given species has been based on its LTE model and fit results. A species has been considered detected if all the detectable transitions above 5σ (according to the LTE model), which are not blended with brighter transitions, are detected in our data. Additionally we required the convergence of the fitting algorithm within MADCUBA to avoid subjective biases.

Table A.3 shows the result from the fit to all detected or tentatively detected species in this survey. As previously indicated in Sect. 3.1, reported uncertainties do not include calibration uncertainties but statistical uncertainty on the fit to the spectra. Values with no errors in Table A.3 represent parameters that were fixed during the fitting process.

Figure 8 shows a graphical summary of the number count in flux density bins and in narrow 5 GHz frequency bins of the transitions in the model. Table 2 also includes the density of spectral lines over wider 50 GHz frequency ranges.

Finally, we point out that there are still a number of clearly detected spectral features which are not accounted for by our model as seen in the figures in Appendix F. These unidentified features may stem from emission out of LTE or the effect of multiple molecular components (Aladro et al. 2011b) or from species not included in our model. We evaluated each of these features for emission from different species, but a model to the candidate species could not be found to fit across the whole frequency range covered.

4.4. New extragalactic molecular detections

Despite the moderate sensitivity of the ACA observations, the broad frequency coverage and the bandpass stability allowed us to probe a number of newly detected species in the extragalactic ISM.

In this paper we report the first extragalactic detections of $H_2^{13}CO$, ethanol (C_2H_5OH), ^{13}CCH, $C^{13}CH$, HOCN, the three ^{13}C isotopologues of CH_3CCH, propynal (HC_3HO), and tentatively $Si^{17}O$ (see discussion in Sect. 5.4.2). Specific details on the fit to C_2H_5OH, HOCN, and HC_3HO are provided in Appendix D.1. Additionally, we confirm previous tentative detections of $H^{15}NC$ (Muller et al. 2006), $^{13}CH_3OH$ (tentatively detected toward NGC 253 by Martín et al. 2009a, and recently reported toward PKS1830-211 by Muller et al. 2021), and HC_5N (Aladro et al. 2015; Costagliola et al. 2015). These detections consist of isotopologues and isomers of previously detected species, as well as new complex organic molecules (COMs, 6+ atoms, Herbst & van Dishoeck 2009). Species like formic acid (HCOOH), very recently reported toward an absorption system (Tercero et al. 2020), is detected for the first time in emission

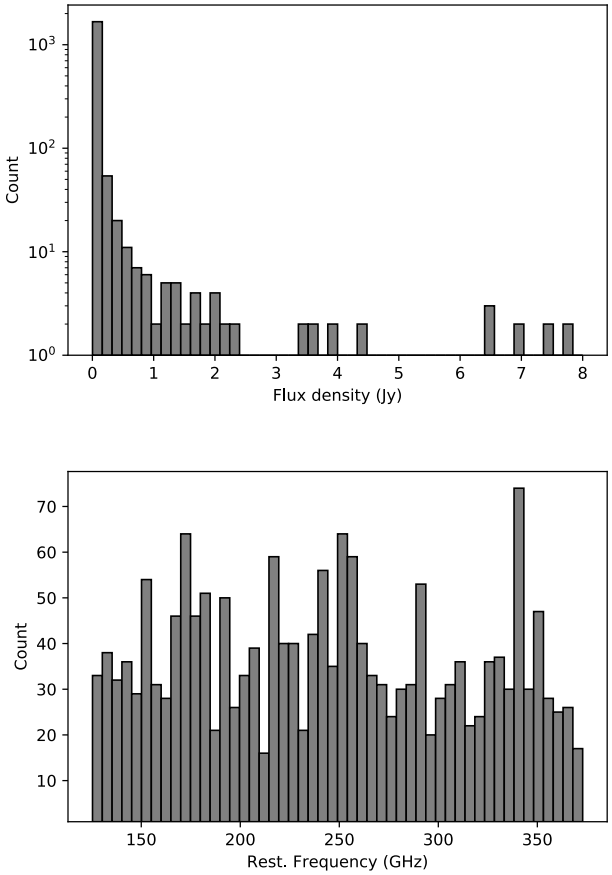

Fig. 8. *Top*: histogram showing the number of spectral lines above 2 mJy in the model in bins of flux density. Lines between 2 mJy and 10 Jy are considered. The three spectral features with flux densities above 10 Jy are not included in this diagram. *Bottom*: histogram showing the number of spectral lines above 2 mJy in frequency bins of ∼5 GHz width.

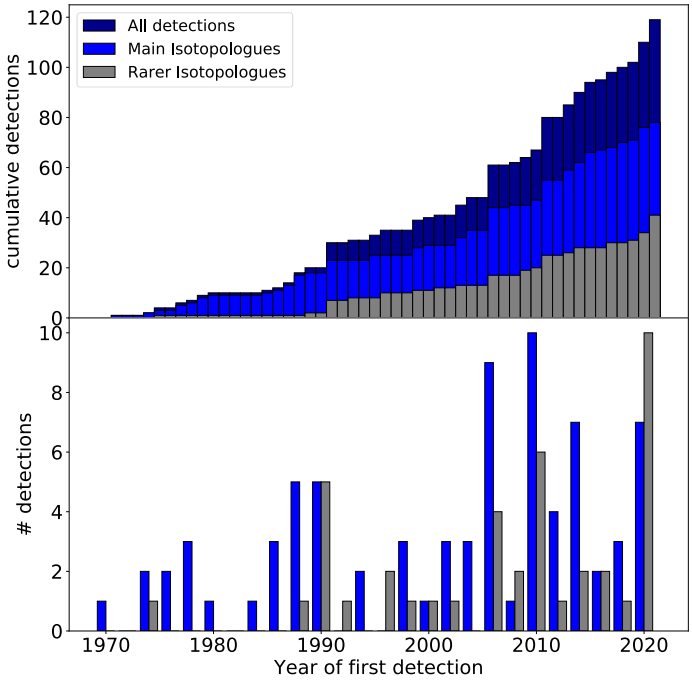

Fig. 9. Chronology of extragalactic molecular detections including those reported in this work. Detections of main and rarer isotopologue substitutions in blue and gray respectively, with the total number of detections, not considering tentative reports, being displayed in dark blue. One and two year bins are used for *top* and *bottom panel* histograms, respectively.

toward NGC 253. We also confirm the detection of the elusive methylamine (CH_3NH_2, Bøgelund et al. 2019), first detected in the extragalactic ISM in absorption by Muller et al. (2011) and so far only tentatively identified toward NGC 253 in emission by Meier et al. (2015).

The chronological evolution of the cumulative number of species detected as well as the yearly detections are summarized in Fig. 9, where the detections reported in our work are included. Details on the updated chronology of first extragalactic molecular detections are provided in Appendix E.

5. Discussion: NGC 253 as starburst molecular template

Even with its moderate angular resolution, the ACA data set provides important information on the abundance and excitation of the gas in the CMZ of NGC 253, which could not be attained by previous surveys with less complete frequency coverage (Martín et al. 2006; Aladro et al. 2015). In this section, we highlight some scientific results that make use of the wide frequency coverage of the ALCHEMI data. This unique frequency coverage allows for multitransition analysis of a variety of molecular species. The upcoming suite of papers based on ALCHEMI data will also make use of this unique wide band data set and will provide a deeper analysis of these and other scientific questions.

5.1. Extragalactic starburst low resolution molecular template

One immediate use of the wideband observations in this article is to serve as a molecular template for extragalactic starbursting environments. The large number of molecules detected in this study is a consequence of both the depth of the ALCHEMI data set and the intrinsic brightness of NGC 253. In fact, we obtained a spectral dynamic range between ∼60 000 and ∼6000, as derived by comparing the flux density of the brightest transition in the survey, CO 3−2 (see Table A.3), to the ACA-achieved noise level at Bands 4 and 7 (Sect. 4), respectively.

Figure 10 presents the number of detected unique species as a function of the flux level relative to the CO 3−2 transition (left panel) or to the brightest transition within a given Band (right panel). The data presented in Fig. 10 are based on modeled intensities from individual transitions and not spectral features (Sect. 4.3.2). Therefore the number count of species is conservative, since spectral features composed of multiple transitions (e.g., species with unresolved hyperfine structure) will rise above the noise before what is estimated based on the flux density of the brightest transition of any given moleucule. The number of detected species in Fig. 10 goes beyond the number of confirmed detections reported in Sect. 4.3.2. This is because the number of species in Fig. 10 includes recombination lines and species in vibrational states, as they are both considered to be relevant unique detections.

The data presented in Fig. 10 can be used to roughly estimate the expected level of molecular complexity achievable in a high redshift "starbursting" object as a function of the sensitivity of the observations. Of course, the main assumption relies on similar abundance and excitation conditions to those in NGC 253, which may not hold for all starburst environments

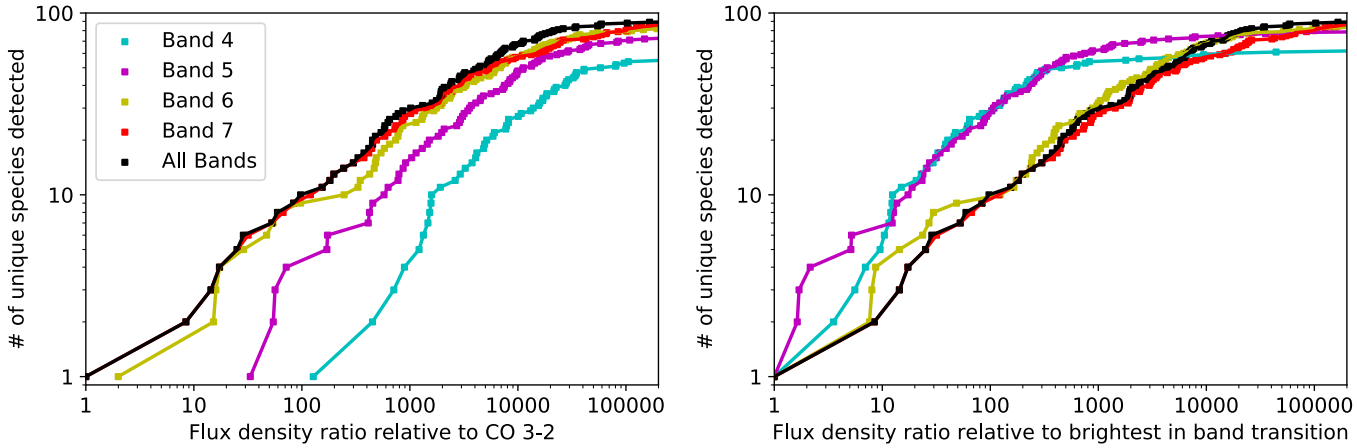

Fig. 10. Number of individual detectable species as a function of the flux density level relative to the brighter transitions detected in the survey per band. *Left*: flux density levels are referred to the CO 3 − 2 (112 Jy beam^{-1}) as the brightest transition detected in the whole spectral range covered. *Right*: flux densities are referred to the brightest transition detected on each band. This is CS 3 − 2 (0.9 Jy beam^{-1} in Band 4), HCO$^+$ 2 − 1 (3 Jy beam^{-1} in Band 5), CO 2 − 1 (56 Jy beam^{-1} in Band 6), and CO 3 − 2 (in Band 7).

(Aladro et al. 2015). Additionally, larger line widths would hamper the detectability of species due to blending.

As a test bed to show the template potential of our data set we used the stacked spectrum derived from 22 high-z sources by Spilker et al. (2014), over the redshift range $z = 2.0 - 5.7$, and covering the frequency range from ∼250 to 800 GHz. Based on their Fig. 2, the CO 3 − 2 line was detected at a signal-to-noise of ∼50. That is, observations should be able to detect emission lines ∼17x fainter if we impose a 3σ detection level. Based on our Fig. 10 (left), if we consider lines ∼17 times fainter than CO 3 − 2 (the level could be even lower considering the integrated line intensity) would result in a detection of 3-4 species. Spilker et al. (2014) reported six species above 3 σ. However, based on the mid panel in their Fig. 2, only three spectral features actually reach the 3σ level at the spectral resolution in their diagram. The increased noise in the small fraction of rest-frame Band 6 they covered resulted in no detections, also in agreement with what would be expected based on the NGC 253 template. Considering a factor of two lower sensitivity in this region, only CO 2 − 1 would be expected, and its frequency was actually not covered in their observations. This comparison shows the predicting potential of NGC 253 for molecular detections toward high-z starbursting galaxies.

5.2. Vibrational emission

Rotational transitions in vibrational states (hereafter vibrational emission or transitions) of HCN, HNC, and HC_3N, with lower energy levels of 1000, 700, and 500 K above the ground state, respectively, are clearly detected in the ACA data analyzed in this article. Vibrational emission toward NGC 253 has been recently reported at subarcsecond resolution toward individual GMCs with observations of the $J = 4 - 3, v_2 = 1f$ transitions of HNC and HCN (Ando et al. 2017; Mangum et al. 2019; Krieger et al. 2020), and two rotational transitions in multiple vibrational states of HC_3N (Rico-Villas et al. 2020). However, it was never detected in low resolution spectral scans of NGC 253 (Martín et al. 2006; Aladro et al. 2015), with spatial resolution similar to that in this work. While HC_3N emission in the $v_7 = 1$, $v_7 = 2$, and $v_6 = 1$ states is clearly detected at 0.″2 resolution (Rico-Villas et al. 2020), we only detect significant emission from $v_7 = 1$ states. We attribute this difference to beam dilution of the vibrational emission which originates from the compact GMC cores (Rico-Villas et al. 2020, 2021; Krieger et al. 2020). This is similar to what is observed within our Galaxy where vibrational emission is solely arising from hot dense material within star forming cores (de Vicente et al. 2000; Martín-Pintado et al. 2005).

The wide-band imaging of ALCHEMI data allows us to probe multiple vibrationally excited transitions of these species and to evaluate the contamination by other species. Figure 11 shows the rotational transitions of HCN, HNC, and HCO$^+$ in the $v_2 = 1f$ vibrational state. Transitions in the $v_2 = 1e$ state are too close in frequency to the rotational transitions in the ground vibrational state (see Fig. 3 in Martín et al. 2016). The derived LTE fit to the emission of all observed transitions assumes an excitation temperature $T_{ex} = 300$ K required to make these high energy transitions detectable (red line in Fig. 11). This fit clearly shows that the LTE approximation does not properly reproduce the excitation of these radiatively pumped transitions (Aalto et al. 2015). Table 3 presents the line ratio between the observed rotational transitions in the ground vibrational ($v_2 = 0$) and $v_2 = 1f$ vibrational states. As previously reported, the relative intensities between rotational transitions within a vibrational state follow that measured within the $v = 0$ rotational transitions (Costagliola et al. 2015; Rico-Villas et al. 2020), with $v_2 = 0/v_2 = 1f$ ratios relatively constant. We note that fitted column density is not physically meaningful since it requires full radiative transfer modeling to take radiative pumping into account.

Based on the analysis of the full spectrum we estimate that the transitions presented in Fig. 11 are only marginally blended with fainter transitions from other species, with the exception of HCN $J = 2-1$ $v_2 = 1f$ and more importantly HNC $J = 4-3$ $v_2 = 1f$. Although not blended with other species, HCO$^+$ $J = 4-3$ $v = 2f$ falls between two bright features and we therefore consider this line to be tentatively detected. The other two HCO$^+$ $v = 2f$ transitions, $J = 3 - 2$ and $2 - 1$, are not detected as shown in Fig. 11.

5.2.1. High temperature driven “carbon-rich” chemistry

Our data show that the vibrational emission of HCO$^+$ is one order of magnitude fainter both relative to the observed

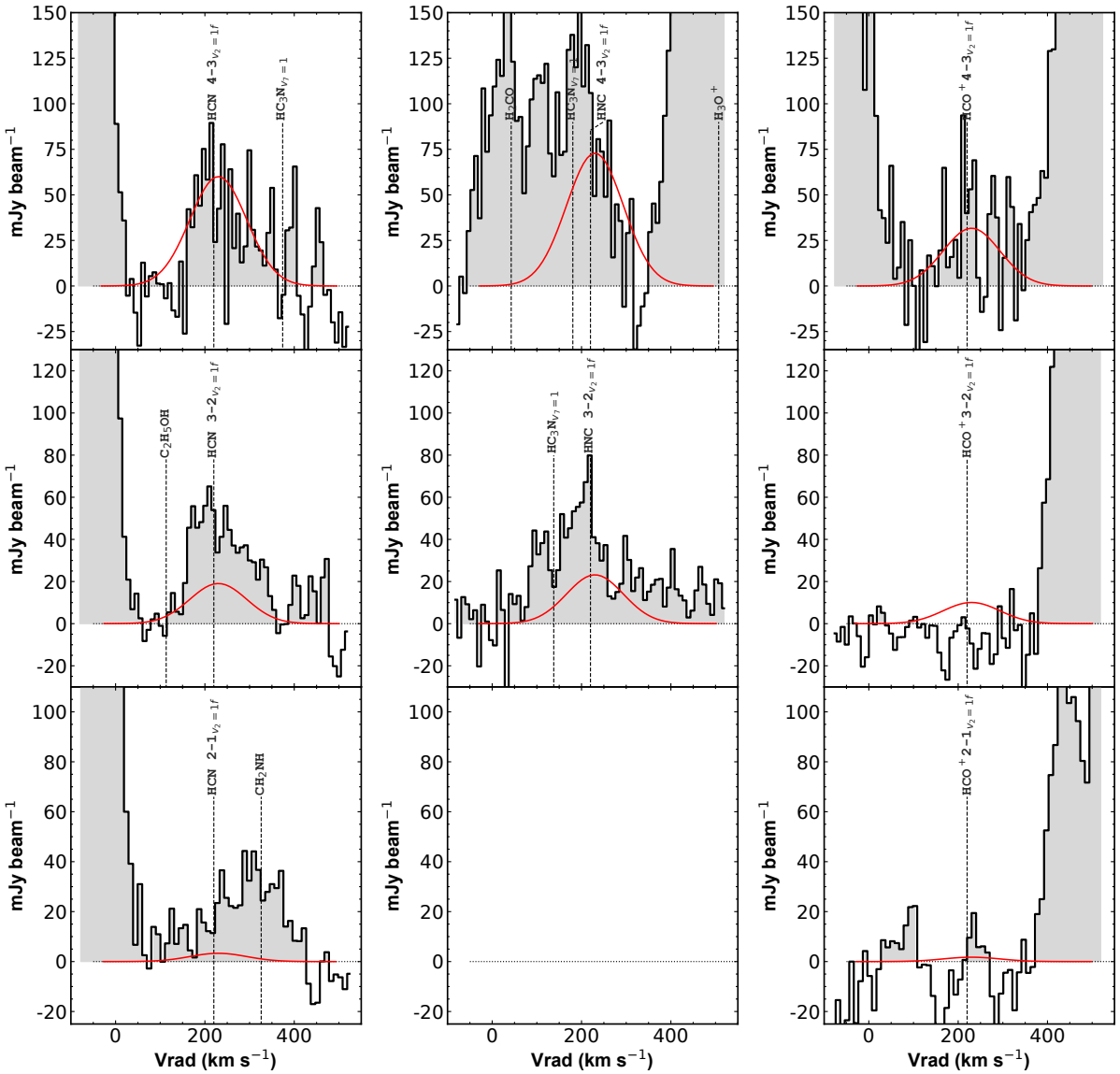

Fig. 11. Rotational transitions in the vibrational state $v_2 = 1f$ of HCN, HNC and HCO$^+$ covered within the surveyed frequency range. The box corresponding to HNC 2−1 $v_2 = 1f$ was left intentionally blank since its emission at 182.6 GHz falls within the telluric water transition observation gap (Sect. 2). Red lines show an attempt to fit the observed emission under LTE assuming $T_{ex} = 300$ K (see text in Sect. 5.2 for details). Nearby transitions from detected species with modeled flux densities >10% of that of the vibrational transitions are labeled.

emission of vibrational HCN and HNC as well as relative to the HCO$^+$ ground vibrational state (see Table 3). The detection of the $J = 4-3, v_2 = 1f$ transition alone might be considered tentative but still relatively faint compared to the corresponding transitions of HCN and HNC. However, if the same ratio among J transitions within the vibrational level of HCN and HNC would apply to HCO$^+$, we would then expect the 3 − 2 and 2 − 1 transitions to be significantly above the LTE fit in Fig. 11. Since this is not observed, we argue against the detection of vibrationally excited HCO$^+$.

The wavelengths of photons required to excite the vibrational states range from ∼22 µm for HNC to 12−14 µm for HCN and HCO$^+$ (Aalto et al. 2007; Sakamoto et al. 2010; Imanishi et al. 2017; González-Alfonso & Sakamoto 2019). High column densities and dust temperatures are required for the effective photon trapping leading the vibrational excitation of these molecules (González-Alfonso & Sakamoto 2019). However, the differences in the conditions for IR pumping of these species may explain the different relative intensities to their respective ground vibrational transitions (Sakamoto et al. 2010). For instance, the one order of magnitude larger HNC Einstein coefficient make it easier to pump than HCN (Aalto et al. 2007). However, these excitation differences alone do not explain the non detection of vibrational HCO$^+$ which has relatively similar excitation conditions to HCN.

Detections of vibrational transitions of HCN, HNC, HC$_3$N, and seemingly CH$_3$CN have been reported toward an ever increasing number of (U)LIRGs (see the compilation by Falstad et al. 2019) at the frequencies covered by ALCHEMI. However, beside the recent detections of vibrationally excited HCO$^+$ in absorption toward the gas-poor AGN in NGC 1052 (Kameno et al. 2020) and the faint emission feature (relative to the global galaxy emission) toward the molecular torus around the luminous AGN in NGC 1068 (Imanishi et al. 2020), no detections of HCO$^+$ in vibrational states have been reported in extragalactic environments.

Table 3. Spectral line emission properties of the vibrational transitions of HCN, HNC, and HCO^+.

Transition $v_2 = 1f$	Freq. (GHz)	$S_{\rm peak}$ (mJy)	$\int S\,\delta v$ (Jy km s^{-1})	$S_{v_2=0}$ (Jy)	$S_{v_2=0}/S_{v_2=1f}$	$L_{\rm vib}$ [(a)] ($L_\odot$)	$\frac{L_{\rm vib}}{L_{\rm IR}}$ [(b)] ($\times 10^{-9}$)
HCN 4 – 3	356.255	50 ± 10	8.0	6.70 ± 0.08	130 ± 30	36.3	1.7
HCN 3 – 2	267.199	53 ± 11	8.5	6.08 ± 0.07	120 ± 20	28.9	1.4
HCN 2 – 1	178.136	24 ± 10	3.8	3.64 ± 0.07	150 ± 60	8.5	0.4
HNC 4 – 3	365.147	68 ± 10	10.8	3.66 ± 0.04	53 ± 8	50.2	2.3
HNC 3 – 2	273.869	40 ± 5	6.4	3.64 ± 0.05	90 ± 10	22.3	1.0
HCO^+ 4 – 3	358.242	<38	<6.0	7.9 ± 0.1	>200	<27	<1.3
HCO^+ 3 – 2	268.689	<6.3	<0.95	6.77 ± 0.08	>1100	<3.2	<0.15
HCO^+ 2 – 1	179.129	<3.5	<1.6	3.58 ± 0.09	>1000	<3.6	<0.17

Notes. Results from Gaussian fitting individual transitions, not from the LTE model in Fig. 11, taking into account contamination from other species. Both the line fit and the upper limit calculations considers a line width of 150 km s^{-1}, similar to that fitted to most rotational transitions. [(a)]Luminosity estimates of the vibrational emission follow Eq. (3) in Solomon & Vanden Bout (2005). [(b)]Considering an infrared luminosity of NGC 253 is $L_{\rm IR} = 2.1 \times 10^{10}\,L_\odot$ from Strickland et al. (2004).

Similar to what is reported here toward NGC 253, an explicit nondetection of vibrational HCO^+ emission was reported toward the compact LIRG NGC 4418 and the ULIRG IRAS 20551-4250 (Sakamoto et al. 2010; Imanishi et al. 2017), while clearly detecting HCN and/or HNC vibrational emission. Imanishi et al. (2017) claimed an overabundance of HCN toward IRAS 20551-4250, following the statistically suggested higher rotational emission HCN/HCO^+ ratio in AGN dominated environments (Izumi et al. 2013; Privon et al. 2015; Imanishi et al. 2016). However, as suggested by Izumi et al. (2013) based on the chemical modeling of Harada et al. (2010) high temperature chemistry could be responsible for such a relative HCN overabundance.

At high temperature (Harada et al. 2010), a "carbon-rich" chemistry can be mimicked when oxygen is locked in the form of H_2O. In such conditions, carbon bearing species such as HCN and HNC may be boosted by 1–2 orders of magnitude, while HCO^+ would be reduced by a similar amount. This may actually be the scenario in hot dense gas around the protostars in starburst dominated environments. In these regions high temperatures and densities are required not only to drive the efficient infrared pumping of vibrational states ($T_{\rm d} > 100$ K, Aalto et al. 2015) but also to populate transitions such as those of HC_3N to $J = 40-39$, with critical density $n_{\rm crit} \sim 10^7$ cm^{-3} and lower level energy $E_l \sim 350$ K (Wernli et al. 2007). Within the ALCHEMI measurements, observed intensities above the LTE-derived fit to HC_3N indicate the presence of a high excitation temperature component.

The proposed scenario, in which high temperatures drive "carbon-rich" chemistry, would be supported by the nondetection of vibrationally excited oxygen-bearing species such as HCO^+, while the rotational transitions in the ground vibrational state, not originating in the denser infrared pumped region, may appear to be as bright as those of HCN and HNC. Similarly it would explain the relatively rich complex carbon chain chemistry detected in NGC 253 (Sect. 5.3), as well as the high abundances of HC_3N and HC_5N not only in NGC 253 (Aladro et al. 2015) but also in the prominent compact obscured nuclei (CON) in the ULIRG Arp 220 and the LIRG NGC 4418 (Martín et al. 2011; Costagliola et al. 2015), two well known emitters of vibrationally excited rotational lines. The locking of oxygen into H_2O would also explain the bright emission of H_2O and its weaker isotopologue $H_2^{18}O$ reported toward Arp 220 (Martín et al. 2011; König et al. 2017). Furthermore, the "carbon-rich" scenario might also be supported by bright HCN relative to CO emission reported toward the molecular outflow in Arp 220 (Barcos-Muñoz et al. 2018), where the oxygen depleted hot dense gas might have been blown away by the nuclear activity (due to either a starburst or active galactic nuclei).

5.2.2. Vibrational emission as tracer of global proto-SSC contribution

The ratios between the vibrational emission and the infrared luminosity for HCN, HNC, and HCO^+ are summarized in Table 3. The ratios measured with HCN $J = 3-2, v2 = 1f$ are about an order of magnitude below the $L_{\rm vib}/L_{\rm IR} = 10^{-8}$ threshold defining the extreme compact obscured nuclei, such as the above mentioned NGC 4418 and Arp 220 (Falstad et al. 2019).

We compare NGC 253 CMZ global average $L_{\rm vib}/L_{\rm IR} = 1.4 \times 10^{-8}$ derived from HCN $J = 3-2, v2 = 1f$ with that of 4.2×10^{-8} measured toward the Galactic Center hot core Sgr B2(N) at a spatial resolution of 0.1−1.2 pc (Rolffs et al. 2011). Assuming that vibrational emission is mostly contributed by Sgr B2(N)-like hot cores, this comparison results in a ∼3% level as a proxy to the contribution from proto-SSCs to the global infrared luminosity in NGC 253. In fact, this estimate is consistent with the contribution from proto-SSCs of ∼3% derived by Rico-Villas et al. (2020) based on high resolution imaging of vibrationally excited HC_3N toward NGC 253. We note that Rico-Villas et al. (2020) used a 25% lower IR luminosity from the CMZ of $1.6 \times 10^{10}\,L_\odot$, but still both results remain in good agreement.

Thus, we tentatively show that vibrational emission could be used as a 0th-order proxy to the proto-SSC contribution to the total infrared luminosity in extragalactic environments, under the assumption that there is marginal or no vibrational emission contribution by AGN heating as recently suggested from observations of the Seyfert galaxy NGC 1068 (Rico-Villas et al. 2021; Imanishi et al. 2020).

5.3. Organic molecules

As described in Sect. 4.4 some of the newly detected species in NGC 253 are organic molecules. In the following we briefly discuss the measured abundances of ethanol (C_2H_5OH) and formic acid (HCOOH). These species are selected as ancillary comparison data exists from Galactic Center molecular clouds to

provide an initial comparison of organic species abundances toward NGC 253; while we leave further more comprehensive discussions on organic molecules to upcoming publications using the higher resolution data. The detection of these organic species can only be unambiguously claimed thanks to the large spectral coverage which has allowed us to properly account for line blending and to cover multiple transitions from these large molecules.

Based on a sample of Galactic Center (GC) GMCs Requena-Torres et al. (2006) claimed an apparently homogeneous COM composition across the Galactic central molecular zone. In their study, the comparison between Galactic hot cores and GMCs showed that organic abundances relative to methanol, and in particular those of C_2H_5OH and HCOOH, agree within a factor of two, although the abundances toward hot cores were systematically found on the high end of the measurements (Fig. 12). The detection of these two species over CMZ scales toward NGC 253, allows us to include, for the first time, an extragalactic environment into this comparison. This allows us to explore the claimed grain composition homogeneity outside our Galaxy, and in this case toward a star-bursting environment.

Figure 12 places the abundances of C_2H_5OH ($1.1\pm0.4\times10^{-1}$) and HCOOH ($2.8 \pm 1.0 \times 10^{-2}$) relative to CH_3OH toward NGC 253 in the context of the Galactic Center GMCs observed by Requena-Torres et al. (2006) and the Galactic hot cores from Ikeda et al. (2001). Relative abundances with respect to methanol are commonly used to explore relative COM abundances while avoiding uncertainties associated with an estimate of H_2 column densities. In our analysis we have estimated the methanol abundance relative to H_2 from $C^{18}O$ and assuming $^{18}O/^{16}O = 100$ (as derived in Sect. 5.4.2) and $CO/H_2 \sim 8\times10^{-5}$ (Frerking et al. 1982), which yields $N_{H_2} = 3.1 \times 10^{23}$ cm^{-2}, in good agreement with previous single dish observations after correcting for the different assumed emission extent (Martín et al. 2009b). We included a conservative factor of two uncertainty in the H_2 determination to account for uncertainty in these assumptions. As expected, the relative abundance of CH_3OH in NGC 253 is significantly lower than in Galactic Center sources, since the clumpier methanol emission is referred to the global extended H_2 emission traced by CO over the large scales probed in our low resolution observations. Therefore the CH_3OH/H_2 in Fig. 12 can be actually considered a lower limit.

The comparison in Fig. 12 shows that the averaged abundances toward NGC 253 are on the high end of GMC measurements, similar to what is observed in the sample of hot cores. In particular the abundance of HCOOH is among the highest in the sample, but still a factor of three below the observed one in the Sgr B2(N) hot core (Requena-Torres et al. 2006).

Within the Galactic Center, emission from complex organic molecules is clearly detected toward hot molecular cores associated with massive star formation (e.g., Belloche et al. 2013, 2017, 2019). However, early surveys on a sample of GC GMCs (Requena-Torres et al. 2006, 2008; Martín et al. 2008a) and the recent reports of an ever increasing COMs richness in GC quiescent clouds (Zeng et al. 2018; Rivilla et al. 2019, 2020; Bizzocchi et al. 2020; Jiménez-Serra et al. 2020) are evidence of the widespread COM emission over GMC scales.

Previous single dish line surveys toward the CMZ of NGC 253 claimed that the observed average chemical abundances resemble that of GC GMCs (Martín et al. 2006; Aladro et al. 2011a). This chemistry would be mostly driven by the widespread large-scale shocks affecting its CMZ (García-Burillo et al. 2000; Martín 2009; Meier et al. 2015).

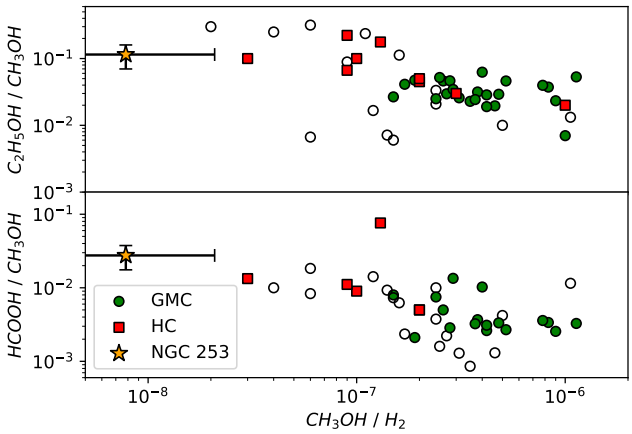

Fig. 12. Abundances of C_2H_5OH and HCOOH relative to CH_3OH toward the NGC 253 CMZ (orange star), compared to those measured toward Galactic hot cores (red squares; Ikeda et al. 2001) and Galactic Center giant molecular clouds (green circles; Requena-Torres et al. 2006). Upper limits to C_2H_5OH and HCOOH are represented by open symbols.

Indeed, these widespread shocks in NGC 253 would be the responsible for the global ejection of organic molecules from dust grains into the gas phase, similar to what is observed within the Galactic CMZ (Martin-Pintado et al. 1997; Martín et al. 2008b).

Our low resolution observations show how the emission from organic species described above, although consistent with that in GMCs, might imply a significant contribution from hot-core emission based on the observed abundances relative to methanol being closer to those found in GC hot cores. Such a hot core contribution should be significant since it is detectable in the averaged low resolution spectrum in this starbursting environment. The actual distribution and resolved abundances across the CMZ in NGC 253 will be better analyzed with the high resolution ALCHEMI data which will allow the comparison between the individual NGC 253 GMCs and the Galactic Center quiescent GMCs and hot cores.

5.4. Isotopic ratios

Investigating the elemental isotopic ratios and the difficulties to measure them with different molecular proxies in nearby galaxies is key to extend these studies to more distant objects, as well as probing the evolution of isotopic enrichment through cosmic time (Muller et al. 2006; Wallström et al. 2016; Kobayashi et al. 2020). A major advantage of the wide frequency coverage of the ALCHEMI survey is to allow for the measurement of isotopic ratios based on all the molecular isotopologue pairs detected within the covered bands, coupled with the relatively accurate column density measurement based on multiple transitions observed at the same angular resolution. The use of individual species and/or single transitions are subject to potential uncertainties in opacity (see Sect. 5.5), excitation, blending effects, as well as chemical fractionation.

Table 4 shows the isotopic ratios derived from the column densities fitted to all detected isotopologue pairs (Sect. 4.3.2). This table is graphically represented in Fig. 13 where the equivalent range of values measured in the Milky Way are also displayed for comparison. As explained in Sect. 4.3.2, a source size of 5″ was used for all species except for CO where a size of 10″ was required to match the observed absolute flux density of the

Table 4. Column density ratios in the CMZ of NGC 253 based on the ACA data.

Isotopes	Ratio [a]	Proxy
$^{12}C/^{13}C$	13.3 ± 1.4 [b]	$CO/^{13}CO$
	21.2 ± 1.5	$HCO^+/H^{13}CO^+$
	26.1 ± 1.3	$HCN/H^{13}CN$
	17.4 ± 1.1	$HNC/HN^{13}C$
	21 ± 2	$CN/^{13}CN$
	23 ± 2	$CS/^{13}CS$
	18 ± 4	$H_2CO/H_2^{13}CO$
	100 ± 10	$C^{18}O/^{13}C^{18}O$
	46 ± 18	$CCH/^{13}CCH$
	80 ± 20	$CCH/C^{13}CH$
	60 ± 40	$CH_3OH/^{13}CH_3OH$
	30 ± 40	$HC_3N/HC^{13}CCN$
	30 ± 40	$HC_3N/H^{13}CCCN$
	20 ± 30	$HC_3N/HCC^{13}CN$
	20 ± 7	$CH_3CCH/CH_3^{13}CCH$
	22 ± 3	$CH_3CCH/CH_3C^{13}CH$
	40 ± 20	$CH_3CCH/^{13}CH_3CCH$
$^{16}O/^{18}O$	48 ± 5 [b]	$CO/C^{18}O$
	520 ± 60	$^{13}CO/\ ^{13}C^{18}O$
	100 ± 20	$HCO^+/HC^{18}O^+$
$^{18}O/^{17}O$	8.7 ± 1.2	$C^{18}O/C^{17}O$
$^{16}O/^{17}O$	400 ± 40 [b]	$CO/C^{17}O$
	13 ± 4	$SiO/Si^{17}O$
$^{14}N/^{15}N$	147 ± 15	$HCN/HC^{15}N$
	220 ± 50	$HNC/H^{15}NC$
$^{32}S/^{34}S$	9.7 ± 0.5	$CS/C^{34}S$
	14 ± 4	$SO/^{34}SO$
$^{28}Si/^{29}Si$	9 ± 4	$SiO/^{29}SiO$
$^{28}Si/^{30}Si$	40 ± 20	$SiO/^{30}SiO$

Notes. [a]Isotopic ratios are based on the column density LTE fits which, though opacity corrected, is close to the optically thin regime. Higher opacity could result in ratios up to a factor of two larger (see Sect. 5.4 and Table 5). [b]This column density ratio has been re-calculated for a common source size of 10″ in order to match the size required to fit the main CO isotopologue emission (see Sect. 5.4)

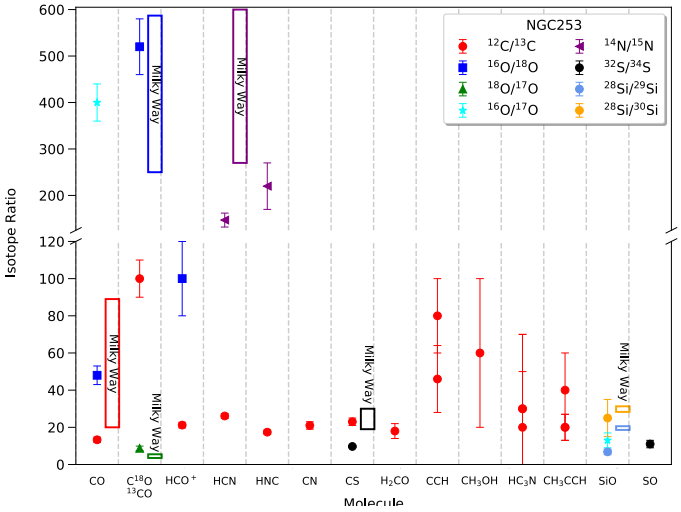

Fig. 13. Measured NGC 253 isotope ratios in the ACA data (Table 4) compared to their equivalent values in the Milky Way (Wilson 1999). The horizontal axis indicates the molecular species, or in the case of CO the isotopomer, used to measure a given isotope ratio. Colored rectangles are used to indicate Milky Way isotope ratio value ranges. As no uncertainties nor range of values was provided for the Si isotope ratios, a range of 10% of the estimated values was assumed. As the Milky Way $^{16}O/^{17}O$ value would be ≳875, we have opted to not show this Milky Way isotope ratio value.

CO transitions. In order to provide a meaningful ratio of CO isotopologues when referred to the main isotopologue, the emission of ^{13}CO and $C^{18}O$ fits were recalculated for an equivalent source size of 10″. In this way the ratio is meaningful, despite opacity considerations, since all the CO isotopologues present resolved structure in the low resolution maps (Fig. 7). We observe how the carbon and oxygen ratios derived with the main CO isotopologue are consistently a factor of 2−10 below those measured with any other isotopologue pairs in Table 4 (Sects. 5.4.1 and 5.4.2). This is evidence of the opacity affecting CO even in the averaged CMZ emission.

The values in Table 4 are optical depth corrected, under the assumptions of LTE and similar source extent. When it was possible to fit the excitation temperatures in the different isotopologues of a given species, we found a good agreement (Sect. 4.3.2). For the assumed source size of 5″ most of the main isotopologues show moderate optical depths (≲1), so column density ratios are close to the optically thin regime and therefore close to what would be derived from line intensity ratios. The advantage of using column density ratios is that we are considering the contribution from all transitions of a given molecule, rather than relying on a single transition.

In order to evaluate the effect of the assumed source size on the opacity of the main isotopologue and, consequently on the derived isotopic ratio, Table 5 shows the LTE fit results for various assumed source sizes, where HCO^+ is selected as case example. We note that for sizes <3″, increasing the excitation temperature T_{ex} is requierd to reproduce the observed absolute flux densities, which results in lower opacities, but it then becomes difficult to fit the emission with a single temperature component. Therefore, the ranges explored in Table 5 are a good representation of the effect of opacity on the derived isotopic ratio, which can become a factor of two larger than the optically thin approximation.

To put our results into context, Table 6 compiles all isotopic ratios reported in the literature toward NGC 253. The "nominal" isotopic ratios commonly used in the literature for local galaxies, as compiled in Wilson (1999), are $^{12}C/^{13}C = 40$, $^{16}O/^{18}O = 200$, and $^{18}O/^{17}O = 8$. However, these derived values are subject to the limitations of the species used as proxy as well as the uncertainty of the opacity in the brighter isotopologue (see Sect.5.5 for a discussion on opacity). Placing our NGC 253 observations into context of previous detections is key since these standard isotopic ratios are mostly based on measurements toward M 82, the other prototypical nearby starburst galaxy, and our target NGC 253 (see overview and discussions in Henkel et al. 2014; Martín et al. 2019b; Tang et al. 2019)

In the following we discuss individual atomic ratios which are probed by our molecular column density ratios and are globally averaged over the CMZ in NGC 253 at our ACA resolution.

5.4.1. Carbon

Observations within the center of our Galaxy show the dependency of the observed isotopic ratios on the molecular species used as proxy. Such variations are observed in $^{12}C/^{13}C$ using

Table 5. Effect of source size on the $^{12}C/^{13}C$ ratio derived from HCO^+.

Source size ($''$)	N(HCO^+) log(cm^{-2})	τ_{3-2}	N($H^{13}CO^+$) log(cm^{-2})	$^{12}C/^{13}C$
3	15.4(14.1)	3.6	13.9(12.3)	38.2(1.9)
4	15.1(13.2)	1.4	13.6(12.1)	27.2(0.8)
5	14.8(12.9)	0.8	13.4(12.2)	21.1(1.3)
10	14.1(12.2)	0.15	12.8(11.2)	19.2(0.6)
15	13.8(11.9)	0.044	12.5(10.9)	18.6(0.5)

Notes. Fit with only column density (N) as free parameter. All other parameters are fixed to those derived for source size 5$''$ to isolate the effect of source size parameter on derived column density and optical depth (see Sect. 5.4).

H_2CO, CO, and CN isotopologues (Gardner & Whiteoak 1982; Langer & Penzias 1990; Milam et al. 2005). In fact, recent chemical models predict different $^{12}C/^{13}C$ ratios for different molecular species depending on the density, on the chemical formation pathways, the temperature and on the cosmic-ray ionization rate (Colzi et al. 2020; Loison et al. 2020; Viti et al. 2020). Therefore, variations among species are expected as they can also trace different gas components.

Under the assumptions described in Sect. 5.4 and excluding the values derived from CO isotopologues (see below), our observations show column density derived $^{12}C/^{13}C$ ratios ranging from 17 to 60, with an error weighted average ~25 ± 10. The largest values are derived from the isotopologues with the faintest transitions, close to the noise level and more affected by the uncertainties due to blending to other species. Therefore, the uncertainties in the ratios may be significantly higher than the pure statistical uncertainty from the fit. Still, they are included in Table 4 for the sake of completeness. The weighted average taking into account only the ratios with the lowest uncertainties, that is the brighter species, namely HCO^+, HCN, HNC, CN, CS, and H_2CO, is 22 ± 2. This value is just marginally lower than the weighted average considering all species and in much narrower agreement among them as can be graphically seen in Fig. 13.

The low average ratio observed in the brighter species of 22 ± 2 is in good agreement to previous low resolution observations (see Table 6 and notes therein), which were used to derive the nominal extragalactic ratio of 40 based on opacity considerations. In fact, the only way to reconcile the average $^{12}C/^{13}C$ ratio with the literature value of $^{12}C/^{13}C$~ 40 is by assuming a smaller source size (see discussion in Sect. 5.4) where the emitting gas within this 850 × 340 pc region is actually confined to a region of $\lesssim$5$''$ ($\lesssim$85 pc). This would imply that all the brightest species showing ratios around ~20 in Table 4 would be affected by approximately the same optical depth. However, based on the opacity of the brightest transition of these species (Table 4), we do not expect the same opacity effect on all these species, and it would not be supported by the discussion of the opacity of sulfur species (Sect. 5.4.4).

We note that, $CN/^{13}CN$ observations by Tang et al. (2019) derived opacity corrected ratios ranging 30–67, and at a similar angular resolution a value of 21 was derived from $C^{18}O/^{13}C^{18}O$ by Martín et al. (2019b). This discrepancy cannot be explained by opacity effects (see Sect. 5.5), but rather by tracing a different molecular component. Despite the uncertainty on the fainter isotopologues, the ratios derived from CCH isotopologue pairs (Fig. 14) are consistent with the limit of >50 derived at single dish resolution based on the non detection of both $C^{13}CH$ and the ^{13}CCH by Martín et al. (2010).

Table 6. Integrated intensity isotopic ratios toward NGC 253 in the literature.

Isotopes	Ratio	Proxy	Beam	Reference
$^{12}C/^{13}C$	16 ± 3	$HCN/H^{13}CN$	26$''$	1
	10.7 ± 1.7	$HCO^+/H^{13}CO^+$	26$''$	1
	28 ± 6	$HNC/HN^{13}C$	26$''$	1
	14 ± 3 [(a)]	$CS/^{13}CS$	16$''$	1
	>40	$CN/^{13}CN$	22$''$	1
	>60	$C^{18}O/^{13}C^{18}O$	23$''$	2
	>56	$CCH/^{13}CCH$	14$''$	2
	>46	$CCH/C^{13}CH$	14$''$	2
	36 [(b)]	$CN/^{13}CN$	22$''$	3
	13.7 ± 0.5	$HCN/H^{13}CN$	24$''$	8
	14 ± 2	$HCO^+/H^{13}CO^+$	24$''$	8
	17 ± 1	$HNC/HN^{13}C$	27$''$	8
	34 ± 2	$CS/^{13}CS$	25$''$	8
	28 ± 2 [(c)]	$CN/^{13}CN$	24$''$	8
	10 – 20	$HCN/H^{13}CN$	2$''$	11
	10 – 20	$HCO^+/H^{13}CO^+$	2$''$	11
	21	$C^{18}O/^{13}C^{18}O$	3$''$	4
	19 – 53 [(d)]	$CN/^{13}CN$	2.5$''$	5
$^{16}O/^{18}O$	~150 [(e)]	$^{13}CO/C^{18}O$	12$''$	6
	>300 [(e)]	$^{13}CO/C^{18}O$	12	2
	130	$^{13}CO/^{13}C^{18}O$	3$''$	4
	69 ± 2	$HCO^+/HC^{18}O^+$	28$''$	8
$^{18}O/^{17}O$	10	$C^{18}O/C^{17}O$	16$''$	7
	~6.5	$C^{18}O/C^{17}O$	12$''$	6
	7.6 ± 0.5	$C^{18}O/C^{17}O$	23$''$	8
	4.5	$C^{18}O/C^{17}O$	3$''$	4
$^{16}O/^{17}O$	~300 – 500	CO	2$''$	11
$^{32}S/^{34}S$	16	$CS/C^{34}S$	24$''$	9
	8	$CS/C^{34}S$	16$''$	9
	8 [(e)]	$^{13}CS/C^{34}S$	16$''$	10
	>16 [(e)]	$^{13}CS/C^{34}S$	16$''$	2
	7.5 ± 0.3	$CS/C^{34}S$	24$''$	8

Notes. [(a)]With this line ratio, Henkel et al. (1993) (see their Sect. 5) estimated a column density ratio of >40 on opacity grounds, under the assumption that previously measured $CS/C^{34}S$~8 by Mauersberger & Henkel (1989) should actually be equal to the average Galactic and solar system sulfur ratio of 23. [(b)]Based on a hyperfine structure derived opacity estimate of 0.5 for the main J = 2–1 feature, which results in an opacity corrected ratio of 40. [(c)]Column density ratio estimated using a fit to the CN profiles with MADCUBA (Martín et al. 2019a). [(d)]When corrected by an average estimated opacity based on the CN hyperfine structure the authors derive a ratio ranging 30 – 67, with notable difference between that at the emission peak (30 – 40) and the galaxy outskirts (47 – 67). [(e)]Indirect measurement using the ^{13}C isotopologue and multiplying by an assumed $^{12}C/^{13}C$ ratio which differs among studies.

References. (1) Henkel et al. (1993, and references therein); (2) Martín et al. (2010); (3) Henkel et al. (2014); (4) Martín et al. (2019b); (5) Tang et al. (2019); (6) Harrison et al. (1999); (7) Sage et al. (1991); (8) Aladro et al. (2015); (9) Mauersberger & Henkel (1989); (10) Martín et al. (2006); (11) Meier et al. (2015).

The ratios estimated based on CO isotopologues appear to be significantly different than those from higher dipole moment species. As mentioned in Sect. 5.4, the lower value derived from $CO/^{13}CO$ is the result of a large opacity affecting the CO main isotopologue, so this value is not considered meaningful.

Now focusing on the rarer CO isotopologue pairs, our averaged $^{12}C/^{13}C$ ratio based on higher dipole moment species

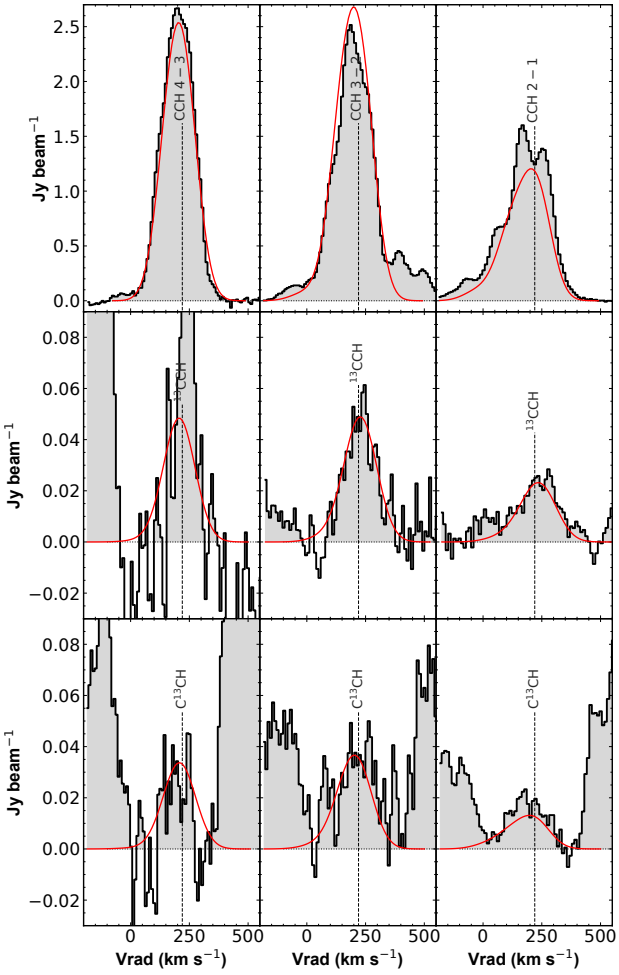

Fig. 14. Spectral features of the $J = 4-3$ (*left*), $3-2$ (*center*) and $2-1$ (*right*) transitions from three of the isotopologues of CCH detected in the survey. Red curves shows the LTE model best fits. Contributions by other species is almost negligible for most transitions according to the global LTE model from the full survey (see Sect. 4.3.2). However we note that the observed profile of ^{13}CCH $4-3$, not following the CCH LTE model and not accounted for by emission from other species, was not used in the fit.

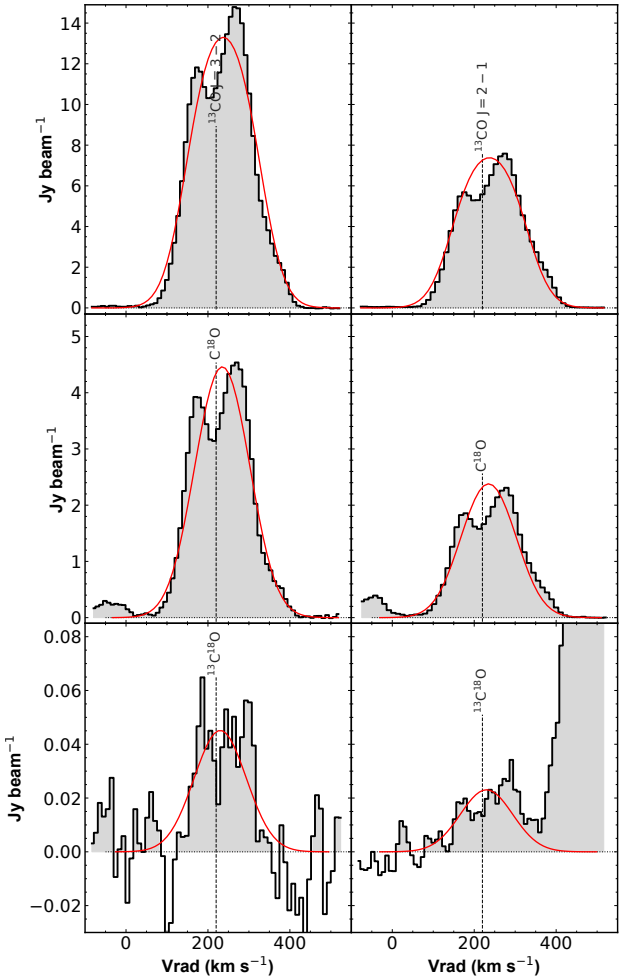

Fig. 15. Spectral features of the $J = 3-2$ (*left*) and $2-1$ (*right*) transitions from three of the rarer isotopologues of carbon monoxide detected in the survey. Red curves show the LTE model best fits. Contributions by other species are not shown since all features appear to be free of contamination.

agrees well with the value of ∼21 ± 6 derived at 3″ resolution using the $C^{18}O/^{13}C^{18}O$ column density ratio (Martín et al. 2019b). In their work, they concluded that there was no obvious signature of high optical depth in the measured 3 mm transitions of the rarer CO isotopologues. However, our measured $C^{18}O/^{13}C^{18}O$ ratio in the 15″ resolution data in this work is a factor of four above the ratio measured with other species and to that measured with the same isotopologue pair at 3″ resolution by Martín et al. (2019b). On the other hand this ratio agrees with the limit of >60 estimated from single dish observations at 23″ resolution (Martín et al. 2010). This high ratio is clearly apparent in the spectral features shown in Fig. 15. We note, for completeness, that both the single dish and high resolution measurements referred here use the $J = 1-0$ transitions. In principle this should not cause differences in the ratios if both transitions originate from the same regions and share similar excitation conditions. As pointed out by Martín et al. (2019b), the different ratios measured at high and low resolution might be evidence for the existence of two distinct components with different degrees of stellar nucleosynthesis ISM processing, similar to what is observed in the Galactic Center (Riquelme et al. 2010). As indicated by Viti et al. (2020), the difficulties to reproduce such a high value from chemical modeling is evidence of the large range of carbon isotopic ratios measured being the result of nucleosynthesis and not fractionation.

In this multicomponent scenario, the low resolution observations would be tracing extended unprocessed material with a $^{12}C/^{13}C$ ratio of ∼100, similar to what is observed in the outskirts of our Galaxy (Wouterloot & Brand 1996). This material must have recently been driven toward the nucleus from the outer regions by the stellar bar in NGC 253 (Sect. 1) and not yet enriched by ongoing star formation in the CMZ. On the other hand, the denser and more compact gas dominating the GMC emission would be enriched by the starburst event (e.g., Romano et al. 2017) resulting in $^{12}C/^{13}C$ ratios of ∼20−30 as traced by optically thicker high electric dipole moment molecules even at low resolution. The high resolution observations of the optically thinner CO transitions would also trace this processed molecular gas with $^{12}C/^{13}C$ ratio of ∼21 (Martín et al. 2019b).

Tracing the more extended, potentially less processed gas by CO isotopologues agrees with them being the only transitions showing extended emission at the ACA resolution (Fig. 7). Although selective photodissociation might play a more

important role in $^{13}C^{18}O$, this effect should also affect $C^{18}O$ and to a lesser extent ^{13}CO. We note that despite the uncertainty due to the noise, $^{13}C^{18}O$ line profiles match very well those of the more abundant CO isotopologues (Fig. 15).

5.4.2. Oxygen

The situation with oxygen ratios is consistent with that encountered with carbon ratio measurements. Our $^{16}O/^{18}O$ ratio of 100±20 measured with HCO^+ could be reconciled with the value in the literature of 200 if we account for a possible multiplicative factor of two due to opacity as discussed above. The value derived with the main CO isotopologue is half (48 ± 5) of that derived with HCO^+, once again due to the high opacity of CO (Sect. 5.4). However, that derived with the ^{13}C substitutions of CO results in a ratio of 520 ± 60 which, similar to the carbon isotopic ratio discussed above, is a factor of five above that measured with HCO^+, but still within the range of values observed within the Milky Way as displayed in Fig. 13. The $^{16}O/^{18}O$ ratio is in reasonable agreement with previous single dish measurements (69, Aladro et al. 2015) and in good agreement with the value measured at higher resolution with the ^{13}C substitutions of CO (130, Martín et al. 2019b) as shown in Table 6.

The scenario depicted by the oxygen ratios would be similar to that from carbon isotopic ratios with a low ^{18}O enriched material traced by the optically thin rarer CO isotopologues. Regarding ^{17}O, we find good agreement between our measured $^{18}O/^{17}O$~9 ratio and the range derived from single dish measurements (7 − 10). The $^{16}O/^{17}O$ ~ 400 derived with the main CO isotopologue, similar to the values derived toward individual GMCs by Meier et al. (2015), would translate into an actual value of ~800 based on the differences observed between CO derived ratios and those with other species above. Finally the low $^{16}O/^{17}O$ ~ 13 value deduced from SiO sheds doubts on the actual detection of $Si^{17}O$ unless its flux density is boosted due to non-LTE effects, in which case the ratio measured would not be indicative of the actual oxygen ratio. We therefore report its detection as tentative.

5.4.3. Nitrogen

Chemical modeling of nitrogen isotopic ratios has recently been published by Viti et al. (2019), where models are compared with existing measurements in the extragalactic ISM. Here we present the first ^{15}N isotopologue detection toward NGC 253 and we place it in the context of previous observations toward other galaxies and high-redshift molecular absorbers. The $^{14}N/^{15}N$ nitrogen isotopic ratio measured with both HCN (147 ± 15) and HNC (220 ± 50) are consistent with a weighted average of 170±20. This value is also in agreement with the $^{14}N/^{15}N$~152± 27 measured toward the molecular absorber PKS 1830-211 (Muller et al. 2011) and with the $^{14}N/^{15}N$~227 ± 41 of toward NGC 4945 (Henkel et al. 2018). In both objects, the HNC ratio is higher, but significantly more uncertain, than that measured with HCN.

The $H^{13}CN/HC^{15}N$ ratio of 5.6 ± 0.6 is close to that measured toward PKS 1830-211 (4.8 ± 0.2) and almost twice that of the other molecular absorber B 0218+357 of 3.0 ± 0.5 (Wallström et al. 2016). This ratio is 35% lower than that measured toward NGC 4945 at ~40 pc resolution (2″, Henkel et al. 2018), where they find a global value of ~8.5 ± 1.7, although values of 4 − 6 are measured outside the very nuclear region, in contrast with the value of 2.1 ± 0.3 at 60″ resolution toward the same object (Wang et al. 2004). On the other hand the ratio $HN^{13}C/H^{15}NC$ of 13 ± 3 is about twice that measured toward PKS 1830-211 of ~7 (Muller et al. 2011).

Similar to what is discussed with the other isotopic ratios, the effect of opacity could raise the $^{14}N/^{15}N$ ratio up to 400 if the opacity correction suggested in the carbon isotopic ratio discussion is considered. Based on the updated $^{14}N/^{15}N$ galactocentric trend by Colzi et al. (2018), a value of 400 would correspond to a 8 kpc galactocentric distance, while the 4 kpc molecular ring shows a ratio of ~300, which decreases 200 at ~1 kpc. The latter is consistent with the value derived here, uncorrected for putative high opacity.

We note that the non detected spectral features of both $N^{15}NH^+$ and $NN^{15}H^+$ down to our achieved noise level is in agreement with the derived $^{14}N/^{15}N$.

5.4.4. Sulfur

$^{32}S/^{34}S$ ratios measured with both CS and SO (9.7 ± 0.5 and 14 ± 4, respectively) are in good agreement with previous single-dish measurements based on CS observations of 8 ± 2 (Martín et al. 2005) and more than a factor of two above that derived from SO (5.1 ± 1.2 Martín et al. 2006). However, the latter is likely the result of uncertain de-blending from SO_2 emission on a very faint feature (see Appendix C.4 in Martín et al. 2006)

However, if the CS emission is actually optically thick, in order to reconcile the carbon isotopic ratios with the nominal extragalactic value of 40 (see Sect. 5.4), then the main CS and SO isotopologues should show the same peak optical depth. This way, the derived $^{32}S/^{34}S$ would be similar in both species. Based on the fit values in Table A.3, the opacity ratio between both species is measured to be $\tau_{C^{34}S/^{34}SO}$ ~ 15 which does not support the idea of CS being optically thick, unless both species are tracing very different sulfur isotopic ratio components.

Our sulfur isotopic ratio of $^{32}S/^{34}S$ ~ 10 is about half of the Galactic Center value of ~22 measured with $^{13}CS/C^{34}S$ (assuming a $^{12}C/^{13}C$) or ~17, directly obtained from $^{13}CS/^{13}C^{34}S$ (Frerking et al. 1980; Wilson & Rood 1994; Humire et al. 2020). However, taking into account the $^{32}S/^{34}S$ Galactocentric gradient reported by Yu et al. (2020), there is a good agreement with the trend value within the Galactic central kiloparsec.

Our measured $^{13}CS/C^{34}S$=0.42 ± 0.04 is in between the average value measured in Galactic disk sources and sources in the Galactic Center region (between 0.35 and 0.68 Frerking et al. 1980).

Although as discussed above we do not see evidence for opacity effects in the sulfur isotopologue ratios, both opacity uncorrected and corrected values would lie within the range of values observed in other extragalactic sources (see, e.g., Wallström et al. 2016).

5.4.5. Silicon

Here we derive the first silicon isotopic ratios measured in emission toward external galaxies through the observed ration between SiO and the rarer ^{29}SiO, ^{30}SiO, and $Si^{17}O$ substitutions.

The ratios presented in Table 4 yields $^{29}Si/^{30}Si$~4.2, which is more than a factor of two above the value of 1.5 within the Galaxy (Penzias 1981; Anders & Grevesse 1989; Lodders 2003), and the value of 1.9 measured toward PKS 1830-211 (Muller et al. 2013). The apparent overabundance of ^{29}Si might imply that this is not a primary nucleus but resulting from some stellar processing. However, observations of silicon iso-

topic ratios toward a wider variety of environments are required to further analyze the origin of silicon isotopologues, since there appears to be no difference between solar and Galactic Center observations (Wilson 1999).

On the other hand, the ratio $^{28}Si/^{29}Si = 9 \pm 2$ is however consistent with the ratio of 11 measured toward the molecular absorber PKS 1830-211 (Muller et al. 2011) and about a factor of two below the Solar system value of 19.6 (Anders & Grevesse 1989; Lodders 2003).

5.4.6. Isotopologue ratio overview

In this section we provide an overview of the results obtained from the different isotopologue ratios measured in this work, which are graphically summarized in Fig. 13.

Carbon, oxygen, nitrogen, and sulfur ratios measured with the brightest species other than CO, namely HCO^+, HCN, HNC, CN, CS, and H_2CO, are on the low end of the range measured in the Milky Way. In fact, the isotopologue ratios toward the NGC 253 CMZ are consistent with the values observed within the Galactic CMZ. These high dipole moment species may be tracing molecular gas enriched by the starburst present in the CMZ, which leads to an enrichment in the rarer isotologues, similar to what is derived from the Galactocentric trends observed in the Milky Way Galaxy (Wilson 1999; Milam et al. 2005; Yu et al. 2020). The emission from these less-abundant species appear unresolved in the 15″ resolution ACA data (Fig. 7).

Carbon and oxygen isotopic ratios measured with CO appear to have a dependency on the probed scales. The 3″ resolution ratios measured with the rarer CO isotopologues yielded reported ratios similar to those measured for the high dipole moment species in this work (Martín et al. 2019b). However, the ACA data discussed here, recovering larger scales, yields carbon and oxygen ratios consistent within the limits derived with single-dish observations (Martín et al. 2010), that is a factor of five larger than those measured at higher resolution. Carbon monoxide may be tracing a more extended molecular component not yet involved in and enriched by the star formation burst within the CMZ. Indeed, CO and its isotopologues are the only species showing extendend emission at the ACA resolution (Fig. 7). This dependence on the size scales measured highlights the importance of tracing the molecular emission at all scales, and in particular the importance of analyzing the ACA data which probes the largest molecular spatial scales.

Although opacity considerations may result in ratios which differ by up to a factor of ∼2 from the higher dipole moment species, in line with the ratios commonly found in the literature, this would imply that all species are affected by the same optical depth correction. Moreover, the high resolution study of CO isotopologues (Martín et al. 2019b), resulting in similar ratios to those from high dipole moment species as mentioned above, did not show evidences of optical depth effects except for potentially toward one of the brightest GMCs. Based on the analysis of CN emission in Sect. 5.5, it is likely that the emission from all species contains an optically thick component surrounded by an optically thin envelope within the individual GMCs.

Fractionation is considered to be negligible under the physical conditions in the bulk of the gas in galaxies (Romano et al. 2017). However, some species in our work might be showing some hints of fractionation. This appears to be the case for CCH (Table 4 and Fig. 14), where differences are found between the two ^{13}C isomers. The relationship of ratios is not consistent with what is observed in dark clouds where $CCH/^{13}CCH > CCH/C^{13}CH$ (Sakai et al. 2010). Our results also do not show evidence of the HC_3N isotopologue abundance differences that are measured in low-mass star forming regions (e.g., Araki et al. 2016). The uncertainty on the abundance ratios of isotopologue substitution of these more complex species have a relatively large uncertainty, which makes it also difficult to claim fractionation in CH_3CCH. Therefore we leave the discussion on the actual effect of fractionation in NGC 253 to a subsequent publication on the of individual GMCs within the NGC 253 CMZ measured at higher spatial resolution.

5.5. Opacity analysis with multitransition CN observations

One of the main sources of uncertainties in estimating column densities of the emitting molecules, or equivalently relative abundances, is the unknown effect of optical depth (Mangum & Shirley 2015; Martín et al. 2019a). Although the MADCUBA fit accounts for the effect of opacity (Sect. 4.3.2), the opacity (linearly related to the column density) and source size are partially degenerate (see discussion in Sect. 5.4). However, some molecular species present hyperfine structure transitions which are separated enough to constrain the opacity based on either the spectral feature profile or the ratio between the different groups of hyperfine spectral features. Such is the case of species like CN and CCH. In this section we analyze the hyperfine structure of multiple CN and CCH transitions, making use of the wide frequency coverage of the ALCHEMI data set. Through this analysis we highlight the importance of multitransition observations for an accurate opacity determination.

Previous studies, both at single dish resolution (Henkel et al. 2014) and ALMA high-resolution observations (Tang et al. 2019), made use of the CN $N = 1 - 0$ hyperfine split spectral line, consisting of two groups, the $J = \frac{3}{2} - \frac{1}{2}$ and the $J = \frac{1}{2} - \frac{1}{2}$ to estimate the optical depth of this transition. Within the frequency coverage of the ACA data presented in this article, we observe the $N = 3 - 2$ and $N = 2 - 1$, each consisting of three groups of hyperfine transitions as shown in Fig. 16. The brighter transitions of these groups, for reference, emit at 340.248 and 226.874 GHz, respectively. Here we present the analysis of these profiles using three simple LTE models (Fig. 16) to explain their observed emission and to estimate the optical depth affecting these lines.

Figure 16 (left panels) shows how the single component optically thin fit used in this work (for a source size of 5″) cannot reproduce the intensity of the fainter hyperfine groups, namely the $J = \frac{5}{2} - \frac{5}{2}$ and $J = \frac{3}{2} - \frac{3}{2}$ for the $N = J = 3 - 2$ and $N = 2 - 1$ groups, respectively. On the other hand, the two brighter hyperfine groups would have appeared to fit well to the optically thin regime if not considering the third group of transitions.

As a second approach (Fig. 16 center panels), we assumed a smaller (2.5″) and therefore thicker emission which accounts better for the fainter hyperfine groups. However, it does not manage to properly reproduce the emission from the two brighter groups. The three $N = 3 - 2$ line component groups could be considered reasonably fit within the model uncertainties if we would only be observing at this frequency. However, it clearly underestimates the emission of the brighter $N = 2 - 1$ group.

Finally, the right panels in Fig. 16 show a third simple model that considers two components. The model consists of one optically thin component with a 5″ source size, together with a much smaller (1.5″) optically thick component. The model fits well all three hyperfine groups in both CN transitions. In this model, the second component, ∼10× larger in mass and accounting for just ∼25% of the integrated line emission, would consist of a comb of saturated line profiles for the brighter hyperfine groups. Since

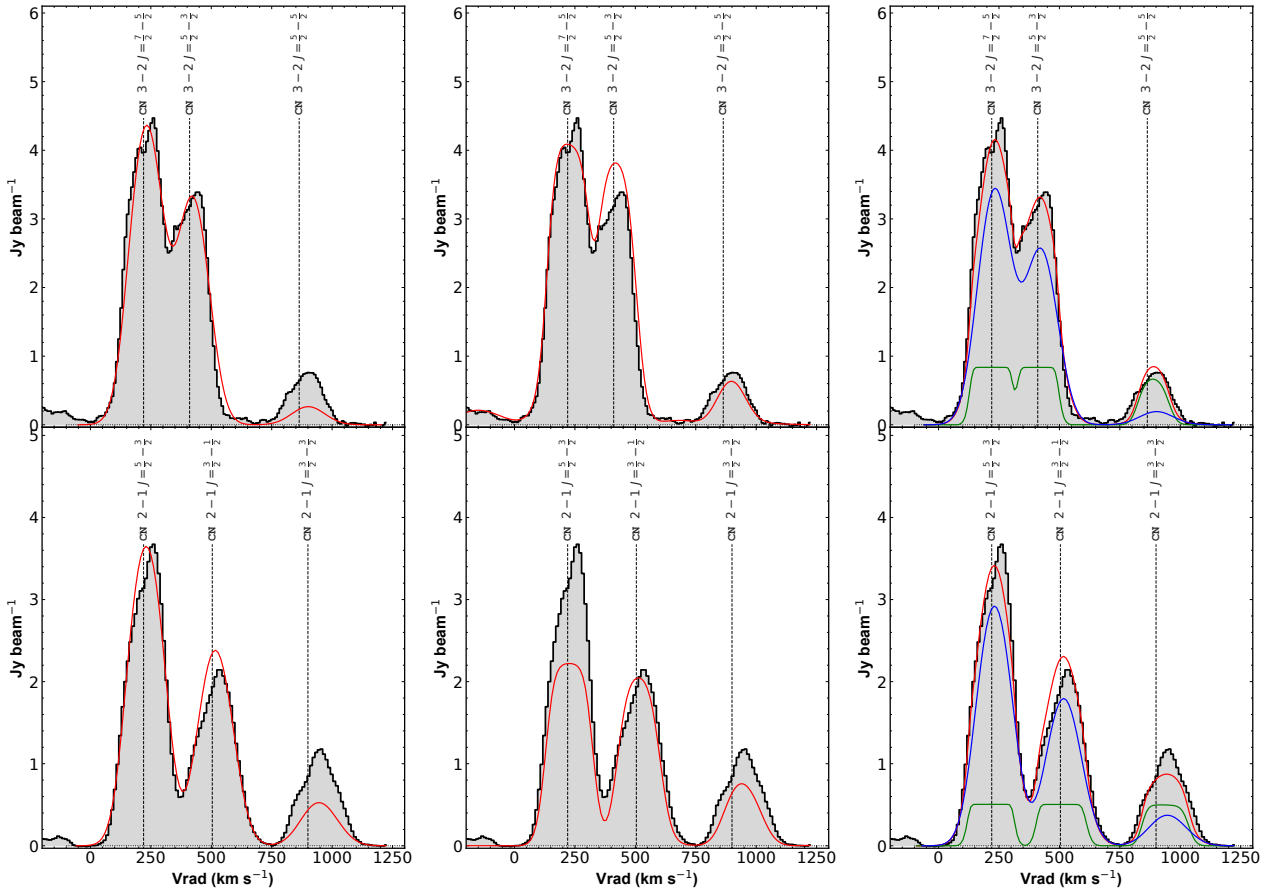

Fig. 16. CN $N = 3-2$ (*top*) and $N = 2-1$ (*bottom*) emission measured with the ACA data presented in this article. Panels are centered at 340.248 and 226.874 GHz, which is the frequency of the stronger emission hyperfine transition. The data are fitted with three simple models. *Left*: single component corresponding to the fit presented in Sect. 4.3.2, where a source size $\theta_s = 5''$ is assumed. The central opacity of the brightest transitions are $\tau_{3-2} = 0.25$ and $\tau_{2-1} = 0.44$, while the cumulative opacity of the stronger hyperfine groups are $\tau^g_{3-2} = 0.6$ and $\tau^g_{2-1} = 1.0$. See text in Sect. 5.5 for details. *Center*: single component fit assuming a smaller source size of $\theta_s = 2.5''$. Physical parameters of the fit are $\log(N) = 16.43$ cm^{-2}, $T = 13.4$ K, $v_{\rm lsr} = 229$ km s^{-1}, $\delta\, v_{1/2} = 118$ km s^{-1}. Opacity of brighter transitions are $\tau_{3-2} = 1.6$ and $\tau_{2-1} = 2.1$, and group opacities $\tau^g_{3-2} = 3.8$ and $\tau^g_{2-1} = 4.7$. *Right*: two component model assuming two sources of sizes $\theta_s = 5''/1.5''$. Physical parameters of models are $\log(N) = 15.6/17.3$ cm^{-2}, $T = 10.2/10.0$ K, $v_{\rm lsr} = 232/220$ km s^{-1}, $\delta\, v_{1/2} = 150/76$ km s^{-1}. Opacity of brighter transitions are $\tau_{3-2} = 0.18$ and $\tau_{2-1} = 0.31$ for the first component, while the thick component is completely saturated. Blue and green lines represent the two components, respectively, with sum of both models is represented by the red line.

the emission is saturated, the fit is degenerate and therefore the mass contained in this component (column density) is subject to a large uncertainty.

This exercise shows that, as we know from high resolution observations (Tang et al. 2019) the integrated emission of NGC 253 is a convolution of molecular components with different degrees of obscuration. Indeed, our unresolved observations point to the presence of a heavily obscured compact emitting region, very likely associated with the GMC dense cores in the NGC 253 CMZ (Sakamoto et al. 2011; Leroy et al. 2015; Rico-Villas et al. 2020) which might contain a large fraction of the mass, surrounded by a thinner likely more widespread component.

In the following we analyze the effect of such differences in size and opacities on the 3 mm transition used in the literature. By extrapolating the first two models above (left and center in Fig. 16) to the band 3 $N = 1-0$ hyperfine groups used in the literature, we obtain integrated flux density ratios between the $J = \frac{3}{2} - \frac{1}{2}$ and $J = \frac{1}{2} - \frac{1}{2}$ hyperfine groups of 1.95 ($\theta = 5''$ optically thin model) and 1.8 ($\theta = 2.5''$ optically thick model). Thus, the two models differ only by 8% in observed integrated intensity ratio of the $N = 1-0$ hyperfine groups. Therefore, this transition is less sensitive to optical depth effects than the combination of the two transitions consisting of three hyperfine groups observed in the ALCHEMI survey.

On the other hand CCH does not show evidence of the existence of such an optically thick component. However, the CCH hyperfine structure is not as well separated as in CN, and only the $2-1$ and $3-2$ groups at 174.7 and 262.0 GHz show an asymmetric profile at lower velocity due to this hyperfine structure. Unfortunately the large line width at this coarse spatial resolution together with the blending with other species, does not allow us to perform an analysis on CCH as detailed as on CN with the ACA data.

6. Summary and conclusions

The central molecular zone of the starburst galaxy NGC 253 is a complicated but interesting multicomponent system with various heating mechanisms playing a role at different scales. Previous low-resolution single-dish observations of NGC 253 showed that the averaged molecular abundances toward its CMZ resembles that of Galactic GMCs, and its observable chemistry

would be mostly driven by low-velocity cloud-cloud collisions (García-Burillo et al. 2000; Martín et al. 2006).

The ALCHEMI spectral survey of NGC 253 brings new insights into the chemical composition and physical conditions of the CMZ of NGC 253. In this article we present the ALCHEMI survey covering the spectral range from 84.2 to 372 GHz. Our large frequency coverage allows us to accurately align the flux scale of the individual tunings, where we observed significant deviations. Here we present the analysis of a subset of the ALCHEMI survey, consisting of the ACA observations covering the 256.7 GHz wide frequency band (i.e., full ALMA Bands 4 to 7) between 125.2 and 373.2 GHz down to a sensitivity of 0.27 to 1.0 mK. Even at the moderate resolution of the ACA observations (15″ ∼ 255 pc) we observe a rich molecular complexity. Here we summarize the main conclusions from our analysis of the ALCHEMI ACA data.

Continuum emission in the Rayleigh-Jeans tail can be modeled with a 42 K dust emission temperature with emissivity $\beta = 1.9$ plus a free-free component with SFR = 2.5 $M_\odot$ yr^{-1}. This SFR is an upper limit since we cannot determine the contribution due to synchrotron emission with the frequencies analyzed in this work.

The line contribution to the observed continuum emission varies across the bands between 5 and 36% when splitting the survey into five 50 GHz frequency bins. Continuum flux emission in high-z sources with a potentially significant starburst contribution might need to be corrected in certain frequency ranges according to our findings.

Spectral line identification was performed through LTE modeling per molecule, and not per spectral feature. 78 molecular species, including isotopologues and vibrational states are detected. Additionally, multiple emission features from radio recombination lines, namely H$n\alpha$, H$n\beta$ and He$n\alpha$, are identified throughout the survey.

Newly detected species in the extragalactic ISM include complex organic species and isotopologues, namely $H_2^{13}CO$, ethanol (C_2H_5OH), ^{13}CCH, $C^{13}CH$, HOCN, the three ^{13}C isotopologues of CH_3CCH, propynal (HC_3HO), and tentatively $Si^{17}O$.

The ALCHEMI survey also provides a useful template for observations of high-redshift galaxies that can be used to estimate the number of individual molecular species that are potentially detectable in a starburst environment as a function of the depth of the observations. Our estimate is based on the stacked spectrum from 22 high-z sources at $z = 2.0-5.7$ by Spilker et al. (2014) yields 3–4 expected species detections, in agreement with their reported identification.

Emission from infrared-pumped vibrational states of HCN, HNC, and HC_3N is detected for the first time in low resolution observations. However we do not detect vibrational emission of HCO^+, similar to what is reported toward the ULIRG IRAS 20551-4250 (Imanishi et al. 2017). We postulate the existence of a "carbon-rich" chemistry as result of oxygen depletion into H_2O according to high-temperature chemistry models (Harada et al. 2010). This explains both the rich carbon chemistry observed as well as the apparent lack of emission from vibrationally excited HCO^+. This would be similar to what is observed in local ULIRGs, where high abundances of carbon chains (HC_3N and HC_5N Martín et al. 2011; Costagliola et al. 2015; Aladro et al. 2015) and water (Martín et al. 2011; König et al. 2017) are reported, as well as HCN rich outflows (Barcos-Muñoz et al. 2018).

The global averaged $L_{\rm vib}/L_{\rm IR}$ ratio that we measure of 1.4×10^{-9} (from HCN 3 − 2) in NGC 253 is an order of magnitude below what is observed in compact obscured nuclei (Falstad et al. 2019). We propose that this ratio is a good proxy of the proto-stellar cluster contribution to the infrared luminosity. Based on this ratio we estimate the vibrational emission originating in Sgr B2(N) like hot cores would contribute 3% to the total infrared luminosity of NGC 253, in agreement with previous estimates by Rico-Villas et al. (2020).

Organic molecules, in particular C_2H_5OH and HCOOH, show relative abundances consistent with those found in Galactic Center GMCs, but on the high end, similar to those measured in Galactic hot cores. Although complex organic molecules are observed to be widespread within the Galactic Center, the global abundances in the central starburst environment in NGC 253 may be significantly contributed by hot core chemistry.

We report the measurement of isotopic ratios of carbon, oxygen, nitrogen, sulfur, silicon with all the isotopologue pairs detected in our survey. $^{14}N/^{15}N = 170 \pm 20$ is measured for the first time in NGC 253. $^{28}Si/^{29}Si = 9 \pm 2$ and $^{29}Si/^{30}Si = 4.2$ are measured for the first time in emission in the extragalactic ISM. Based on the analysis of all these ratios, we do not find evidence for opacity effects globally affecting the derived isotopic ratios.

High dipole moment species, namely HCO^+, HCN, HNC, CN, CS, and H_2CO, show consistent isotopic ratios of $^{12}C/^{13}C = 24 \pm 8$ and $^{16}O/^{18}O = 100 \pm 20$ which is half the standard extragalactic values (Wilson 1999) and consistent with the ratios observed within the central kiloparsec of our Galaxy. Nitrogen and sulfur isotopic ratios of $^{14}N/^{15}N = 170 \pm 20$ and $^{32}S/^{34}S \sim 10$ are also consistent with those in the Galactic CMZ.

Carbon and oxygen isotopic ratios derived from the rarer CO isotopologues result in values a factor of five larger than those measured with high dipole moment species and with the same CO isotopologues observed at higher spatial resolution. This result appears to confirm the multicomponent scenario where CO would be tracing the widespread gas recently funneled toward the CMZ from the galactic outskirts and therefore not yet processed by the prominent nuclear star formation. In this scenario higher dipole moment species would trace more compact dense gas clumps in the GMCs already enriched in secondary isotopologues.

Multitransition analysis of the hyperfine structure of CN reveals the presence of a likely saturated molecular component which could account for a significant fraction of the molecular mass and which is likely associated with the optically thick cores of GMCs.

The forthcoming series of papers based on the high resolution ALCHEMI data set will further investigate each of the topics presented in this paper to peer into the physical conditions that drive the observed averaged molecular abundances. The results in this article are therefore a reference for low linear resolution molecular observations of distant extragalactic sources and for follow-up studies of NGC 253 with higher angular resolution.

Acknowledgements. The authors want to specially thank David Fernández from the JAO ALMA Education and Public Outreach department for his contribution in creating the visuals presented in Fig. 1. This paper makes use of the following ALMA data: ADS/JAO.ALMA#2017.1.00161.L and ADS/JAO.ALMA#2018.1.00162.S. ALMA is a partnership of ESO (representing its member states), NSF (USA) and NINS (Japan), together with NRC (Canada), MOST and ASIAA (Taiwan), and KASI (Republic of Korea), in cooperation with the Republic of Chile. The Joint ALMA Observatory is operated by ESO, AUI/NRAO and NAOJ. The National Radio Astronomy Observatory is a facility of the National Science Foundation operated under cooperative agreement by Associated Universities Inc. N.H. is supported by JSPS KAKENHI Grant Number JP21K03634. K.S. is supported by MOST grants 108-2112-M-001-015 and 109-2112-M-001-020. L. C. acknowledges financial support from

the Spanish State Research Agency (AEI) through the project No. ESP2017-86582-C4-1-R. L.C. and V.M.R. acknowledge support from the Comunidad de Madrid through the Atracción de Talento Investigador Senior Grant (COOL: Cosmic Origins Of Life; 2019-T1/TIC-15379). G.A.F acknowledges financial support from the State Agency for Research of the Spanish MCIU through the AYA2017-84390-C2-1-R grant (co-funded by FEDER) and through the "Center of Excellence Severo Ochoa" award for the Instituto de Astrofísica de Andalucia (SEV-2017-0709). L.H. and M.P. are grateful for funding from the INAF PRIN-SKA 2017 program 1.05.01.88.04. K.K. acknowledges the support from the JSPS KAKENHI Grant Number JP17H06130. K.K. and Y. N. are supported by the NAOJ ALMA Scientific Research Grant Number 2017-06B.

References

Aalto, S., Spaans, M., Wiedner, M. C., & Hüttemeister, S. 2007, A&A, 464, 193
Aalto, S., Martín, S., Costagliola, F., et al. 2015, A&A, 584, A42
Aladro, R., Martín, S., Martín-Pintado, J., et al. 2011a, A&A, 535, A84
Aladro, R., Martín-Pintado, J., Martín, S., Mauersberger, R., & Bayet, E. 2011b, A&A, 525, A89
Aladro, R., Viti, S., Bayet, E., et al. 2013, A&A, 549, A39
Aladro, R., Martín, S., Riquelme, D., et al. 2015, A&A, 579, A101
Anders, E., & Grevesse, N. 1989, Geochim. Cosmochim. Acta, 53, 197
Ando, R., Nakanishi, K., Kohno, K., et al. 2017, ApJ, 849, 81
Araki, M., Takano, S., Sakai, N., et al. 2016, ApJ, 833, 291
Astropy Collaboration (Robitaille, T. P., et al.) 2013, A&A, 558, A33
Astropy Collaboration (Price-Whelan, A. M., et al.) 2018, AJ, 156, 123
Barcos-Muñoz, L., Aalto, S., Thompson, T. A., et al. 2018, ApJ, 853, L28
Bauer, M., Pietsch, W., Trinchieri, G., et al. 2008, A&A, 489, 1029
Belloche, A., Müller, H. S. P., Menten, K. M., Schilke, P., & Comito, C. 2013, A&A, 559, A47
Belloche, A., Meshcheryakov, A. A., Garrod, R. T., et al. 2017, A&A, 601, A49
Belloche, A., Garrod, R. T., Müller, H. S. P., et al. 2019, A&A, 628, A10
Bendo, G. J., Beswick, R. J., D'Cruze, M. J., et al. 2015, MNRAS, 450, L80
Bernard-Salas, J., Peeters, E., Sloan, G. C., et al. 2006, ApJ, 652, L29
Bizzocchi, L., Prudenzano, D., Rivilla, V. M., et al. 2020, A&A, 640, A98
Bøgelund, E. G., McGuire, B. A., Hogerheijde, M. R., van Dishoeck, E. F., & Ligterink, N. F. W. 2019, A&A, 624, A82
Bolatto, A. D., Warren, S. R., Leroy, A. K., et al. 2013, Nature, 499, 450
Butler, B. 2012, ALMA MEMO #594
Canzian, B., Mundy, L. G., & Scoville, N. Z. 1988, ApJ, 333, 157
Cao, Y., Qiu, K., Zhang, Q., et al. 2019, ApJS, 241, 1
Chin, Y., Henkel, C., Millar, T. J., Whiteoak, J. B., & Mauersberger, R. 1996, A&A, 312, L33
Chin, Y., Henkel, C., Langer, N., & Mauersberger, R. 1999, ApJ, 512, L143
Churchwell, E., Witzel, A., Huchtmeier, W., et al. 1977, A&A, 54, 969
Colzi, L., Fontani, F., Rivilla, V. M., et al. 2018, MNRAS, 478, 3693
Colzi, L., Sipilä, O., Roueff, E., Caselli, P., & Fontani, F. 2020, A&A, 640, A51
Combes, F., & Wiklind, T. 1998, A&A, 334, L81
Combes, F., Gottesman, S. T., & Weliachew, L. 1977, A&A, 59, 181
Costagliola, F., Aalto, S., Rodriguez, M. I., et al. 2011, A&A, 528, A30
Costagliola, F., Sakamoto, K., Muller, S., et al. 2015, A&A, 582, A91
Dahlem, M., Weaver, K. A., & Heckman, T. M. 1998, ApJS, 118, 401
Dale, D. A., Cohen, S. A., Johnson, L. C., et al. 2009, ApJ, 703, 517
de Kleer, K., Butler, B., de Pater, I., et al. 2021, Planet. Sci. J., 2, 5
de Vaucouleurs, G., de Vaucouleurs, A., Corwin, Jr., H. G., et al. 1991, in Third Reference Catalogue of Bright Galaxies
de Vicente, P., Martín-Pintado, J., Neri, R., & Colom, P. 2000, A&A, 361, 1058
De Zotti, G., Bonato, M., & Cai, Z. Y. 2019, in 3rd Cosmology School, Introduction to Cosmology, eds. K. Bajan, M. Biernacka, & A. Pollo, 9, 125
Endres, C. P., Schlemmer, S., Schilke, P., Stutzki, J., & Müller, H. S. P. 2016, J. Mol. Spectrosc., 327, 95
Falgarone, E., Zwaan, M. A., Godard, B., et al. 2017, Nature, 548, 430
Falstad, N., Hallqvist, F., Aalto, S., et al. 2019, A&A, 623, A29
Fernández-Ontiveros, J. A., Prieto, M. A., & Acosta-Pulido, J. A. 2009, MNRAS, 392, L16
Forbes, D. A., & Depoy, D. L. 1992, A&A, 259, 97
Francis, L., Johnstone, D., Herczeg, G., Hunter, T. R., & Harsono, D. 2020, AJ, 160, 270
Frerking, M. A., Wilson, R. W., Linke, R. A., & Wannier, P. G. 1980, ApJ, 240, 65
Frerking, M. A., Langer, W. D., & Wilson, R. W. 1982, ApJ, 262, 590
Friedel, D. N., Kemball, A., & Fields, B. D. 2011, ApJ, 738, 37
Fuente, A., Black, J. H., Martín-Pintado, J., et al. 2000, ApJ, 545, L113
García-Burillo, S., Martín-Pintado, J., Fuente, A., & Neri, R. 2000, A&A, 355, 499
García-Hernández, D. A., Manchado, A., García-Lario, P., et al. 2010, ApJ, 724, L39
Gardner, F. F., & Whiteoak, J. B. 1974, Nature, 247, 526
Gardner, F. F., & Whiteoak, J. B. 1982, MNRAS, 199, 23P
Geballe, T. R., Goto, M., Usuda, T., Oka, T., & McCall, B. J. 2006, ApJ, 644, 907
Ginsburg, A., Sipőcz, B. M., Brasseur, C. E., et al. 2019, AJ, 157, 98
González-Alfonso, E., & Sakamoto, K. 2019, ApJ, 882, 153
González-Alfonso, E., Smith, H. A., Fischer, J., & Cernicharo, J. 2004, ApJ, 613, 247
Guzmán, A. E., Verdugo, C., Nagai, H., et al. 2019, PASP, 131
Harada, N., Herbst, E., & Wakelam, V. 2010, ApJ, 721, 1570
Harada, N., Sakamoto, K., Martín, S., et al. 2018, ApJ, 855, 49
Harada, N., Sakamoto, K., Martín, S., et al. 2019, ApJ, 884, 100
Harrison, A., Henkel, C., & Russell, A. 1999, MNRAS, 303, 157
Heikkilä, A., Johansson, L. E. B., & Olofsson, H. 1999, A&A, 344, 817
Henkel, C., & Bally, J. 1985, A&A, 150, L25
Henkel, C., Jacq, T., Mauersberger, R., Menten, K. M., & Steppe, H. 1987, A&A, 188, L1
Henkel, C., Schilke, P., & Mauersberger, R. 1988, A&A, 201, L23
Henkel, C., Mauersberger, R., Wiklind, T., et al. 1993, A&A, 268, L17
Henkel, C., Asiri, H., Ao, Y., et al. 2014, A&A, 565, A3
Henkel, C., Mühle, S., Bendo, G., et al. 2018, A&A, 615, A155
Herbst, E., & van Dishoeck, E. F. 2009, ARA&A, 47, 427
Humire, P. K., Thiel, V., Henkel, C., et al. 2020, A&A, 642, A222
Ikeda, M., Ohishi, M., Nummelin, A., et al. 2001, ApJ, 560, 792
Imanishi, M., Nakanishi, K., & Izumi, T. 2016, ApJ, 825, 44
Imanishi, M., Nakanishi, K., & Izumi, T. 2017, ApJ, 849, 29
Imanishi, M., Nguyen, D. D., Wada, K., et al. 2020, ApJ, 902, 99
Iodice, E., Arnaboldi, M., Rejkuba, M., et al. 2014, A&A, 567, A86
Izumi, T., Kohno, K., Martín, S., et al. 2013, PASJ, 65, 100
Jiménez-Serra, I., Martín-Pintado, J., Rivilla, V. M., et al. 2020, Astrobiology, 20, 1048
Johansson, L. E. B. 1991, in Dynamics of Galaxies and Their Molecular Cloud Distributions, eds. F. Combes, & F. Casoli, IAU Symp., 146, 1
Kamenetzky, J., Glenn, J., Maloney, P. R., et al. 2011, ApJ, 731, 83
Kameno, S., Sawada-Satoh, S., Impellizzeri, C. M. V., et al. 2020, ApJ, 895, 73
Kepley, A. A., Chomiuk, L., Johnson, K. E., et al. 2011, ApJ, 739, L24
Kobayashi, C., Karakas, A. I., & Lugaro, M. 2020, ApJ, 900, 179
König, S., Martín, S., Muller, S., et al. 2017, A&A, 602, A42
Krieger, N., Bolatto, A. D., Walter, F., et al. 2019, ApJ, 881, 43
Krieger, N., Bolatto, A. D., Leroy, A. K., et al. 2020, ApJ, 897, 176
Langer, W. D., & Penzias, A. A. 1990, ApJ, 357, 477
Lehmer, B. D., Wik, D. R., Hornschemeier, A. E., et al. 2013, ApJ, 771, 134
Lenc, E., & Tingay, S. J. 2006, AJ, 132, 1333
Leroy, A. K., Bolatto, A. D., Ostriker, E. C., et al. 2015, ApJ, 801, 25
Leroy, A. K., Bolatto, A. D., Ostriker, E. C., et al. 2018, ApJ, 869, 126
Levy, R. C., Bolatto, A. D., Leroy, A. K., et al. 2021, ApJ, 912, 4
Li, F., Wang, J., Kong, M., & Li, S. 2019, MNRAS, 482, 4763
Lodders, K. 2003, ApJ, 591, 1220
Loison, J.-C., Wakelam, V., Gratier, P., & Hickson, K. M. 2020, MNRAS, 498, 4663
Magain, P., & Gillet, D. 1987, A&A, 184, L5+
Mangum, J. G., & Shirley, Y. L. 2015, PASP, 127, 266
Mangum, J. G., Ginsburg, A. G., Henkel, C., et al. 2019, ApJ, 871, 170
Martín, S. 2009, ASP Conf. Ser., 420, 19
Martín, S. 2011, IAU Symp., 280, 351
Martin, R. N., & Ho, P. T. P. 1979, A&A, 74, L7
Martín, S., Mauersberger, R., Martín-Pintado, J., García-Burillo, S., & Henkel, C. 2003, A&A, 411, L465
Martín, S., Martín-Pintado, J., Mauersberger, R., Henkel, C., & García-Burillo, S. 2005, ApJ, 620, 210
Martín, S., Mauersberger, R., Martín-Pintado, J., Henkel, C., & García-Burillo, S. 2006, ApJS, 164, 450
Martín, S., Requena-Torres, M. A., Martín-Pintado, J., & Mauersberger, R. 2008a, Ap&SS, 313, 303
Martín, S., Requena-Torres, M. A., Martín-Pintado, J., & Mauersberger, R. 2008b, ApJ, 678, 245
Martín, S., Martín-Pintado, J., & Viti, S. 2009a, ApJ, 706, 1323
Martín, S., Martín-Pintado, J., & Mauersberger, R. 2009b, ApJ, 694, 610
Martín, S., Aladro, R., Martín-Pintado, J., & Mauersberger, R. 2010, A&A, 522, A62
Martín, S., Krips, M., Martín-Pintado, J., et al. 2011, A&A, 527, A36
Martín, S., Kohno, K., Izumi, T., et al. 2015, A&A, 573, A116
Martín, S., Aalto, S., Sakamoto, K., et al. 2016, A&A, 590, A25
Martín, S., Martín-Pintado, J., Blanco-Sánchez, C., et al. 2019a, A&A, 631, A159
Martín, S., Muller, S., Henkel, C., et al. 2019b, A&A, 624, A125
Martin-Pintado, J., de Vicente, P., Fuente, A., & Planesas, P. 1997, ApJ, 482, L45
Martín-Pintado, J., Jiménez-Serra, I., Rodríguez-Franco, A., Martín, S., & Thum, C. 2005, ApJ, 628, L61

Mauersberger, R., & Henkel, C. 1989, A&A, 223, 79
Mauersberger, R., & Henkel, C. 1991, A&A, 245, 457
Mauersberger, R., Henkel, C., & Sage, L. J. 1990, A&A, 236, 63
Mauersberger, R., Henkel, C., Walmsley, C. M., Sage, L. J., & Wiklind, T. 1991, A&A, 247, 307
Mauersberger, R., Henkel, C., & Chin, Y. 1995, A&A, 294, 23
Mauersberger, R., Henkel, C., Wielebinski, R., Wiklind, T., & Reuter, H. 1996, A&A, 305, 421
McGuire, B. A. 2018, ApJS, 239, 17
McMullin, J. P., Waters, B., Schiebel, D., Young, W., & Golap, K. 2007, in Astronomical Data Analysis Software and Systems XVI, eds. R. A. Shaw, F. Hill, & D. J. Bell, ASP Conf. Ser., 376, 127
Meier, D. S., & Turner, J. L. 2005, ApJ, 618, 259
Meier, D. S., & Turner, J. L. 2012, ApJ, 755, 104
Meier, D. S., Walter, F., Bolatto, A. D., et al. 2015, ApJ, 801, 63
Milam, S. N., Savage, C., Brewster, M. A., Ziurys, L. M., & Wyckoff, S. 2005, ApJ, 634, 1126
Mouhcine, M., Ferguson, H. C., Rich, R. M., Brown, T. M., & Smith, T. E. 2005, ApJ, 633, 810
Müller, H. S. P., Thorwirth, S., Roth, D. A., & Winnewisser, G. 2001, A&A, 370, L49
Müller, H. S. P., Schlöder, F., Stutzki, J., & Winnewisser, G. 2005, J. Mol. Struct., 742, 215
Muller, S., Guélin, M., Dumke, M., Lucas, R., & Combes, F. 2006, A&A, 458, 417
Muller, S., Beelen, A., Guélin, M., et al. 2011, A&A, 535, A103
Muller, S., Beelen, A., Black, J. H., et al. 2013, A&A, 551, A109
Muller, S., Black, J. H., Guélin, M., et al. 2014a, A&A, 566, L6
Muller, S., Combes, F., Guélin, M., et al. 2014b, A&A, 566, A112
Müller, H. S. P., Muller, S., Schilke, P., et al. 2015, A&A, 582, L4
Muller, S., Kawaguchi, K., Black, J. H., & Amano, T. 2016, A&A, 589, L5
Muller, S., Müller, H. S. P., Black, J. H., et al. 2017, A&A, 606, A109
Muller, S., Roueff, E., Black, J. H., et al. 2020, A&A, 637, A7
Muller, S., Ubachs, W., Menten, K. M., Henkel, C., & Kanekar, N. 2021, A&A, 652, A5
Müller-Sánchez, F., González-Martín, O., Fernández-Ontiveros, J. A., Acosta-Pulido, J. A., & Prieto, M. A. 2010, ApJ, 716, 1166
Nakajima, T., Takano, S., Kohno, K., Harada, N., & Herbst, E. 2018, PASJ, 70, 7
Naylor, B. J., Bradford, C. M., Aguirre, J. E., et al. 2010, ApJ, 722, 668
Nguyen-Q-Rieu, Nakai, N., & Jackson, J. M. 1989, A&A, 220, 57
Nguyen-Q-Rieu, Henkel, C., Jackson, J. M., & Mauersberger, R. 1991, A&A, 241, L33
Nishimura, Y., Shimonishi, T., Watanabe, Y., et al. 2016a, ApJ, 829, 94
Nishimura, Y., Shimonishi, T., Watanabe, Y., et al. 2016b, ApJ, 818, 161
Omont, A. 2007, Rep. Prog. Phys., 70, 1099
Paglione, T. A. D., Yam, O., Tosaki, T., & Jackson, J. M. 2004, ApJ, 611, 835
Pence, W. D. 1981, ApJ, 247, 473
Penzias, A. A. 1981, ApJ, 249, 513
Pérez-Beaupuits, J. P., Güsten, R., Harris, A., et al. 2018, ApJ, 860, 23
Petuchowski, S. J., & Bennett, C. L. 1992, ApJ, 391, 137
Phillips, T. G., van Dishoeck, E. F., & Keene, J. 1992, ApJ, 399, 533
Pickett, H. M., Poynter, I. R. L., Cohen, E. A., et al. 1998, J. Quant. Spectr. Rad. Transfer, 60, 883
Privon, G. C., Herrero-Illana, R., Evans, A. S., et al. 2015, ApJ, 814, 39
Puche, D., Carignan, C., & van Gorkom, J. H. 1991, AJ, 101, 456
Qiu, J., Zhang, J., Zhang, Y., Jia, L., & Tang, X. 2020, A&A, 634, A125
Rekola, R., Richer, M. G., McCall, M. L., et al. 2005, MNRAS, 361, 330
Requena-Torres, M. A., Martín-Pintado, J., Rodríguez-Franco, A., et al. 2006, A&A, 455, 971
Requena-Torres, M. A., Martín-Pintado, J., Martín, S., & Morris, M. R. 2008, ApJ, 672, 352
Rickard, L. J., Palmer, P., Morris, M., Zuckerman, B., & Turner, B. E. 1975, ApJ, 199, L75
Rickard, L. J., Turner, B. E., Palmer, P., Morris, M., & Zuckerman, B. 1977, ApJ, 214, 390
Rico-Villas, F., Martín-Pintado, J., González-Alfonso, E., Martín, S., & Rivilla, V. M. 2020, MNRAS, 491, 4573
Rico-Villas, F., Martín-Pintado, J., González-Alfonso, E., et al. 2021, MNRAS, 502, 3021
Riquelme, D., Amo-Baladrón, M. A., Martín-Pintado, J., et al. 2010, A&A, 523, A51+
Rivilla, V. M., Beltrán, M. T., Vasyunin, A., et al. 2019, MNRAS, 483, 806
Rivilla, V. M., Martín-Pintado, J., Jiménez-Serra, I., et al. 2020, ApJ, 899, L28
Rodríguez-Rico, C. A., Goss, W. M., Zhao, J. H., Gómez, Y., & Anantharamaiah, K. R. 2006, ApJ, 644, 914
Rolffs, R., Schilke, P., Wyrowski, F., et al. 2011, A&A, 527, A68
Romano, D., Matteucci, F., Zhang, Z.-Y., Papadopoulos, P. P., & Ivison, R. J. 2017, MNRAS, 470, 401
Sage, L. J., & Ziurys, L. M. 1995, ApJ, 447, 625
Sage, L. J., Henkel, C., & Mauersberger, R. 1991, A&A, 249, 31
Sakai, N., Saruwatari, O., Sakai, T., Takano, S., & Yamamoto, S. 2010, A&A, 512, A31
Sakamoto, K., Aalto, S., Evans, A. S., Wiedner, M. C., & Wilner, D. J. 2010, ApJ, 725, L228
Sakamoto, K., Mao, R.-Q., Matsushita, S., et al. 2011, ApJ, 735, 19
Sakamoto, K., Gonzalez-Alfonso, E., Martin, S., et al. 2021, ApJ, submitted [arXiv:2109.06695]
Sánchez-Monge, Á., Schilke, P., Ginsburg, A., Cesaroni, R., & Schmiedeke, A. 2018, A&A, 609, A101
Sanders, D. B., Mazzarella, J. M., Kim, D., Surace, J. A., & Soifer, B. T. 2003, AJ, 126, 1607
Scourfield, M., Viti, S., García-Burillo, S., et al. 2020, MNRAS, 496, 5308
Scoville, N. Z., Soifer, B. T., Neugebauer, G., et al. 1985, ApJ, 289, 129
Seaquist, E. R., & Bell, M. B. 1986, ApJ, 303, L67
Sewiło, M., Indebetouw, R., Charnley, S. B., et al. 2018, ApJ, 853, L19
Snell, R. L., Narayanan, G., Yun, M. S., et al. 2011, AJ, 141, 38
Soifer, B. T., Boehmer, L., Neugebauer, G., & Sanders, D. B. 1989, AJ, 98, 766
Solomon, P. M., & de Zafra, R. 1975, ApJ, 199, L79
Solomon, P. M., & Vanden Bout, P. A. 2005, ARA&A, 43, 677
Spilker, J. S., Marrone, D. P., Aguirre, J. E., et al. 2014, ApJ, 785, 149
Stark, A. A., & Wolff, R. S. 1979, ApJ, 229, 118
Strickland, D. K., Heckman, T. M., Weaver, K. A., & Dahlem, M. 2000, AJ, 120, 2965
Strickland, D. K., Heckman, T. M., Colbert, E. J. M., Hoopes, C. G., & Weaver, K. A. 2004, ApJ, 606, 829
Takano, S., Nakajima, T., Kohno, K., et al. 2014, PASJ, 66, 75
Takano, S., Nakajima, T., & Kohno, K. 2019, PASJ, 71, S20
Tang, X. D., Henkel, C., Menten, K. M., et al. 2019, A&A, 629, A6
Tercero, B., Cernicharo, J., Cuadrado, S., de Vicente, P., & Guélin, M. 2020, A&A, 636, L7
Thompson, R. I., Lebofsky, M. J., & Rieke, G. H. 1978, ApJ, 222, L49
Turner, B. E. 1985, ApJ, 299, 312
Turner, J. L., & Ho, P. T. P. 1985, ApJ, 299, L77
Ulvestad, J. S., & Antonucci, R. R. J. 1997, ApJ, 488, 621
Usero, A., García-Burillo, S., Fuente, A., Martín-Pintado, J., & Rodríguez-Fernández, N. J. 2004, A&A, 419, 897
van der Tak, F. F. S., Aalto, S., & Meijerink, R. 2008, A&A, 477, L5
van der Werf, P. P., Isaak, K. G., Meijerink, R., et al. 2010, A&A, 518, L42
van Loon, J. T., Zijlstra, A. A., & Groenewegen, M. A. T. 1999, A&A, 346, 805
Varshalovich, D. A., Ivanchik, A. V., Petitjean, P., Srianand, R., & Ledoux, C. 2001, Astron. Lett., 27, 683
Viti, S., Fontani, F., Jiménez-Serra, I., & Holdship, J. 2019, MNRAS, 486, 4805
Viti, S., Fontani, F., & Jiménez-Serra, I. 2020, MNRAS, 497, 4333
Wallström, S. H. J., Muller, S., & Guélin, M. 2016, A&A, 595, A96
Wallström, S. H. J., Muller, S., Roueff, E., et al. 2019, A&A, 629, A128
Walter, F., Bolatto, A. D., Leroy, A. K., et al. 2017, ApJ, 835, 265
Wang, M., Henkel, C., Chin, Y., et al. 2004, A&A, 422, 883
Wang, M., Chin, Y., Henkel, C., Whiteoak, J. B., & Cunningham, M. 2009, ApJ, 690, 580
Wang, J., Li, D., Goldsmith, P. F., et al. 2020, ApJ, 889, 129
Watanabe, Y., Sakai, N., Sorai, K., & Yamamoto, S. 2014, ApJ, 788, 4
Watanabe, Y., Nishimura, Y., Sorai, K., et al. 2019, ApJS, 242, 26
Watson, A. M., Gallagher, J. S., III, Holtzman, J. A., et al. 1996, AJ, 112, 534
Weiß, A., Requena-Torres, M. A., Güsten, R., et al. 2010, A&A, 521, L1
Weliachew, L. 1971, ApJ, 167, L47
Welty, D. E., Howk, J. C., Lehner, N., & Black, J. H. 2013, MNRAS, 428, 1107
Wernli, M., Wiesenfeld, L., Faure, A., & Valiron, P. 2007, A&A, 464, 1147
Whiteoak, J. B., Gardner, F. F., & Hoglund, B. 1980, MNRAS, 190, 17P
Wilson, T. L. 1999, Rep. Prog. Phys., 62, 143
Wilson, T. L., & Rood, R. 1994, ARA&A, 32, 191
Wilson, R. W., Jefferts, K. B., & Penzias, A. A. 1970, ApJ, 161, L43
Wouterloot, J. G. A., & Brand, J. 1996, A&AS, 119, 439
Yu, H. Z., Zhang, J. S., Henkel, C., et al. 2020, ApJ, 899, 145
Zeng, S., Jiménez-Serra, I., Rivilla, V. M., et al. 2018, MNRAS, 478, 2962

[1] European Southern Observatory, Alonso de Córdova, 3107, Vitacura, Santiago 763-0355, Chile
e-mail: smartin@eso.org

[2] Joint ALMA Observatory, Alonso de Córdova, 3107, Vitacura, Santiago 763-0355, Chile
[3] National Radio Astronomy Observatory, 520 Edgemont Road, Charlottesville, VA 22903-2475, USA
[4] National Astronomical Observatory of Japan, 2-21-1 Osawa, Mitaka, Tokyo 181-8588, Japan
[5] Institute of Astronomy and Astrophysics, Academia Sinica, 11F of AS/NTU Astronomy-Mathematics Building, No.1, Sec. 4, Roosevelt Rd, Taipei 10617, Taiwan
[6] Department of Astronomy, School of Science, The Graduate University for Advanced Studies (SOKENDAI), 2-21-1 Osawa, Mitaka, Tokyo 181-1855, Japan
[7] Department of Space, Earth and Environment, Chalmers University of Technology, Onsala Space Observatory, 43992 Onsala, Sweden
[8] Max-Planck-Institut für Radioastronomie, Auf dem Hügel 69, 53121 Bonn, Germany
[9] Department of Physics, Faculty of Science and Technology, Keio University, 3-14-1 Hiyoshi, Yokohama, Kanagawa 223–8522, Japan
[10] Institute of Astronomy, Graduate School of Science, The University of Tokyo, 2-21-1 Osawa, Mitaka, Tokyo 181-0015, Japan
[11] Institute of Space Sciences (ICE, CSIC), Campus UAB, Carrer de Magrans, 08193 Barcelona, Spain
[12] Argelander-Institut für Astronomie, Universität Bonn, Auf dem Hügel 71, 53121 Bonn, Germany
[13] Astronomy Department, University of Virginia, 530 McCormick Road, Charlottesville, VA 22904–4325, USA
[14] Centro de Astrobiología (CSIC-INTA), Ctra. de Torrejón a Ajalvir km 4, 28850 Torrejón de Ardoz, Madrid, Spain
[15] INAF Osservatorio Astrofisico di Arcetri, Largo Enrico Fermi 5, 50125 Firenze, Italy
[16] Jodrell Bank Centre for Astrophysics, Department of Physics & Astronomy, School of Natural Sciences, The University of Manchester, Manchester M13 9PL, UK
[17] Intituto de Astrofísica de Andalucia (CSIC), Glorieta de al Astronomia s/n, 18008 Granada, Spain
[18] Observatorio Astronómico Nacional (OAN-IGN), Observatorio de Madrid, Alfonso XII, 3, 28014 Madrid, Spain
[19] Cosmic Dawn Center, DTU Space, Technical University of Denmark, Elektrovej 327, Kgs. Lyngby 2800, Denmark
[20] Department of Physics and Astronomy, University College London, Gower Street, London WC1E6BT, UK
[21] Astron. Dept., Faculty of Science, King Abdulaziz University, PO Box 80203, Jeddah 21589, Saudi Arabia
[22] Xinjiang Astronomical Observatory, Chinese Academy of Sciences, Urumqi 830011, PR China
[23] Leiden Observatory, Leiden University, PO Box 9513, 2300 RA Leiden, The Netherlands
[24] Research Center for the Early Universe, Graduate School of Science, The University of Tokyo, 7-3-1 Hongo, Bunkyo-ku, Tokyo 113-0033, Japan
[25] New Mexico Institute of Mining and Technology, 801 Leroy Place, Socorro, NM 87801, USA
[26] National Radio Astronomy Observatory, PO Box O, 1003 Lopezville Road, Socorro, NM 87801, USA
[27] Institute for Space-Earth Environmental Research, Nagoya University, Furo-cho, Chikusa-ku, Nagoya, Aichi 464-8601, Japan
[28] Department of Physics, General Studies, College of Engineering, Nihon University, Tamura-machi, Koriyama, Fukushima 963-8642, Japan

Appendix A: Additional tables

Table A.1. Imaged spectral tuning frequency coverage and amplitude scaling.

ID [a]	Rest. Freq. Coverage (GHz) LSB	USB	a_i [b] Com./Ext.
B3a	84.172 – 87.614	96.190 – 99.335	0.976/1.108
B3b	87.423 – 90.980	99.174 – 102.731	1.003/0.789
B3c	90.777 – 94.334	102.531 – 106.088	0.990/1.107
B3d	94.131 – 97.688	105.885 – 109.441	0.997/1.128
B3e	97.488 – 101.045	109.242 – 112.798	1.009/0.948
B3f	100.848 – 103.993	112.617 – 116.005	1.001/0.922
B4a	125.193 – 128.804	137.281 – 140.977	0.996/0.998
B4b	128.771 – 132.457	140.934 – 144.625	1.003/1.026
B4c	132.424 – 136.110	144.587 – 148.273	1.015/1.001
B4d	136.077 – 139.763	148.240 – 151.931	0.980/0.989
B4e	139.731 – 143.421	151.894 – 155.584	0.992/0.968
B4f	143.384 – 147.069	155.547 – 159.237	1.021/1.014
B4g	147.037 – 150.723	159.200 – 162.891	0.992/1.002
B5a	163.215 – 166.761	175.306 – 178.834	1.016/1.147
B5b	166.566 – 170.112	178.657 – 182.203	0.998/1.050
B5c	169.917 – 173.469	183.684 – 185.560[c]	1.013/0.974
B5d	173.274 – 176.820	185.365 – 188.911	0.993/0.928
B5e	185.380 – 188.890	197.441 – 200.988	0.992/0.856
B5f	188.713 – 192.241	200.798 – 204.338	0.955/0.428
B5g	192.058 – 195.598	204.149 – 207.695	1.033/0.927
B5h	195.409 – 198.955	207.506 – 211.046	1.001/0.974
B6a	211.286 – 214.733	226.279 – 229.766	0.948/0.995
B6b	214.545 – 218.096	229.578 – 233.121	1.000/1.005
B6c	217.908 – 221.459	232.941 – 236.492	1.004/1.034
B6d	221.271 – 224.822	236.304 – 239.847	1.001/1.010
B6e	224.634 – 228.185	239.667 – 243.218	0.995/0.990
B6f	243.202 – 246.753	258.235 – 261.786	0.867/0.991
B6g	246.565 – 250.116	261.598 – 265.157	1.015/1.003
B6h	249.936 – 253.479	264.969 – 268.512	0.924/0.992
B6i	253.299 – 256.842	268.332 – 271.875	0.959/1.006
B6j	256.662 – 260.141	271.703 – 275.126	1.027/1.008
B7a	275.348 – 278.726	287.333 – 290.761	1.020/0.975
B7b	278.490 – 281.978	290.536 – 294.014	1.013/1.008
B7c	281.753 – 285.231	293.789 – 297.267	0.988/1.003
B7d	284.996 – 288.484	297.041 – 300.509	1.257/1.040
B7g	295.015 – 298.663	307.050 – 310.528	0.990/0.984
B7h	298.257 – 301.876	310.293 – 313.781	0.833/0.998
B7e	300.519 – 303.997	312.555 – 316.023	0.993/1.014
B7f	303.772 – 307.240	315.808 – 319.266	0.996/0.994
B7i	328.313 – 331.811	340.579 – 344.097	1.023/0.956
B7j	331.636 – 335.184	343.922 – 347.460	0.989/0.984
B7k	334.999 – 338.527	347.275 – 350.803	0.972/1.017
B7l	338.372 – 341.870	350.658 – 354.136	1.028/0.967
B7o	348.851 – 352.469	360.887 – 364.425	0.922/1.007
B7p	352.204 – 355.822	364.239 – 367.767	1.025/1.034
B7m	354.156 – 357.694	366.441 – 368.298[c]	1.034/1.044
B7n	357.509 – 361.047	369.814 – 373.202	1.008/0.991

Notes. Rest frequency coverage of each individual spectral setup in the lower (LSB) and upper (USB) receiver sidebands, in order of increasing frequency. Each sideband is covered by two slightly overlapping 1.875 GHz-wide spectral windows (Sect. 2.1). Observed frequencies were Doppler corrected to rest frequency assuming a receding velocity of 258.80 km s^{-1} (LSR, radio convention) as originally set up in the observations. [(a)]The ID of each setup corresponds to the ALMA band and an identifying letter matching that in the ALMA archive (http://almascience.nrao.edu/aq/) for archival search purposes. [(b)]Amplitude scale factors. See Sect. 3.1 for details. [(c)]This sideband was imaged in only one spectral window since the other suffered from poor atmospheric transmission.

Table A.2. ALCHEMI calibrator summary.

Calibrator	Frequency Setup/Array [a]
Flux and Bandpass Calibration	
J0006−0623	B3a, B3bTM2, B3c, B3dTM1, B3eTM2, B3f, B4a, B4b, B4c, B4d, B4e, B4f, B4g, B5aTM1, B5bTM1, B5d7M, B6aTM1, B6b, B6c, B6d, B6e, B6fTM1, B6gTM1, B6hTM1, B6iTM1, B6j, B7aTM1, B7bTM1, B7cTM1, B7d, B7e, B7f, B7g, B7hTM1, B7i, B7jTM1, B7kTM1, B7l, B7nTM1, B7p
J0237+2848	B5c7M, B3c, B3dTM2
J0334−4008	B4aTM1
J0423−0120	B5b7M, B5f7M, B5g7M, B5h, B7oTM1
J0522−3627	B4b7M, B4e7M, B5b7M, B5e7M, B5h7M, B6a7M, B6g7M, B6i7M, B7a7M, B7b7M, B7c7M, B7d7M, B7e7M, B7f7M, B7g7M, B7h7M, B7i7M, B7j7M, B7l7M, B7m7M, B7n7M, B7o7M, B7p7M
J2253+1608	B5c7M, B5d7M, B5e7M, B6b7M, B6f7M, B6g7M, B7c7M, B7e7M, B7f7M, B7h7M, B7i7M, B7j7M, B7k7M, B7l7M, B7o7M, B7p7M
J2258−2758	B3bTM1, B3eTM1, B3fTM1, B4a7M, B4b7M, B5a7M, B5b7M, B5c, B5d, B5e, B5f, B5g, B5h, B6a7M, B6d7M, B6e7M, B6g7M, B6h7M, B6i7M, B7a7M, B7b7M, B7c7M, B7d7M, B7g7M, B7h7M, B7k7M, B7mTM1, B7n7M, B7p7M
J2357−5311	B3bTM1, B3fTM1, B5cTM1
Phase Calibration	
J0038−2459	all except B7aTM1, B7m7M [b]
J0106−2718	B4a7M, B4c7M, B4f7M, B4g7M, B6a7M, B6c7M, B7aTM1
J0118−2141	B7m7M, B5h7M, B6e7M, B6j7M, B7b7M, B7f7M, B7g7M, B7i7M, B7k7M, B7l7M, B7m7M, B7p7M
J0132−1654	B7b7M, B6i7M, B7a7M, B7n7M, B7p7M
J0143−3200	B4e7M, B6a7M, B6g7M, B7m7M, B7n7M

Notes. Calibrator sources used on any of the executions of a given setup. Information in this table extracted from the ALMA archive using astroquery (Ginsburg et al. 2019). [(a)]Frequency setup ID (Table A.1) and array combined label. TM refer to 12 m Array, with TM1 and TM2 referring to the extended and compact array, respectively (see Sect. 2). Only ID listed when both arrays used calibrator. [(b)]All spectral setups used J0038−2459 as phase calibrator on at least one of their executions but for those indicated.

Table A.3. Derived physical parameters from LTE fit to the observed spectra.

Formula	$log_{10}\,N$ [a] (cm^{-2})	T_{ex} (K)	v_{lsr} ($km\,s^{-1}$)	$\Delta v_{1/2}$ ($km\,s^{-1}$)	S_0 [b] (Jy $beam^{-1}$)	τ_0 [c]
CO	18.4(17.3)	19.6(0.5)	252.7(1.1)	149.1(3.7)	112.203(3.943)	2.608
^{13}CO	18.1(17.0)	14.6(0.5)	237.2(1.4)	150.0(...)	13.3(0.789)	1.347
HCO^+	14.8(13.4)	14.6(0.3)	233.1(1.0)	151.0(2.2)	7.789(0.396)	0.499
HCN	15.1(13.7)	12.7(0.2)	229.2(0.9)	150.8(2.1)	6.497(0.35)	0.547
$C^{18}O$	17.4(16.2)	15.7(0.9)	235.1(1.9)	150.0(...)	4.462(0.393)	0.252
HNC	14.7(13.2)	12.9(0.2)	227.2(1.0)	134.8(2.2)	3.904(0.141)	0.435
CN	15.7(14.4)	10.2(0.2)	232.6(1.1)	148.6(2.0)	2.129(0.117)	0.249
CS	15.1(13.5)	16.0(0.3)	225.3(1.2)	150.0(...)	1.887(0.063)	0.156
N_2H^+	14.0(12.5)	14.7(0.3)	226.3(1.1)	132.3(2.6)	1.34(0.056)	0.099
C_2H	15.8(14.3)	12.4(0.2)	226.9(1.1)	143.0(2.8)	1.153(0.042)	0.124
CH_3OH	15.4(13.8)	24.1(0.6)	235.3(2.9)	150.0(...)	0.728(0.031)	0.018
$C^{17}O$	16.4(15.2)	16.4(1.1)	239.1(2.3)	150.0(...)	0.618(0.059)	0.028
H_2CO	14.6(13.3)	14.4(0.4)	226.5(2.3)	163.5(5.4)	0.567(0.041)	0.038
H_2S	15.1(13.6)	55.6(1.7)	225.5(3.2)	150.0(...)	0.461(0.025)	0.004
NO	16.5(15.2)	54.0(3.1)	225.2(3.1)	150.0(...)	0.374(0.02)	0.003
$H^{13}CO^+$	13.5(12.3)	11.3(0.4)	233.7(2.5)	150.0(...)	0.339(0.024)	0.041
$H^{13}CN$	13.7(12.1)	12.4(...)	224.1(2.2)	150.0(...)	0.299(0.007)	0.021
SO	14.6(13.1)	25.8(0.6)	219.0(1.5)	150.0(...)	0.27(0.01)	0.007
HC_3N	14.6(14.6)	33.1(17.7)	211.3(46.2)	150.0(...)	0.249(0.285)	0.018
HOC^+	13.1(11.8)	15.2(0.5)	222.0(2.1)	150.0(...)	0.248(0.021)	0.012
$C^{34}S$	14.1(12.8)	18.3(0.5)	220.0(2.2)	150.0(...)	0.234(0.012)	0.015
c-C_3H_2	14.4(14.2)	17.8(7.2)	240.4(42.3)	150.0(...)	0.208(0.151)	0.017
SiO	13.7(13.0)	17.2(1.7)	207.9(8.3)	150.0(...)	0.193(0.045)	0.012
CH_2NH	14.6(13.3)	16.8(0.9)	232.9(4.0)	150.0(...)	0.191(0.01)	0.008
H_3O^+	15.5(14.5)	15.0(...)	207.1(5.7)	120.3(13.4)	0.179(0.026)	0.011
$HN^{13}C$	13.4(12.2)	11.5(0.4)	224.0(2.1)	135.0(...)	0.173(0.012)	0.020
$HCN_{v_2=1}$	14.8(14.3)	300.0(...)	230.0(...)	150.0(...)	0.151(0.049)	< 0.001
CH_3C_2H	15.6(13.8)	43.0(0.5)	243.3(1.0)	145.0(2.5)	0.144(0.004)	0.003
HNCO	15.0(14.0)	29.4(1.7)	232.2(5.5)	150.0(...)	0.13(0.012)	0.005
CH_3CN	13.9(13.4)	38.6(8.8)	246.8(21.1)	150.0(...)	0.086(0.026)	0.002
$HC^{18}O^+$	12.8(12.2)	14.5(...)	233.0(...)	150.0(...)	0.07(0.016)	0.004
$HC^{15}N$	12.9(11.9)	12.6(...)	230.0(...)	150.0(...)	0.064(0.006)	0.006
H_2CS	14.1(13.1)	30.3(3.1)	224.8(6.6)	150.0(...)	0.058(0.009)	0.002
CO^+	14.1(13.5)	8.3(0.9)	231.7(9.9)	150.0(...)	0.058(0.016)	0.014
^{13}CN	14.4(13.4)	10.0(...)	223.8(11.1)	150.0(...)	0.057(0.006)	0.006
CH_3NH_2	14.6(14.4)	15.0(...)	230.0(...)	150.0(...)	0.056(0.038)	0.003
^{13}CS	13.7(12.7)	12.2(0.6)	216.1(4.2)	150.0(...)	0.054(0.006)	0.010
$C^{33}S$	13.4(13.1)	18.0(...)	225.0(...)	150.0(...)	0.047(0.024)	0.003
$HC_3N_{v_7=1}$	13.5(12.5)	300.0(...)	212.0(...)	150.0(...)	0.047(0.005)	< 0.001

Table A.3. continued.

Formula	$log_{10}\,N$ [a] (cm^{-2})	T_{ex} (K)	v_{lsr} ($km\,s^{-1}$)	$\Delta v_{1/2}$ ($km\,s^{-1}$)	S_0 [b] (Jy $beam^{-1}$)	τ_0 [c]
$HNC_{v_2=1}$	13.8(...)	300.0(...)	230.0(...)	150.0(...)	0.046(...)	< 0.001
OCS	14.7(13.9)	60.6(8.3)	230.0(...)	130.0(...)	0.039(0.008)	0.001
NS	14.2(13.0)	16.2(0.7)	225.0(...)	143.3(6.9)	0.039(0.003)	0.004
H_2C_2N	14.1(13.6)	15.0(...)	230.0(...)	150.0(...)	0.038(0.012)	0.007
$H_2{}^{13}CO$	13.3(12.7)	16.5(2.0)	230.0(...)	162.0(21.1)	0.035(0.011)	0.002
HCS^+	13.3(12.5)	15.0(...)	230.0(...)	150.0(...)	0.029(0.004)	0.002
$HOCO^+$	14.0(13.1)	15.0(...)	230.0(...)	150.0(...)	0.028(0.004)	0.005
$^{13}C^{18}O$	15.4(14.3)	15.6(...)	230.0(...)	150.0(...)	0.026(0.002)	0.001
C_3H^+	13.5(12.9)	15.0(...)	230.0(...)	150.0(...)	0.025(0.007)	0.004
SO_2	13.9(13.6)	11.1(9.0)	230.0(...)	150.0(...)	0.022(0.019)	0.002
C_2H_5OH	14.4(14.0)	17.6(6.7)	230.0(...)	150.0(...)	0.021(0.012)	0.001
NH_2CN	13.1(12.6)	48.5(14.3)	230.0(...)	150.0(...)	0.021(0.006)	< 0.001
^{29}SiO	12.8(11.9)	17.0(...)	230.0(...)	150.0(...)	0.02(0.003)	0.001
HCO	14.1(13.7)	5.1(1.1)	230.0(...)	150.0(...)	0.02(0.009)	0.020
^{34}SO	13.5(12.9)	26.0(...)	230.0(...)	150.0(...)	0.019(0.005)	0.001
$^{13}CH_3OH$	13.6(13.4)	24.0(...)	235.0(...)	150.0(...)	0.018(0.011)	0.001
CH_3SH	14.6(14.9)	15.0(...)	230.0(...)	150.0(...)	0.017(0.031)	0.001
$H^{15}NC$	12.3(11.7)	13.0(...)	227.0(...)	135.0(...)	0.016(0.004)	0.001
C_2S	13.7(13.5)	35.1(14.9)	230.0(...)	150.0(...)	0.016(0.012)	0.001
HOCN	13.0(12.4)	29.6(...)	230.7(...)	150.0(...)	0.015(0.003)	0.001
H_2C_2O	14.4(14.2)	15.0(...)	230.0(...)	150.0(...)	0.015(0.009)	0.002
^{13}CCH	14.2(13.8)	12.4(...)	226.9(...)	143.0(...)	0.013(0.005)	0.001
NH_2CHO	13.8(13.6)	15.0(...)	230.0(...)	150.0(...)	0.012(0.007)	0.001
HC_5N	14.6(14.0)	32.0(...)	230.0(...)	150.0(...)	0.01(0.002)	0.001
$Si^{17}O$	12.5(11.8)	17.0(...)	230.0(...)	150.0(...)	0.01(0.002)	0.001
SO^+	13.8(13.1)	15.0(...)	230.0(...)	150.0(...)	0.01(0.002)	0.001
l-C_3H_2	13.2(12.8)	15.0(...)	230.0(...)	150.0(...)	0.008(0.003)	0.001
$C^{13}CH$	13.9(13.4)	12.4(...)	226.9(...)	143.0(...)	0.008(0.002)	0.001
$HC^{13}CCN$	13.2(13.4)	33.0(...)	212.2(...)	150.0(...)	0.007(0.011)	< 0.001
CH_3CHO	14.2(13.2)	15.0(...)	230.0(...)	150.0(...)	0.007(0.001)	0.001
$CH_3{}^{13}CCH$	14.3(13.8)	43.0(...)	242.3(...)	143.7(...)	0.007(0.003)	< 0.001
$H^{13}CCCN$	13.2(13.0)	33.0(...)	212.2(...)	150.0(...)	0.007(0.004)	< 0.001
$CH_3C^{13}CH$	14.2(13.4)	43.0(...)	242.3(...)	143.7(...)	0.006(0.001)	< 0.001
C_4H	15.2(14.5)	15.0(...)	230.0(...)	150.0(...)	0.005(0.001)	0.001
$HCC^{13}CN$	13.3(13.4)	33.0(...)	212.2(...)	150.0(...)	0.005(0.006)	< 0.001
^{30}SiO	12.1(11.8)	17.0(...)	230.0(...)	150.0(...)	0.005(0.002)	< 0.001
HCOOH	13.8(13.4)	15.0(...)	230.0(...)	150.0(...)	0.003(0.001)	0.001
$^{13}CH_3C_2H$	13.9(13.7)	43.0(...)	242.3(...)	143.7(...)	0.003(0.002)	< 0.001
HC_3HO	13.9(13.6)	15.0(...)	230.0(...)	150.0(...)	0.002(0.001)	< 0.001

Notes. Reported uncertainties correspond to the statistical uncertainty of the fit. Fixed parameters in the fit are presented as values with no errors. Physical parameters for CO are obtained assuming a source size of 10″, different from the size of 5″ used for all other molecules (see Sect. 4.3.2 for details) This table was machine generated and values were formatted to a fix number of decimal places and not to significant digits. [(a)]The reported column density $log_{10}N = A(B)$ correspond to $N = 10^A \pm 10^B$. [(b)]Molecules are ordered in descending peak flux density of their brightest transition. [(c)]Opacity at the line center.

Appendix B: Unscaled and scaled spectra

Sect. 3.1 and[4] Appendix C provide details on the absolute and relative flux calibration accuracy for the ALCHEMI measurements. As noted, relative flux calibration was improved by utilizing the information provided by overlapped receiver tunings throughout the ALCHEMI survey. In Figure B.1 we present, for completeness, the unscaled and scaled spectra prior to continuum subtraction (Section 3.3) as extracted from the TH2 position within the compact configuration measurements, 12mC (Band 3) and ACA (Band 4, 5, 6, and 7) observations and imaged to 15″ resolution. Additionally, Figs. B.2 through B.7 present zoomed versions for each receiver Band where Band 7 is split into two figures.

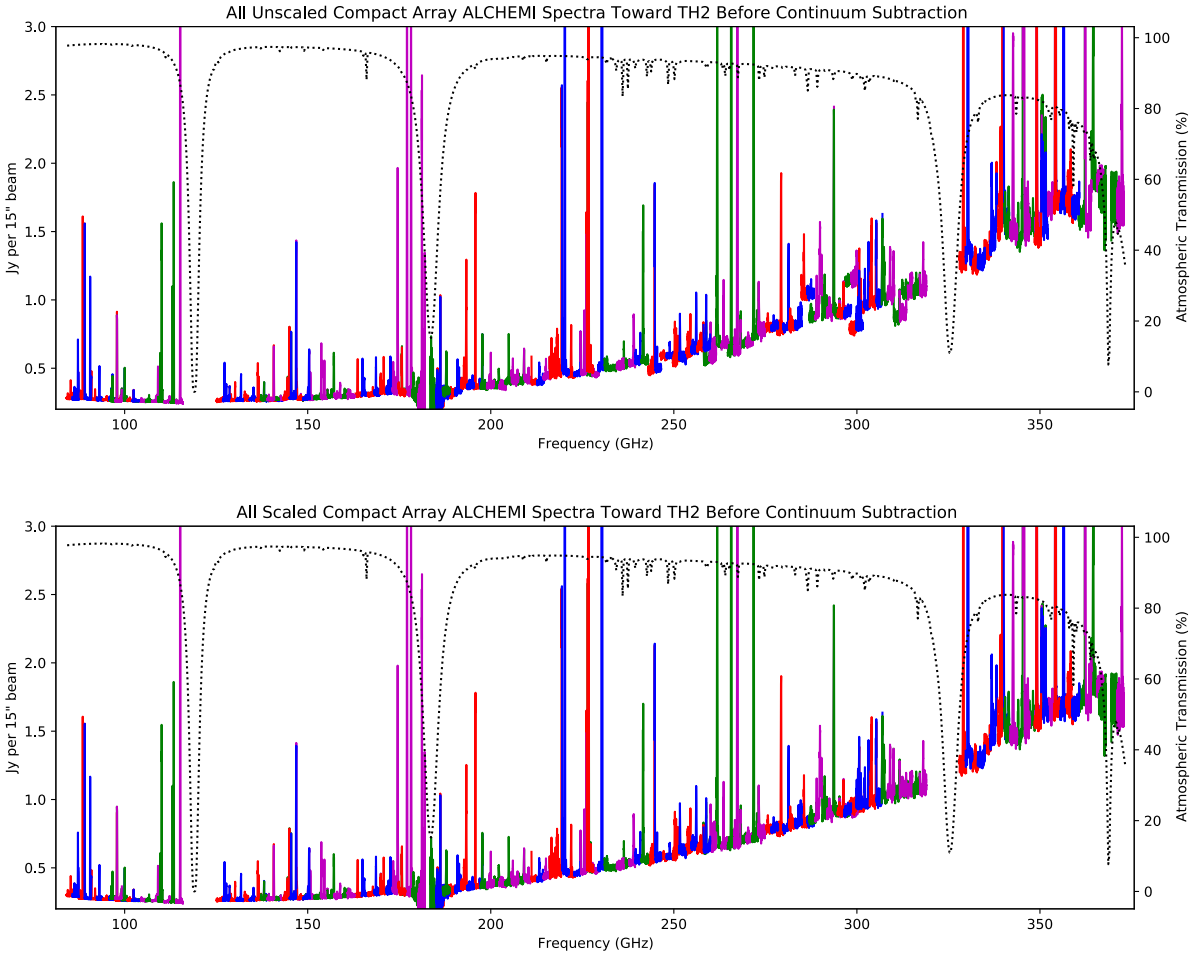

Fig. B.1. Unscaled (top) and scaled (bottom) full spectral scans. The spectra were extracted from the TH2 position in the low resolution data (see Sect. B). The colors in the spectra represent the spectral windows from the lower side band (red and blue) and the upper side band (green and violet). A dotted line indicates the atmospheric transmission for a PWV of 1 mm.

[4] Analysis and diagrams in these appendices make extensive use of astropy (Astropy Collaboration et al. 2013, 2018).

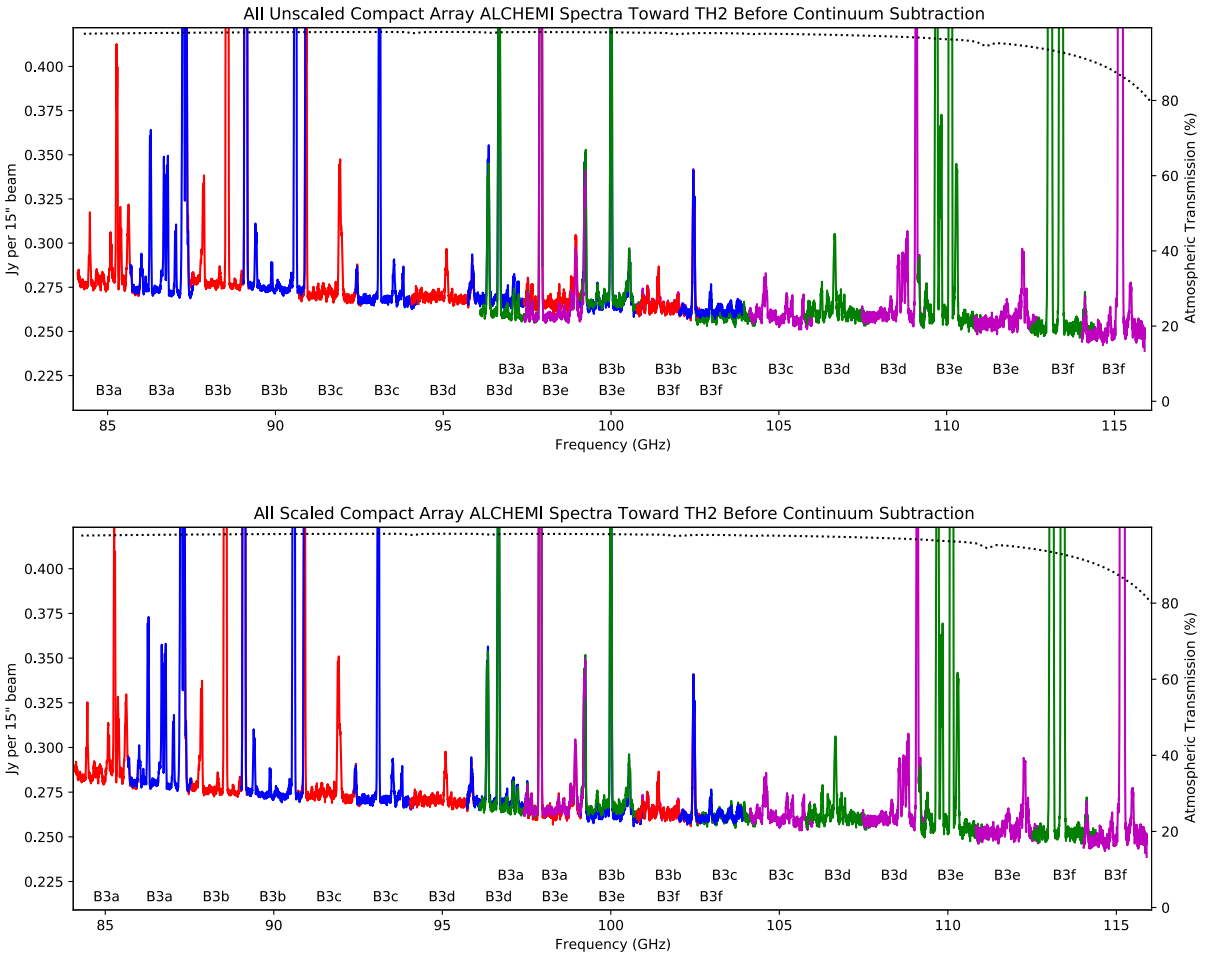

Fig. B.2. Same as Fig. B.1, but for Band 3 unscaled (top) and scaled (bottom). Additionally the label for each of the individual spectral setups (see Sect. 2) are displayed.

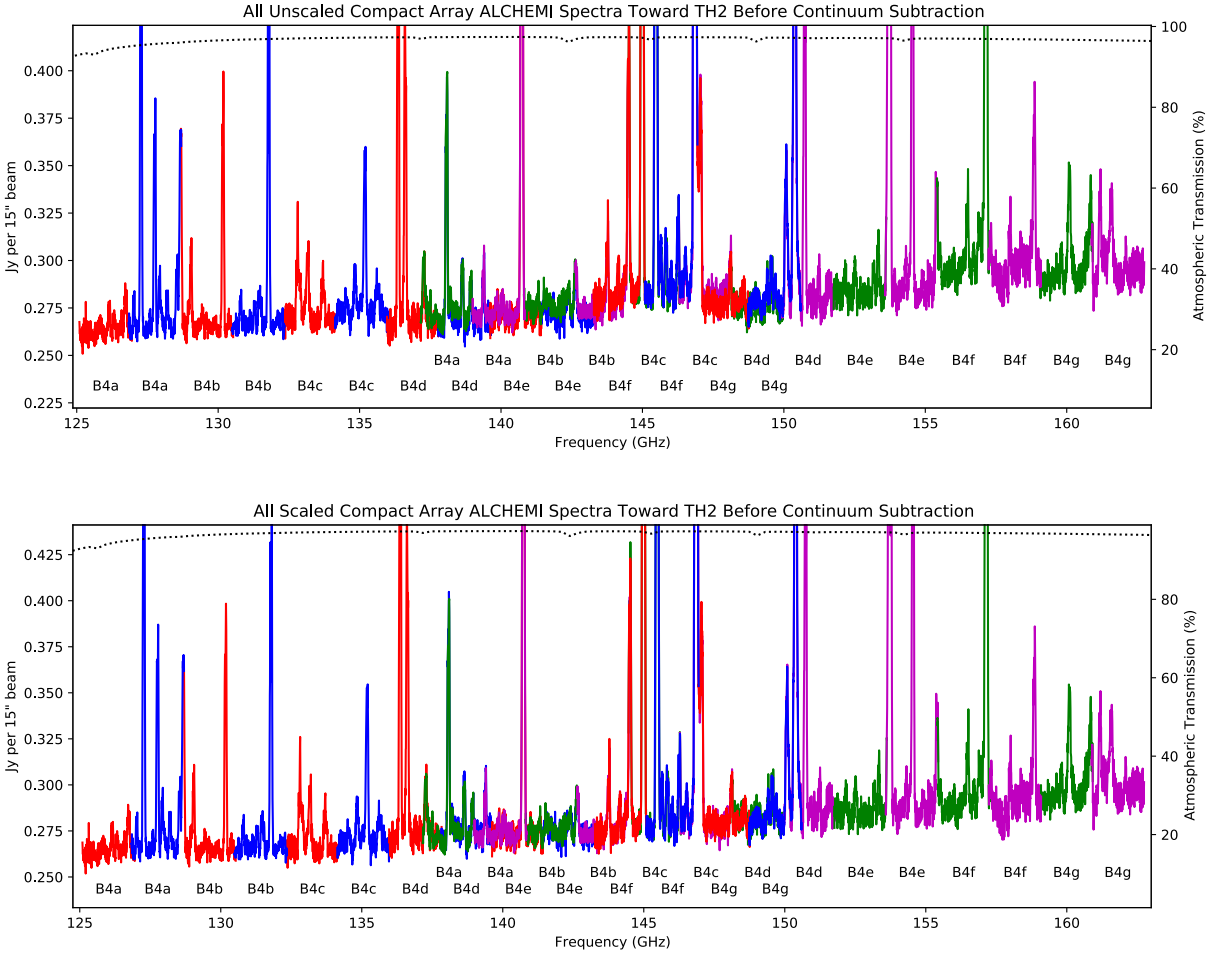

Fig. B.3. Same as Fig. B.2 but for Band 4 unscaled (top) and scaled (bottom).